Advancement of a Quantitative MRI Pipeline to Assess Healing Progression of Soft Tissues in the Knee After ACL Surgery

By:

Dominique Alexis Barnes

B.S., University of Florida, 2020

A dissertation submitted in partial fulfillment of the requirements for the degree of Doctor of Philosophy in the Biomedical Engineering program, a joint program in the Division of Biology and Medicine and the School of Engineering at Brown University

Providence, Rhode Island

May 2026

This dissertation by Dominique Barnes is accepted in its present form by the Biomedical Engineering program, a joint program in the Division of Biology and Medicine and the School of Engineering, as satisfying the dissertation requirement for the degree of Doctor of Philosophy.

Date _____ _____
Braden C. Fleming, Advisor

Recommended to the Graduate Council

Date _____ _____
Jillian E. Beveridge, Reader

Date _____ _____
Joseph J. Crisco, Reader

Date_____ _____
Benjamin Kimia, Reader

Date_____ _____
Ata M. Kiapour, Reader

Approved by the Graduate Council

Date_____ _____
David P. Lindstrom, Dean of the Graduate School

Curriculum Vitae

Dominique Alexis Barnes, Ph.D.('26)

ORCID: 0000-0003-4917-7854

Education

Ph.D. in Biomedical Engineering, Brown University

Scamp. in Data Science, Brown University

B.S. in Mechanical Engineering, University of Florida

Training and Experience

Brown University

PhD, Biomedical Engineering ***May 2026***

Master's, Data Science

Thesis: Advancement of a Quantitative MRI Pipeline to Assess Healing

Progression of Soft Tissues in the Knee After ACL Surgery

- Led quantitative and qualitative biomechanical studies to analyze the ACL to assess return to sport outcomes in collaboration with clinicians from Boston Children's Hospital, resulting in 7 peer-reviewed publications (3 first author; 1 in review)
- Managed and mentored 6 undergraduate students, collaborated with 4 research engineers, surgeons, and 5 PhD researchers
- Oversaw four simultaneous PhD research aims, independently organizing timelines and resources while coordinating inputs from cross-disciplinary teams and actively being involved on Brown's campus as Vice President of the Grad Student Council
- Instructed 90+ undergraduate and graduate students in weekly 2-hour human anatomy cadaveric labs
- Presented original research in oral and poster formats at 11 professional conferences

Exponent, Inc.

Study Facilitator **September 2025 – December 2025**

- Led and coordinated human-subject studies involving wrist wearable technologies, overseeing study documentation, participant interaction, and protocol execution to ensure regulatory compliance, data integrity, and high-quality outcomes
- Instrumented participants with wearables and biometric devices and conducted structured exercise protocols, prioritizing measurement accuracy, participant safety, and comfort while adapting procedures to support reliable data collection
- Integrated exercise data and biometric data with qualitative user feedback to contextualize wearable performance, evaluate functionality, and deliver insights that informed product evaluation and iteration

Exactech, Inc.

Manufacturing Operations Engineer **September 2020 – May 2021**

- Designed a Manufacturing Execution System (MES) to streamline the production of lower limb orthopedic implants
- Managed data migration of over 100 technical drawings and SOPs using Excel-based workflows, enhancing team accessibility

Danaher, Corp.

Manufacturing Intern **May 2018 – August 2018**

- Improved cost and functionality of automated liquid handlers through design updates, resulting in annual savings of $115k
- Developed and installed 20 scalable 3D printed assembly tools using SolidWorks to reduce operational cycle time by 7%

Publications

[+]**Longitudinal Quantitative Mapping Reveals Persistent Meniscal Morphological and Signal Intensity Differences After ACL Surgery** *(AJSM, In Review)* – CSA and SI analysis between ACL surgical patients' limb and non-surgical limb from 6 to 24 months

+***Quantitative Mapping of Meniscus Morphology Using Advanced Imaging Analysis in Young Patients**** *(Sci Rep, In Review)* – CSA and SI analysis between healthy males and females

+**Advancement of an Automatic Segmentation Pipeline** *(MRI, 2025)* - Designed and validated a pipeline to remove metal artifacts from ACL MRIs.

Comprehensive Evaluation of MRI Sequences for Signal Intensity-Based Assessment of ACL following Surgery (*J Orthop Res, 2024)* – Used Signal Intensity to track longitudinal ACL remodeling post-surgery

+**Quantitative MRI Biomarkers to Predict Risk of Reinjury** (*AJSM, 2023)* - Developed predictive MRI metrics to forecast reinjury in surgically treated ACL athletes.

Automated Segmentation of Healed ACL from T2* (*J Orthop Res, 2022)* - Applied novel signal processing to improve clinical assessment of ACL recovery.

+First Author

Conferences & Selected Presentations

- **Early and Persistent Changes in Meniscal Morphology following ACL surgery,** ORS, North Carolina, 2026 *(Meniscus Section Finalist Award)
- **Sex-Based Variations in Meniscal Morphology**, ASB, Pittsburgh, 2025
- **Differences in Meniscal CSA Profiles**, Female Athlete Conference, Boston, 2025
- **Precision Imaging for Metal Artifact Segmentation**, ORS, Phoenix, 2024
- **ACL Signal Intensity Normalization**, ORS, Long Beach, 2023
- **Quantitative MRI Biomarkers for ACL Risk**, ORS, Dallas, 2023

Certifications & Skills

- **Certifications**: Data Science Doctoral Certificate (2024)
- **Software**: Python, MATLAB, R, Visual3D
- **Hardware**: Force plates, motion capture, EMG, MRI instrumentation
- **Methods**: SPM, MRI tissue segmentation, machine learning, signal normalization, artifact correction
- **Soft Skills**: Interdisciplinary collaboration, effective scientific communication, athlete-centered thinking, team player

Teaching & Mentoring

Graduate Teaching Assistant – BIOL 1885: Human Anatomy & Biomechanics, Brown University (Spring 2023, 2025) - Led labs and tutorials focused on musculoskeletal anatomy and joint biomechanics with emphasis on performance and injury.

Mentorship: Empowerment in Movement Mentorship Program (2026), Graduate Mentor for the Department of Biomedical Engineering (2023-2025), Undergraduate and Pre-College Mentor (2022), Leadership Alliance Mentor (2022,2023, and 2024)

Leadership & Service

- **Coach**, South County Volleyball Club, *13s Stingrays* (2025-2026)
- **Vice President**, Brown University Graduate Student Council (2024–2025)
- **Vice President**, Graduate Students of Color in STEM (2024-2025)
- **Financial Secretary**, Theta Psi Omega Chapter of Alpha Kappa Alpha Sorority Inc. (2025)
- **Graduate Council Member**, Nominations Chair, and DEI-focused university committees (2023-present)
- **Treasurer**, Graduate Students of Color in STEM (2022–2024)
- **Engineering Advisory Board Member** (2022–present)
- **Journal of MRI** – Manuscript Reviewer (2021-present)
- **American Journal of Sports Medicine** – Manuscript Reviewer (2025-present)

Awards & Honors

- American Society of Biomechanics **NIH: First Step in Biomechanics Award** (2025)
- American Society of Biomechanics **Student Travel Award** (2025)
- **Graduate Student Leader of the Year** (2025)
- **Innovation Award** – Lifespan Research (2023)
- Brown University **Diversity Fellow** (2021–2022)

Professional Organization Memberships

- American Society of Biomechanics, 2025
- Biomedical Engineering Society, 2019-2022
- Black Biomechanists Association, 2023-2026
- International Women in Biomechanics, 2025-2026
- National Society of Black Engineers, 2016-2021
- Orthopaedic Research Society, 2021-2026

Links

LinkedIn: https://www.linkedin.com/in/dominique-barnes/

Google Scholar: https://bit.ly/DominiqueABScholar

Acknowledgements

There is no version of this dissertation that exists without the people who supported me along the way. I am incredibly grateful to those who challenged me, guided me, and contributed to this journey in ways both large and small. To my advisor, Dr. Braden Fleming, who took a chance on me 5 years ago. Through the ups and downs of this journey, Braden's support and belief in me have been unwavering. "This is your story, tell it how you want to tell it." Braden let me be the author of my own story here at Brown and supported every decision I made, from joining the Open Graduate Program and earning my Master's in Data Science to deciding how to explore and answer these important research questions in my dissertation. I would like to thank Dr. Jillian Beveridge for helping me make sense of this PhD. From asking challenging questions to the reassurance when things didn't work out exactly how I planned them to. I am forever grateful for your support and guidance throughout the years. Dr. Trey Crisco for always being supportive during my time at Brown. Dr. Benjamin Kimia for providing supportive and critical feedback. Dr. Ata Kiapour for being a source of guidance with the technical portions of this work and helping me become a better researcher. Thank you to Dr. Martha Murray and the entire BEAR Team, without whom this collaboration and guidance would not have been possible. I would like to thank Crystal Murray for being a sounding board for all my ideas and for letting me ask her a million questions a day.

Sean, Josephine, and the PhD students who have come before me. I thank you for setting the standards and inspiring me to get to this step. Landon, Siddharth, Ava, and all of the current and previous lab members, thank you for making coming into work so much fun. Thank you to Amy for sharing your knowledge of the latest machine learning

news and helping me through the technical portions of this dissertation. Thank you, Scott, for always being a bright light in the lab with the unlimited supply of jokes. I would also like to thank Quianna because this journey was not an easy one, but I was lucky enough to be able to go through it with you, and for that, I am forever grateful. I would like to thank my friends in Florida and now all over the world. Thank you to the Biomedical Engineering department, specifically the 2021 cohort of BME PhDs. To the Graduate Student Council, thank you for providing me with the opportunity to be a leader within the Brown community. Thank you to all of the administrators that I have been so lucky to work with during my time at Brown. I am grateful to Dr. Sharon Swartz and Dr. Elizabeth Brainerd for fostering one of the best experiences I was able to have at Brown when leading the anatomy labs for two semesters.

Finally, I would like to thank my family, whose encouragement and belief in me never wavered. Thank you for instilling the faith, grit, and resilience that allowed me to make it this far in this journey of life. Their support throughout my graduate education and constant reminders to keep striving forward have meant more than I can express. I hope to continue making you proud.

Dedication

I dedicate this work to my mom, my dad, Luigi, Marcos, Logan, and Koda, who have been my constant source of strength and encouragement along the way.

Table of Contents

List of Figures

List of Tables

Nomenclature

ACL	Anterior Cruciate Ligament
ACLR	ACL Reconstruction
ANOVA	Analysis of Variance Statistical Test
BCH	Boston Children's Hospital
BEAR	Bridge Enhanced ACL Restoration
BMI	Body Mass Index
BPTB	Bone-patellar tendon-bone autograft
CISS	Constructive Interference in Steady State (MRI Sequence)
CNN	Convolutional Neural Network (deep learning architecture)
CPU	Central Processing Unit
CSA	Cross-sectional Area
CycleGAN	Cycle Generative Adversarial Network
DESS	Double Echo Steady State
DICOM	Digital Imaging and Communications in Medicine file
FA	Flip Angle
FEM	Finite Element Model
FN	False Negative
FOV	Field of View
FP	False Positive
GAN	Generative Adversarial Loss
GPU	Graphics Processing Unit
GUI	Graphical User Interface

IKDC	International Knee Documentation Committee
IRB	Institutional Review Board
KOOS	Knee Injury and Osteoarthritis Outcome Score
MAE	Mean Absolute Error
ML	Machine Learning
MRI	Magnetic Resonance Imaging
OA	Osteoarthritis
PCA	Principal Component Analysis
PTOA	Post-Traumatic Osteoarthritis
PSNR	Peak Signal-to-Noise Ratio
qMRI	Quantitative Magnetic Resonance Imaging
ROI	Region of Interest
SI	Signal Intensity
SPM	Statistical Parametric Mapping
SSIM	Structural Similarity Index Metric
T_1-weighted	Apparent spin-lattice relaxation time
T_2*	Apparent spin-spin relaxation time
TE	Echo Time
TN	True Negative
TP	True Positive
TR	Repetition Time

CHAPTER 1: Introduction

1.1 Background and Motivation

Anterior cruciate ligament (ACL) injuries are common in the young and active population.[98] ACL injury risk is highest in specific athlete populations (e.g., football, soccer, basketball, etc.), females, and young adults.[98] For these patients, the desire to regain function and return to sport is paramount. Therefore, surgical treatments such as ACL reconstruction (ACLR) are commonly performed.[98]

An ideal graft used for ACLR should be one that recreates the anatomical, biological, biomechanical, and neurophysiological properties of a native ACL.[20] The most common graft options provided to a patient include bone-patellar tendon-bone, hamstring tendon, and quadriceps tendon autografts.[85,191] The bone-patellar tendon-bone has the advantage of bone healing within the tibial and femoral bone tunnels, however, due to the site of the graft harvest, this graft has a higher rate of anterior knee and kneeling pain in short and mid-term follow-ups.[100,191] Hamstring tendon grafts account for 33 to 53% of all ACL grafts.[112,173,191] Anatomically, the double-bundle technique of the hamstring tendon harvesting procedure for ACLR replicates the double bundles of the native ACL and better restores normal knee biomechanics.[85] The least popular option of the three is the quadriceps tendon graft.[191] A study reported that this graft type did not replicate the biomechanical strength of the native ACL,[127] though more recent studies have shown its strength to be comparable to the hamstring tendon graft.[85,155] Autograft harvest produces donor site morbidity such as anterior knee pain, sensory deficits, and strength deficits.[191] Studies have also shown that only about half of patients following ACLR can return to their pre-injury activity level, with an estimated 1 in 4 adolescent patients having a second ACL injury within the first-year post-operation.[69,98]

New surgical methods to restore the native ACL have been introduced. The bridge-enhanced ACL restoration (BEAR) is a surgical procedure that stimulates ACL healing by placing an extracellular matrix-based implant within the injury site and using it to hold the patient's blood in the space between the torn ends of the ligament.[117-120] The blood-extracellular matrix-based scaffold composite subsequently creates an environment that is biologically conducive to ligament healing. In the first in-human study of the BEAR procedure, patient-reported outcomes, physical examinations, and functional outcomes were similar to those that had undergone ACLR.[120] In a randomized controlled trial, BEAR patients reported greater hamstring strength than ACLR patients.[118] As strength deficits are expected due to the harvesting of the hamstring tendon for ACLR patients, these deficits were not found in BEAR patients, as harvesting of tendons is not required for the surgical procedure.[118] Numerous factors, such as age, activity level, anatomic features, and graft type, are associated with increased risk of reinjury after ACLR,[23,76,151,186] predictive risk factors of reinjury for patients who undergo the BEAR surgery are not as well-known.

Low postoperative patient-reported outcomes (e.g., International Knee Documentation Committee (IKDC) subjective score),[72,129] clinical outcomes (e.g., arthrometer-based knee laxity testing),[179] and asymmetry in joint function (e.g., single-leg hop test) have been used to track ACLR recovery and approximate reinjury risk.[144] However, studies have shown that patient-reported outcome measurements introduce bias and inconsistency when compared to more objective methods.[24] None of these commonly used outcome measures directly assesses the structural integrity of the healing ACL or ACL graft.[179]

The integrity of the ACL after surgery has also been assessed indirectly by evaluating overall knee function, lower extremity functional performance, and patient-reported outcomes.[3,6] However, these measures can be influenced by varying levels of subjectivity. To supplement the existing patient-reported clinical and functional assessments, non-invasive imaging methods have been developed to evaluate graft maturity and to estimate structural properties of the surgically treated ACL and other tissues in the knee using quantitative magnetic resonance imaging (qMRI).[8,80,81]

Advancements of MR systems have allowed for higher strength magnets such as 3T, which provide twice the signal-to-noise ratio of a 1.5T system.[60] Increasing the signal-to-noise ratio improves the overall quality of the image and increases the spatial resolution.[60] The higher spatial resolution allows for greater distinction of complex structures such as the ACL, allowing for the geometric measurement of the ACL, providing clinicians the ability to obtain the cross-sectional area or volume of the tissue non-invasively. Quantitative MRI is also advantageous because various tissues have different signal intensities, or brightness, on MR images that provide contrast and boundaries between tissues that are dependent on the sequence used.[110] T2-weighted images, for example, are sensitive to water-based tissues such as muscle, cartilage, and ligaments. [110] Many pathologies observed in these tissues result in excess fluid accumulation, allowing for ease in preliminary diagnosis and evaluating the extent of injury on MRI.[110] Semi-quantitative clinician-graded scores based on MR signal intensity have been used to evaluate ACL graft or tissue integrity and maturation following surgery. While useful in a research context, signal intensity grading is limited by the

natural subjectivity of the clinician and signal intensity dependency on MR scan parameters, as well as sequence selection.[13,49]

The double-echo steady state (DESS) sequence has become the standard method to measure structural properties of cartilage,[161] while qMRI sequences, such as T_2*-weighted and T_1-weighted, are commonly used to measure ACL structural properties.[13,15,16] Similar to T2*-weighted, the constructive interference in steady state (CISS) sequence has also been associated with structural properties of the ACL.[15,121] DESS is a gradient echo steady-state sequence that combines two echoes to capture both T1/T2* and T2 information to be used for quantitative cartilage assessment, like T2/T2*, and allows for excellent cartilage imaging.[64,161] CISS is also a steady-state, but unlike DESS, it is derived from balanced gradients driven by the T2/T1 ratio to maximize signal-to-noise ratios and provide high-contrast visualizations.[157] An advantage of the CISS sequence, as compared to other sequences such as DESS, is the contrast for the tissue of interest, the ACL. DESS is advantageous when visualizing changes in cartilage structure, as the cartilage has a stark contrast compared to neighboring tissue and bone. However, it is not ideal for visualizing and quantifying changes in the ACL, as the ACL is dark and hard to differentiate from other tissues. However, CISS is sensitive in capturing differences in the ACL tissue. There is a good contrast between the ACL and surrounding tissue, which makes this sequence ideal for ACL analysis and quantification using qMRI parameters. Studies have determined that changes in qMRI parameters from CISS scans, such as signal intensity (SI) and cross-sectional area (CSA) of the ligament or graft, can be used to determine the integrity of the healing structures shown to reflect the biomechanical and histological properties of the healing tissue.[13,15,16] The early time

point (6-9 months) CISS scan qMRI variables provide for a noninvasive assessment of the healing structures to predict ACL surgery outcomes and reinjury risk within 24 months post-surgery.[8] However, due to the differences in MRI sequences used throughout various hospitals or clinical trials, there is a need for standardization of qMRI variable collection to ensure ease of clinical implementation.

Clinical implementation of qMRI may have the potential to identify patients early-on that have an increased risk of post-traumatic osteoarthritis (PTOA), commonly seen after ACL injury and surgery. PTOA is often associated with pain, functional limitations, and an overall decreased quality of life.[53] Approximately 51.6% of ACL-injured patients show radiographic signs of PTOA within 20 years post-surgery.[28] The average age of patients with ACL tears is within the 15-25 year old range, therefore, a majority of these patients may experience PTOA by the age of 35-45 and, on average, are expected to receive a total knee replacement surgery 7 years earlier than patients without a prior history of knee injury and subsequent surgery.[96,152] This statistic is a stark contrast compared to the average age of general osteoarthritis diagnosis of 55-65 years.[96]

The use of qMRI in the clinic can be used to detect early signs of PTOA in patients by identifying regions of morphological differences in the tissue post-surgery, because the damage is irreversible, to prevent the onset and progression of PTOA. There are several hurdles to overcome to translate qMRI into routine clinical practice, such as standardization of qMRI across MRI sequences.[49] The standardization between MRI sequences will allow for quantitative values to be derived from scans regardless of where the MRI was acquired, qMRI-predicted failure loads could be calculated from MRIs across hospitals and clinical trial sites. qMRI is also highly susceptible to metallic

artifacts. Metallic artifacts can be created due to metal fragments that are often unavoidable from ACL surgery, where drill bits are used to create bone tunnels through the femur and tibia to support a graft.[9] The metallic fragments result in noticeably large dark patches within the MR image, which make it difficult to extract quantitative signal intensity values to assess the healing of the tissue.[9] Methods to avoid these dark patches caused by the metallic debris may advance the use of qMRI in clinical practice.

qMRI has been used to detect changes in articular cartilage throughout the progression of PTOA found in patients.[114,168,169] With the advancements of qMRI to track the healing progression of the ACL,[8,9,49] along with the growing belief that ACL injuries incite a whole knee injury response, it would be desirable to use qMRI for the analysis of additional tissues in the knee, such as the menisci. Concomitant ACL and meniscus injuries are well-documented and occur in up to 65% of patients presenting with an ACL injury.[5,92,102,150,168] The lateral meniscus is at an increased risk of being injured during an ACL injury, however, in the case of an isolated ACL injury, the medial meniscus is at a higher risk of a subsequent injury.[22,114,150,169] The functions of the menisci to reduce contact stresses can be disturbed by injury to the tissue, which may result in early onset PTOA, especially in patients with a concomitant ACL injury.[139,182] The effect of an ACL injury on meniscal morphological changes over time is not well understood. qMRI may provide a better understanding of how the meniscus is affected due to an ACL injury and surgery to further validate the use of qMRI in clinical settings to evaluate overall knee health.

The use of qMRI could provide a noninvasive tool to evaluate overall knee health, including the ACL and meniscal healing progression over time following ACL surgery.

This further validates how the clinical implementation of qMRI has the potential to help guide rehabilitation strategies, inform return to sport decisions, and reduce the risk of reinjury and the progression of PTOA.

1.2 Specific Aims

The objective of this dissertation is to advance a qMRI pipeline to noninvasively quantify the integrity of the healing knee joint tissues, including the ACL and menisci. Patients with ACL tears are at a higher risk of reinjury, subsequent meniscal damage, and PTOA, despite ACL reconstruction surgery. Clinical implementation of qMRI has the potential to inform return to sport decisions and reduce the risk of reinjury and PTOA.

This dissertation addressed four specific aims. The first aim was to establish a baseline of qMRI variables as predictors of ACL reinjury. Specifically using qMRI methods to measure tissue morphometry (i.e., volume and CSA) and signal intensity (SI) as a measure of tissue quality of the healing ACL or ACL graft.[15,16] As there are challenges incorporated with the use of qMRI post-surgery, such as metallic susceptibility, the second aim was to develop a method to minimize the effects of these artifacts on MRIs. The third aim focused on the morphological changes of the menisci post-ACL surgery to extend the pipeline to include a quantitative assessment of the menisci and to better understand tissue adaptations post-surgery that may influence the increased risk of PTOA in knee joints. With the validation of qMRI as a way to measure the healing of ACL, the final aim was to develop strategies to harmonize qMRI parameters across various MRI sequences, as there are many sequences utilized throughout research facilities and clinics.

1.2.1 Specific Aim 1

Identify qMRI variables that predict patients at a higher risk of re-tearing their ACL after ACL Restoration surgery.

It has been estimated that 1 in 4 patients may suffer a second ACL injury following an ACL reconstruction (ACLR) surgery.[98] Given that ACL Restoration is a new procedure, the reinjury rate has not been fully assessed. Nonetheless, it is unknown whether qMRI variables, such as the average ACL cross-sectional area, normalized ACL signal intensity, and/or the predicted failure load calculated from those variables, can predict risk of reinjury. (Hypothesis 1) We hypothesized that qMRI data obtained 6 to 9 months post ACL Restoration surgery, the time at which most patients go back to sport, is associated with the risk of revision surgery within 2 years.

1.2.2 Specific Aim 2

Advance the qMRI pipeline to correct MR images with metallic susceptibility artifacts.

ACL surgery is an invasive procedure that may leave behind metal particles of different sizes in the joint.[9] Metallic debris and fixation hardware can distort and occlude regions within MR images that can impede accurate segmentations of regions of interest, such as the ACL or ACL graft. Manually removing artifacts from ACL MR image segmentations can be time-consuming.[9] A machine learning algorithm was developed to advance a current segmentation pipeline to segment out metallic susceptibility artifacts in MR images.[9] (Hypothesis 2) We hypothesized that the signal intensity obtained from the automatic segmentation pipeline with artifact removed would not be significantly

different from the ground truth (manual segmentation) and statistically equivalent within a 5% margin of error.

1.2.3 Specific Aim 3

Evaluate the influence of ACL surgery on the morphological integrity of the meniscus as measured by qMRI.

Concomitant injuries to other structures in the knee, especially the meniscus, are frequently associated with ACL tears or present themselves post-surgery.[92] Meniscus injuries can hinder knee function and lead to early onset PTOA.[22,114] To evaluate the integrity of the menisci post-surgery, the qMRI variables of the meniscus (i.e., cross-sectional area and signal intensity) were considered, as these proved to be valuable to assess the integrity of healing ligaments and grafts. To identify what would be considered baseline meniscal values of CSA and SI on qMRI and to account for any anatomical differences between the sexes, an initial analysis was completed to compare CSA and SI profiles of the intact limb of males and females. (Hypothesis 3.1) We hypothesized that the CSA of the males would be significantly larger than that of females, even when normalized for knee size, and the SI profiles would be similar between the sexes, as the menisci are intact and should have similar tissue composition. The CSA and SI profiles will also be compared between the patient's surgical and contralateral knee to identify morphological changes of the menisci post ACL surgery over 6-, 12-, and 24-months post-surgery. (Hypothesis 3.2) We hypothesized that the CSA profile of the medial and lateral menisci in surgical knees is larger than in non-surgical knees, and the SI of the menisci in the surgical knees will be higher than in non-surgical knees at all time points.

1.2.4 Specific Aim 4

Optimize a deep learning algorithm to transform MR images across sequences.

qMRI parameters, particularly SI, are dependent on the sequence and scanner used.[49] Normalized SI is used as an independent variable to predict the failure load of the ACL.[15,16] However, the predictive equations were developed using the constructive interference in steady state (CISS) sequence on a Siemens 3T magnet. It is currently unknown how the predicted failure load can be evaluated from SI values from more commonly used MRI sequences, such as the Double Echo Steady State (DESS) sequence, a sequence that is important to evaluate articular cartilage health. Deep learning algorithms may be able to translate MRI data from the source domain of DESS to the target domain of CISS to predict the failure load of the ACL from DESS images. (Hypothesis 4) We hypothesized that a deep learning algorithm, CycleGAN, would be able to successfully translate the source domain to the target domain.

CHAPTER 2: qMRI Biomarkers Predict Odds of Reinjury within 2-Years

Quantitative MRI Biomarkers to Predict Risk of Reinjury Within 2 Years After Bridge-Enhanced ACL Restoration

Dominique A. Barnes, Sean W. Flannery, PhD, Gary J. Badger, MS, Yi-Meng Yen, MD, PhD, Lyle J. Micheli, MD, Dennis E. Kramer, MD, Paul D. Fadale, MD, Michael J. Hulstyn, MD, Brett D. Owens, MD, Martha M. Murray, MD, Braden C. Fleming, PhD, Ata M. Kiapour, PhD

The BEAR Trial Team:
Kirsten Ecklund, MS, Ryan M. Sanborn, Meggin Q. Costa, Cynthia Chrostek, Benedikt L. Proffen, Nicholas Sant

The following chapter was published in the *American Journal of Sports Medicine.*

2023 Feb;51(2):413-421. doi: 10.1177/03635465221142323. Epub 2023 Jan 16.

2.1 Abstract

Quantitative magnetic resonance imaging (qMRI) methods were developed to establish the integrity of healing ACLs and grafts. However, the ability of qMRI variables to predict the increased or decreased odds of reinjury is unknown. The purpose of this study was to determine if qMRI variables measured at 6 to 9 months after an ACL restoration procedure can predict the risk of revision surgery within two years of the initial procedure. 124 patients underwent ACL restoration surgery as part of the BEAR I, BEAR II, and BEAR III prospective clinical trials and consented to undergo an MRI of the surgical knee 6 to 9 months after surgery. One subject was lost to follow-up, and four did not undergo MRI (n=119). qMRI techniques were used to calculate the average cross-sectional area (CSA), normalized signal intensity (SI), and a qMRI-based predicted failure load, which was calculated using a pre-specified equation based on CSA and normalized SI. Patient-reported outcomes (International Knee Documented Committee (IKDC) Subjective Score), clinical measures (hamstring strength, quadricep strength, and side-to-side knee laxity), and functional outcomes (single-leg hop) were also measured at 6 to 9 months after surgery. Univariate and multivariable analyses were performed to determine the odds ratios (OR) for revision surgery based on the qMRI and non-imaging variables. Patient age and posterior tibial slope values were included as covariates. Sixteen of 119 patients (13%) required revision ACL surgery within two years. The univariate analyses showed higher IKDC subjective score at 6 to 9 months postoperatively (OR = 1.66 per 10-point increase, p=.035) and a lower qMRI-based predicted failure load (OR=0.66 per 100N increase, p=.014) were associated with increased risk of revision surgery. In the multivariable model, which adjusted for age and

posterior tibial slope, the qMRI-based predicted failure load was the only significant predictor of revision surgery (OR=0.71 per 100N, p=.044). The current findings highlight the potential utility of early qMRI in postoperative management of patients undergoing ACL restoration.

2.2 Introduction

ACL injuries are common in the young active population where the desire to regain function and return to sport is high, thus, surgical treatments such as ACL reconstruction (ACLR) are commonly performed.[98] However, only about half of the patients following ACLR can return to their pre-injury activity level, with an estimated 1 in 4 having a second ACL injury within the first-year after surgery.[69,98] Numerous factors, such as age, activity level, anatomical features, and graft type, are associated with the increased risk of reinjury following ACLR.[76] Given the shortcomings of ACLR (i.e., comorbidities due to graft harvest, risk of PTOA), new surgical methods to repair or restore the native ACL have been introduced.[54,62,118,173] The bridge-enhanced ACL restoration (BEAR) is a surgical procedure that stimulates ACL healing by placing an extracellular matrix-based implant within the injury site and using it to hold the patient's blood in the space between the torn ends of the ligament.[117-120,180] The blood and collagen scaffold subsequently creates an environment that is biologically conducive to ligament healing.[117] As the ACL restoration technique is new, postoperative outcome measures that can predict risk factors for reinjury and subsequent revision surgery remain unknown in patients who undergo the ACL restoration procedure.

Younger age and steeper posterior tibial slope have been identified as risk factors for an ACL graft retear.[23,76,151,186] Low postoperative patient-reported outcomes (e.g.,

International Knee Documentation Committee (IKDC) subjective score), clinical outcomes (e.g., arthrometer-based knee laxity testing), and asymmetry in joint function (e.g., single-leg hop test) have also been used to track ACLR recovery and to approximate reinjury risk.[72,129,144,179] However, studies have shown that patient-reported outcome measurements (e.g., IKDC) introduce bias and inconsistency when compared to more objective methods.[3,6] These discrepancies become more apparent when comparing various validated knee outcome scores.[3,70]

To supplement the existing patient-reported, clinical, and functional assessments, non-invasive imaging methods have been developed to evaluate the graft maturity and to estimate the structural properties of the surgically treated ACL using quantitative magnetic resonance imaging (qMRI).[16,19,80,81,159,178] Studies have determined that changes in the qMRI parameters, such as signal intensity (SI), volume, and cross-sectional area (CSA) of the ligament or graft, can be used to determine the integrity of the healing structures, as these parameters have been shown to reflect the biomechanical and histological properties of the healing tissue.[13,16,19,187] Despite promising preclinical and clinical evidence on the utility of qMRI for non-invasive assessment of the healing ACL structural properties and postoperative remodeling, these techniques have not yet become mainstream. Possible reasons for this include technical challenges in standardizing image acquisition parameters or post-hoc harmonization for consistent qMRI results, and the lack of high-quality evidence on the relative performance of qMRI metrics in predicting ACL surgery outcomes and reinjury risk.[49,178]

The purpose of this study was to analyze the prospectively collected data from the BEAR clinical trials to determine if early qMRI parameters (e.g., those obtained at 6- or

9- month post-ACL surgery) were associated with the risk of revision surgery during the two years following the procedure. The 6 to 9-month window was selected as it corresponds to the time that patients are typically cleared to go back to sport.[3,6,54] We also assessed the ability of common patient-reported, clinical, and functional outcomes, all collected at 6 to 9 months postoperatively, to predict the revision risk in the same cohort. We hypothesized that 1) qMRI-based measure of the healing ACL structural properties (e.g. average CSA, normalized SI, and predicted failure load) collected at 6 to 9 months would predict the odds of revision surgery within two years following the initial ACL restoration procedure, and 2) qMRI-based measures could improve the ability to predict the odds of ipsilateral revision after considering baseline variables (e.g. age, posterior tibial slope), and patient-reported, clinical, and functional outcomes at 6 to 9 months in a multivariable regression analysis.

2.3 Methods

2.3.1 Subjects

Data were acquired from patients enrolled in the BEAR I (NCT02292004, IRB-P00012984),[120] BEAR II (NCT02664545, IRB-P00021470),[118] and BEAR III (NCT03348995, IRBP00026162) clinical trials between February 2015 and January 2019. The three trials were approved by the Institutional Review Boards, and all subjects granted their informed consent before participating. BEAR I was a non-randomized controlled cohort study with 10 patients, BEAR II was a randomized controlled trial with 65 patients, and BEAR III was a prospective dual-center cohort study with 49 BEAR patients (Figure 1).[118,120] Patients were excluded from these trials if they had a history of prior knee surgery, knee infection, or potentially adverse risk factors, including a history

of nicotine use, corticosteroid use, chemotherapy, diabetes, inflammatory arthritis, sickle cell anemia, or anaphylaxis. Patients with concomitant injury to the posterolateral corner, grade III medial collateral ligament injury, or complete patellar dislocation were also excluded. Of the 124 patients who underwent the ACL restoration procedure, 119 had imaging data to carry out the analysis (97%), and revision surgery data were available for the 119 patients at two years (Figure 1). A complete description of the inclusion/exclusion criteria has been previously published.[118,120]

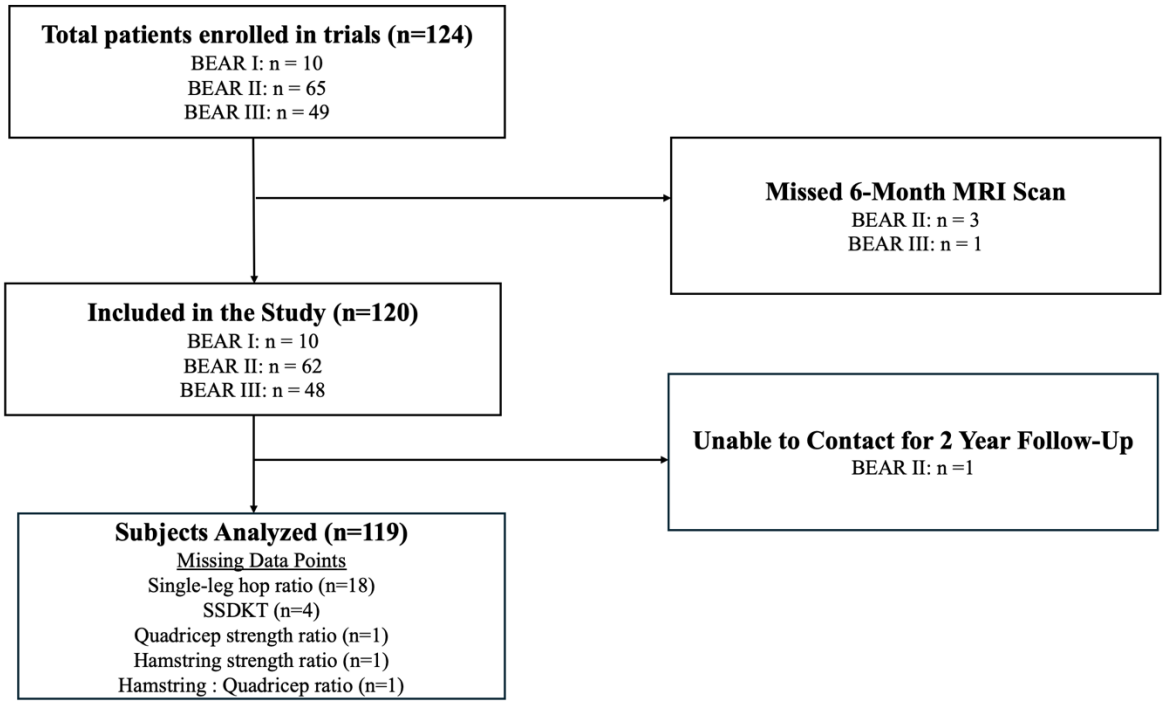

Figure 1. STROBE (Strengthening the Reporting of Observational Studies in Epidemiology) diagram detailing the flow of patients through the analysis. BEAR, bridge-enhanced ACL restoration; SSDKT, side-to-side difference in KT knee laxity.

2.3.2 Surgical Procedure

The ACL restoration procedure utilizes a resorbable implant to provide a platform on which the patient's blood can stimulate the torn ACL to heal.[119-121] The implant is a scaffold composed of bovine extracellular matrix proteins, primarily collagen, which acts

to hold autologous blood between the torn ligament ends. The scaffolds were manufactured at Boston Children's Hospital. Investigational Device Exemptions for the use of the implant in the three trials were granted by the FDA.[117]

Details of the BEAR procedure have been previously described.[118,120] In brief, a whipstitch (Vicryl; Ethicon) was placed in the tibial stump. A cortical button combined with a polyester suture stent (Ethibond; Ethicon) was passed through the femoral tunnel and secured to the proximal femoral cortex. The polyester sutures were threaded through the BEAR scaffold and a tibial tunnel and secured in place with an extracortical button. The scaffold was then saturated with 5 to 10 mL of the patient's blood, and the tibial stump was pulled into the saturated scaffold to repair the ACL.[118,120]

2.3.3 Image Data

MR imaging was performed 6 to 9 months post-surgery on a 3T scanner (Tim Trio or Prisma; Siemens, Erlangen, Germany) using a 15-channel transmit/receive knee coil (Siemens). For the BEAR I and II clinical trials, the Constructive Interference in Steady State (CISS) sequence was acquired for the surgical limb on the Time Trio (Table 1). Harmonization to standardize the images between the two scanners was performed as previously described.[49] The Prisma scans were scaled to the Tim Trio scans due to hardware-necessitated differences in the sequence acquisition parameters (Table 1). The ACL was then segmented from the MR image stack by an observer with more than 8 years of experience in ACL segmentation (A.M.K.) using commercial imaging software (Mimics; Materialise, Leuven, Belgium).

Table 1. MRI Acquisition Parameters for Constructive Interface in Steady State sequence on Tim Trio and Prisma Scanners

	BEAR I, II, and III	**BEAR III**
Scanner	**Tim Trio (n = 109)**	**Prisma (n=10)**
Flip Angle	35	35
Repetition Time (ms)	12.78	12.92
Echo Time (ms)	6.39	6.46
Field of View (mm)	140 x 140	130 x 160
Acquisition matrix (-)	384 x 384	512 x 270
Voxel Size (mm)	0.36 x 0.36 x 1.50	0.31 x 0.31 x 1.00

2.3.4 qMRI Outcome Measures

The normalized SI and average CSA of the ACL were obtained from the MR images at 6 to 9 months after the initial ACL surgery. The normalized SI was calculated from the values of each voxel within the segmented ACL, normalized SI was calculated from the values of each voxel within the segmented ACL, normalized to the SI of the anterior cortex of the femur, and log base-2 transformed as the data were normally distributed (Eq. 1).[16] The anterior cortex of the femur was selected because it is consistently near the noise floor. The difference in background noise texture between scanners was used as a scaling term to harmonize the scanners (ΔNoise).[16]

$$SI_{scaled} = \log_2\left(\frac{SI_{ACL} + \Delta Noise}{SI_{Bone} + \Delta Noise}\right) \quad \text{(Eq. 1)}$$

The mean CSA was calculated by dividing the ACL volume by the ACL length. The qMRI prediction model of ACL failure load was previously determined using a

porcine model of ACL repair, from which qMRI and tensile failure data were avaiable.[16] The models were scaled to humans by exchanging the ligament volume parameter of the previous study with the average CSA to account for ligament size differences between pigs and humans. The updated model used normalized SI and CSA as independent variables to predict the failure load of the ACL (F_{max}) (Eq.2).[16] All measurements were completed within one month of imaging, and values were stored until the two-year outcomes were measured. The imaging examiner was blinded to the postoperative outcomes.

$$Predicted\ F_{max} = \beta_0 + \beta_1 SI + \beta_2 CSA \quad (2)$$

Preoperative MR images were used to measure the posterior slope of the tibial plateau in the medial compartments as previously described.[80,81] The posterior slope of the medial tibial plateau was measured in a sagittal slice at the center of the medial plateau as the angle between a line that joined the peak points on the anterior and posterior rims of the plateau and a line perpendicular to the longitudinal axis of the tibia. Measurements were performed based on established techniques by an experienced member (A.M.K.) using a commercially available image viewer (Osirix Viewer v8.5, Pixmeo SARL).[80,81]

2.3.5 Patient Follow-Up and Non-Imaging Outcome Measures

Six patient-reported, clinical, and functional outcomes were assessed between 6 to 9 months after surgery: 1) the IKDC subjective sore, 2) the side-to-side difference in KT knee laxity (SSDKT), 3) quadriceps strength ratio (%surgical: contralateral), 4) hamstring strength ratio (%surgical : contralateral), 5)quadricep-hamstring strength ratio of the surgical leg, and 6) single-leg hop ratio (%surgical : contralateral). The IKDC subjective score was calculated based on patients' responses to the IKDC questionnaire.[72,129] The

arthrometer measurements (KT-1000; MEDMetric, San Diego, CA) were performed by an experienced independent examiner, who was blinded to surgical laterality and treatment using knee sleeves.[33] Hamstring and quadriceps isometric muscle strength were measured using a handheld dynamometer (Microfet 2; Hoggan Scientific, LLC, Salt Lake City, UT). All measures were performed on each knee in duplicate and duplicates were averaged.[12] During the single-leg hop test, patients wore a brace on the surgically treated knee.

2.3.6 Statistical Analyses

Logistic regression analyses were performed by an experienced statistician (G.J.B.) to identify outcomes obtained at 6 to 9 months postoperatively, including qMRI, patient-reported, clinical, and functional outcomes, and baseline variables that were significant predictors of revision surgery prior to the two year assessment. First, unadjusted odds ratios were estimated for each variable using univariate logistic regression (i.e., one-predictor-at-a-time). Next, a multivariable logistic regression model utilizing a forward stepwise approach was implemented to determine the best set of predictors of subsequent revision and their associated adjusted odds-ratios. To limit the number of potential predictors, only variables with $p<.20$ for their bivariate relationship with two year revision were considered as candidates for the multivariable model. Two baseline variables, age at surgery and posterior slope of the tibial plateau in the medial compartments (MTS), were forced into the multivariable stepwise model (i.e., step 0) as they have been previously shown to be predictive of revision.[154] A multiple imputation procedure was used (n=5 iterations) to allow the use of all cases in the multivariable analyses because listwise deletion of cases due to incomplete data on candidate clinical

variables adversely affects the sample size used for the stepwise multivariable regression model. All analyses were conducted using SAS statistical software (Version 9.4, SAS Institute, Cary, NC, USA) with statical significance based on $p<.05$.

2.4 Results

2.4.1 Baseline Characteristics

The mean ± standard deviation (SD) age of the patients in the three studies was 17.6 ± 7.1 years. Sixty-four (54%) of the patients were female. Ninety-eight (82%) of the patients were Caucasian (non-Hispanic). The mean ± SD of the body-mass index (BMI) was 23.9 ± 3.4 (kg/m^2). The mean SD of the MTS was 5.2 ± 2.4 degrees. Table 2 presents the qMRI, patient-reported, clinical, and functional outcomes recorded at 6 to 9 months postoperatively, considered potential predictors of revision surgery.

Table 2. qMRI and Non-Imaging Outcome Measures at 6 to 9 Months Postoperative (n=119). [a] n=115, [b] n=118, [c] n=101, SSDKT = Side-to-side difference in KT (surgical : contralateral)

Postoperative qMRI Outcomes	
Average Cross-Sectional Area *(mm^2),* mean ± SD	60.2 ± 14.6
Normalized Average Signal Intensity, mean ± SD	1.3 ± 0.2
Predicted Failure Load *(N)*, mean ± SD	705 ± 207
Postoperative Patient-reported, Clinical, and Functional Outcomes	
IKDC subjective score, mean ± SD	78.7 ± 13.4
SSDKT *(mm),* mean ± SD[a]	2.5 ± 2.8
Quadriceps Strength (% contralateral), mean ± SD[b]	94.4 ± 17.1
Hamstrings Strength (% contralateral), mean ± SD[b]	91.6 ± 20.2
Hamstring : Quadriceps Ratio (%), mean ± SD	47.3 ± 15.2
Single-Leg Hop Ratio (% contralateral), mean ± SD[c]	84.9 ± 17.6

2.4.2 Univariate Predictors of Revision

Sixteen (13%) of the 119 analyzed patients required revision surgery prior to the two year follow-up visit. Outcomes significantly associated with increased risk of revision at two years were a higher IKDC subjective score at 6 to 9 months postoperatively (p=.035) and a lower predicted failure load on the 6 to 9 month postoperative qMRI (p=.014; Table 3). Each 10-unit increase in IKDC subjective score (total range 100 points) corresponded to a 65% increase in the odds of revision ACL surgery. Additionally, a 100 Newton (N) increase in qMRI predicted failure load corresponded to a 34% decrease in the odds of revision. The average CSA and normalized SI on the 6 to 9 month qMRI were marginally

associated with increased odds of revision (p<.06), with lower CSA and higher normalized SI associated with increased risk of two year revision (Table 3).

Table 3. Unadjusted odds ratios associated with revision by two year follow-up. P-Values in bold type are significant. SSDKT = side-to-side difference in KT (surgical : contralateral)

Postoperative qMRI Outcomes	**Odds Ratio**	**95% CI**	**P-Value**
Average Cross-Sectional Area *(mm²),* per 10 mm² increase	0.64	0.41, 1.01	.054
Normalized Average Signal Intensity	1.63	0.99, 2.69	.057
Predicted Failure Load *(N)*, per 100N increase	0.66	0.48, 0.92	**.014**
Postoperative Patient-reported, Clinical, and Functional Outcomes			
IKDC subjective score, mean ± SD	1.66	1.04, 2.65	**.035**
SSDKT *(mm),* mean ± SD[a]	1.09	0.91, 1.32	.35
Quadriceps Strength (% contralateral), mean ± SD[b]	1.06	0.77, 1.46	.71
Hamstrings Strength (% contralateral), mean ± SD[b]	1.17	0.92, 1.49	.19
Hamstring : Quadriceps Ratio (%), mean ± SD	1.06	0.77, 1.47	.71
Single-Leg Hop Ratio (% contralateral), mean ± SD[c]	1.27	0.90, 1.80	.18

2.4.3 Multivariable Predictors of Revision

After adjusting for patient age and MTS in the multivariable analysis, the 6 to 9 months postoperative qMRI predicted failure load was the only significant predictor of 2-year revision risk after the initial surgery (Table 4). Each 100N increase in predicted failure load measured at 6 to 9 months corresponded to a 29% decrease in the odds of revision ACL surgery within two years.

Table 4. Adjusted odds ratio associated with revision surgery on multivariable stepwise logistic regression. P-values in bold type are significant.

Predictor	Odds Ratio	95% CI	P-Value
Age *(years)*, 1 year increase	0.65	0.47, 0.90	.009
Medial Tibial Slope *(degrees)*,	1.25	0.97, 1.61	.079
Predicted Failure Load *(N)*, per 100N increase	0.71	0.51, 0.99	**0.044**

2.5 Discussion

This study demonstrated that an increase in predicted failure load of the healing ACL, as measured by qMRI variables at 6 to 9 months after surgery, was associated with decreased odds of revision surgery by two years. Predicted failure load remained a significant predictor after adjusting for baseline variables (i.e., age, posterior tibial slope). Patient-reported, clinical, and functional outcomes at 6 to 9 months did not contribute to the predictive ability of revision in the multivariable model.

Traditionally, return to sport decisions were based on time, with athletes typically being returned to sport at 6 to 9 months after surgery.[193] More recently, some surgeons have also included a battery of patient-reported, clinical, and functional outcomes to

guide the postoperative care plan for safe return to sports.[19] Acceptable scores on assessments such as subjective rating scales, knee laxity tests, and functional hop testing have been used to determine a patient's readiness to return to play.[19] These outcomes remain controversial as studies have shown reinjuries occurring shortly after using these assessments to decide if a patient is ready to return to sport.[30,135,143,189] These assessments lack sufficient resolution to directly assess the healing ligament and are often influenced by factors unrelated to the ACL structure. For example, physical examinations of the knee (e.g., the Lachman and pivot shift test) can be influenced by the injury or hypertrophy of secondary stabilizers of the knee.[57,165] Functional testing (e.g., hop testing and balance testing) can be influenced by the quality of the rehabilitation program, patient compliance, and fear of reinjury.[24,135] Patient-reported outcomes after ACL surgery have been shown to be influenced by self-esteem levels, body mass index, and smoking.[24,61] All of these support the need to improve current clearance protocols, including the addition of non-invasive qMRI approaches to directly assess the healing ligament. These techniques have been shown to identify detailed structural changes in healing ligament and provide an objective evaluation of ligament maturation and remodeling after surgery.[80,81,178] Our current observations are in agreement with a recent study that focused on signal intensity, indicating an increased risk of hamstrings autograft failure in patients with a higher signal intensity ratio at one year.[140] The current study used a combination of CSA and normalized SI to measure predicted failure load to determine the odds of revision surgery, which was evaluated in both univariate and multivariable settings.

Among all the patient-reported, clinical, and functional outcomes, only the IKDC subjective score was associated with subsequent reinjury within two years in the univariate analysis. Interestingly, the results of this study demonstrated that a higher IKDC subjective score was predictive of a higher risk of revision after the ACL restoration surgery, while prior work has demonstrated a higher IKDC score was associated with a lower risk of revision surgery for ACL reconstruction patients.[24,115,190] One possible explanation for this finding is that patients with higher IKDC score felt better at an earlier timepoint and may have returned to activates earlier as a result.[24] Future work should better quantify postoperative activity levels in ACL restoration patients.

A previous porcine study utilized a similar sequence to that used in the current study and demonstrated that volume and normalized SI were independent predictor variables of the maximum failure load.[16] The previous study also showed that an increase in tissue volume and a decrease in normalized SI were related to a higher maximum failure load.[16] A combination of both variables in the maximum failure load prediction model provided a significant improvement in the prediction of the maximum failure load (R^2=.73), compared to either variable by itself ($R^2 \leq .56$).[16] These prior findings align with those of the current study as it would be expected that an increase in the healing ACL failure load would lessen the risk of revision surgery. These findings complement prior reports of temporal changes in ACL or graft normalized SI within two years after surgery, corresponding to tissue healing, and those associated with high graft SI to incomplete healing and integration, as well as graft rupture within one year after ACL reconstruction.[80,81,140]

Postoperative qMRI parameters have not been used to measure the risk of ACL revision surgery in ACL restoration patients, to our knowledge. This study, therefore, provides new insight by suggesting that the predicted failure load, as calculated using qMRI techniques at 6 to 9 months, is associated with the risk of revision within two years post-surgery. This result indicates that for every 100N increase in predicted failure load measured at 6 to 9 months, the odds of revision by two years significantly decreased by 29%. This result provides evidence that a direct assessment of ACL integrity provides valuable data to predict the risk of ACL restoration failure. Future prospective studies are needed to assess whether the use of qMRI assessment can reduce ACL revision surgery when making return to sport decisions. A strength of this study was the low number of patients lost to follow-up, with 120 of the original 124 patients receiving the 6 to 9 month MRI and 119 patients providing information on revision surgery at the two year follow-up. An additional strength of this study was that the qMRI assessor was blinded to postoperative outcomes and did not know which patients had reinjured their ACL at the time of the analysis. The qMRI data were collected at the 6 to 9-month time point and analyzed prior to obtaining the revision data for all patients.

This study also has limitations. The total sample size (n=119) of this cohort and the number of revisions (n=16) were relatively small. Accordingly, derived confidence intervals for the estimated odds-ratio were quite wide. A study with an increased sample size would lead to more precise point estimates and may potentially identify additional factors with smaller effect sizes that may also be associated with failure. Nonetheless, both the univariate and multivariable analyses showed that the qMRI-predicted failure load was associated with subsequent revision surgery. In addition, this study only

evaluated the outcomes of patients undergoing the ACL restoration procedure. However, we believe the qMRI methods could be successfully applied to ACL reconstruction patients as well. Therefore, it would be interesting to determine the relationships between the qMRI parameters and graft failure after ACL reconstruction or primary repair in future studies. While ACL reconstruction patients were included in the BEAR I and BEAR II trials, the sample size (n=10 and n=35) was too small to be considered for this analysis.[118,120] Another limitation was that the MR images were only acquired on scanners by one manufacturer. Future studies should explore if these same equations and qMRI methods would be applicable when different manufacturer magnets are utilized. Lastly, the imaging was performed using a Tim Trio scanner in the single site BEAR I and II trials, while both the Tim Trio and Prisma scanners were used in the BEAR III trial. However, a recently validated harmonization procedure was used to standardize the qMRI images between scanners.[49] Future large-scale prospective studies are needed to confirm the current findings and assess the utility of qMRI in revision prediction after ACL reconstruction.

The current study provides an example of how qMRI parameters can be used to assess the integrity of a healing ACL after the BEAR procedure. Several hurdles, including cost, must be overcome to translate qMRI in routine clinical practice to predict the integrity of the healing ligament or graft. To aid in translation, we have developed harmonization procedures to standardize qMRI results between scanners.[49] We have also engineered automatic ACL segmentation techniques to reduce the segmentation time from hours to seconds to obtain the qMRI parameters required for the prediction.[47,48] An automatic pipeline that included image harmonization, ACL segmentation, and the

predicted equations to determine the failure properties of the healing ligament is under development. We intended to extend the post-processing pipeline to include ACL grafts to increase generalizability and to help facilitate the clinical translation of qMRI. qMRI provides a tool to evaluate rehabilitation progress and assist with return to sport decisions when needed, in light of the additional costs of an MRI.

In conclusion, qMRI obtained at 6 to 9 months after bridge-enhanced ACL restoration surgery determined that the predicted failure load at that time point was a significant predictor of revision ACL surgery within two years of the procedure. Taken together, these data suggest that a direct measure of the structural properties of the healing ligament using qMRI techniques may be beneficial to assess rehabilitation progress and inform return to sport decisions.

CHAPTER 3: Metallic Artifact Removal in Post-Surgical ACL MRI

Advancement of an automatic segmentation pipeline for metallic artifact removal in post-surgical ACL MRI

Dominique A. Barnes, Crystal J Murray, Janine Molino, Jillian E. Beveridge, PhD, Ata M. Kiapour, PhD, Martha M. Murray, MD, Braden C. Fleming, PhD

The following chapter was published in the *Magnetic Resonance Imaging.*

2025 Sep:121:110417. doi: 10.1016/j.mri.2025.110417. Epub 2025 May 14.

3.1 Abstract

MRI has the potential to identify post-operative risk factors for retearing an ACL using a combination of imaging CSA and SI of the healing ACL. During surgery, micro-debris can result from drilling the osseous tunnels for graft and/or suture insertion. The debris presents a limitation when using post-surgical MRI to assess reinjury risk as it causes rapid magnetic field variations during acquisition, leading to signal loss within a voxel. The present study demonstrates how K-means clustering can refine an automatic segmentation algorithm to remove the lost signal intensity values induced by the artifacts in the image. MRI data were obtained from 82 patients enrolled in three prospective clinical trials of ACL surgery. Constructive Interference in Steady State MRIs were collected at 6 months post-operation. Manual segmentation of the ACL with metallic artifacts removed served as the gold standard. The accuracy of the automatic ACL segmentations was compared using the Dice coefficient, sensitivity, and precision. The performance of the automatic segmentation was comparable to manual segmentation (Dice coefficient = .81, precision = .81, sensitivity = .81). The normalized average signal intensity was calculated as 1.06($\pm$ 0.25) for the automatic and 1.04($\pm$ 0.23) for the manual segmentation, yielding a difference of 2%. These metrics emphasize the automatic segmentation model's ability to precisely capture ACL signal intensity while excluding artifact regions. The automatic artifact segmentation model described here could enhance qMRI's clinical utility by allowing for more accurate and time-efficient segmentations of the ACL.

3.2 Introduction

qMRI of the ACL has been used to assess the healing tissue after ACL surgery.[13,15,16,25,81] MRI offers the potential to identify the risk of reinjury of the healing ACL or ACL graft, specifically utilizing a measure of normalized SI.[8,91] However, a significant challenge when using MRI to assess postoperative healing is the presence of susceptibility artifacts caused by metallic micro-debris.[47,48,65,136] Micro-debris is frequently introduced into the joint from the instruments used to drill the osseous tunnels for graft and/or suture insertion during ACL surgery.[47,65,136] The metallic micro-debris causes rapid magnetic field variations when acquiring the images, leading to dephasing and signal loss within a voxel. This signal loss produces dephasing and signal loss within a voxel.[65] This signal loss reproduces black regions in the image where otherwise there would be signal.[65] Accurate automatic segmentation of the ACL tissue that simultaneously avoids artifacts is a significant barrier to implementing qMRI in clinical practice to assess reinjury risk. Thus, post-processing software for automatic image segmentation is needed that will eliminate the impact of metallic artifacts on the overall signal intensity of the ACL or ACL graft, enhancing the predictive utility of qMRI for assessing reinjury risk in the clinic.[35]

Discrete Wavelet Transformation (DWT) is an image processing approach to extract high-frequency components of MR images to highlight fine edges and structures.[32] Rabottino et al employed DWT, in addition to a contouring method for segmentation, and successfully separated various types of tissues in mammographic images.[141] This study demonstrated how DWT can be used as a pre-processing step before applying machine learning models for automatic segmentation. DWT extracts

frequency and spatial information from data, capturing key features such as edges and lines, elements that can contribute to more information than raw voxel data alone.[32,67,147]

Clustering machine learning algorithms, such as K-means clustering, can be used in segmentation tasks to identify a cluster structure in a dataset characterized by high similarity within the same cluster and high dissimilarity between different clusters.[29,36,124,147,156,166] K-means clustering is one of the simplest, computationally efficient, and widely used unsupervised segmentation methods that relies on the image voxels.[29,36,124,131,147,156,166,196] K-means clustering partitions data into a predetermined number of clusters (k).[36,67,153,166] There are two steps in K-means clustering: 1) calculating the k centroids and 2) assigning each voxel to the nearest cluster centroid from the representative imaging data.[36,153] The centroid is determined as the point that minimizes the sum of distances from all other points in the cluster.[36] A commonly used method to define the distance of the nearest centroid is Euclidean distance.[36] Once the distances are calculated, the centroid is established, K-means clustering aims to minimize the sum of distances from each point to its cluster centroid over all centroids.[36,67,153]

Manual segmentation of the ACL without artifacts is time-consuming even when performed by an experienced examiner. [48]The average automatic segmentation time of an intact ACL has been reported to be 0.33 seconds per subject, whereas manual segmentation takes approximately 2 hours even when no artifacts are present.[48] When artifacts are present, the manual segmentation task becomes more complicated and thus would add more time to complete the task.[48]

The study objective was to develop a method to enhance the automatic segmentation of healing ACL tissues by applying DWT and K-means clustering to

effectively remove artifacts that interfere with quantitative image analysis.[47,48] In this study, the performance of this enhanced automatic approach was compared to the most commonly used method, manual segmentation.[47] We hypothesized that the automatic segmentation model with the artifacts removed would attain good performance (scores greater than 0.80) indices (i.e., Dice coefficient, sensitivity, and precision) when compared to the manual segmentation with the artifacts removed by an experienced examiner. Normalized signal intensity was chosen as a quantitative feature for analysis because it has been used as an input for ACL structural property prediction models.[8,15,16,121] We also hypothesized that the average normalized signal intensity of both segmentation methods would yield differences within a 5% margin of equivalence (p-value <.05), indicating that the automatic segmentation method would yield equivalent results to manual segmentation.

3.3 Methods

3.3.1 Image Data

The MR imaging data were obtained from 82 patients enrolled in three Institutional Review Board-approved clinical trials of an ACL restoration procedure (Bridge-enhanced ACL restoration (BEAR); BEAR I Trial (NCT02292004), BEAR II Trial (NCT022664545), and BEAR III Trial (NCT03348995)).[118,121,154] All patients provided their informed consent prior to surgery, and the imaging data were de-identified and shared for the current assessment. Patients who underwent either the BEAR or ACL reconstruction procedures were included. All MR images from the surgical limbs, those that included artifacts of varying amounts and those that did not, were included in this analysis. The MR images were obtained from the surgical limb of the 82 patients six

months after their initial surgery on a 3T scanner (Tim Trio; Siemens) using a 15 channel transmit/receive knee coil (Siemens) and a Constructive Interference in Steady State sequence (Table 5). The ACL and the artifacts were manually segmented from the MRI stack by an examiner with more than 9 years of experience in ACL and ACL graft segmentations (A.M.K.) using commercial imaging software (Mimics; Materialise). Previous reliability assessment of repeated manual segmentations by this examiner using this software was shown to be high (ICC>0.97), justifying it's use as the ground truth.[48,49]

Table 5. MRI Acquisition Parameters for Constructive Interface in Steady State sequence on Tim Trio

	BEAR I, II, and III
Scanner	**Tim Trio (n = 82)**
Flip Angle	35
Repetition Time (ms)	12.78
Echo Time (ms)	6.39
Field of View (mm)	140 x 140
Acquisition matrix (-)	384 x 384
Voxel Size (mm)	0.36 x 0.36 x 1.50

3.3.2 Image Processing

Discrete wavelet transformation (DWT) was applied to each image slice from the image stack to extract frequency and spatial information to sharpen key geometric features such as edges and lines within the image (PyWavelets, 2025).[32,67,147] The image slice was extracted from the MR image stack, and DWT was performed using the biorthogonal

wavelet, which decomposes the image into four sub-bands: approximate (LL), horizontal detail (LH), vertical detail (HL), and diagonal detail (HH) (Figure 2).[32,141,147] To enhance high-frequency components, the LL sub-band, which contains low-frequency information, was set to zero. An inverse wavelet transform was then applied to reconstruct the image with only high-frequency details, resulting in a high-pass filtered image that highlights edges and fine structures (Figure 3).

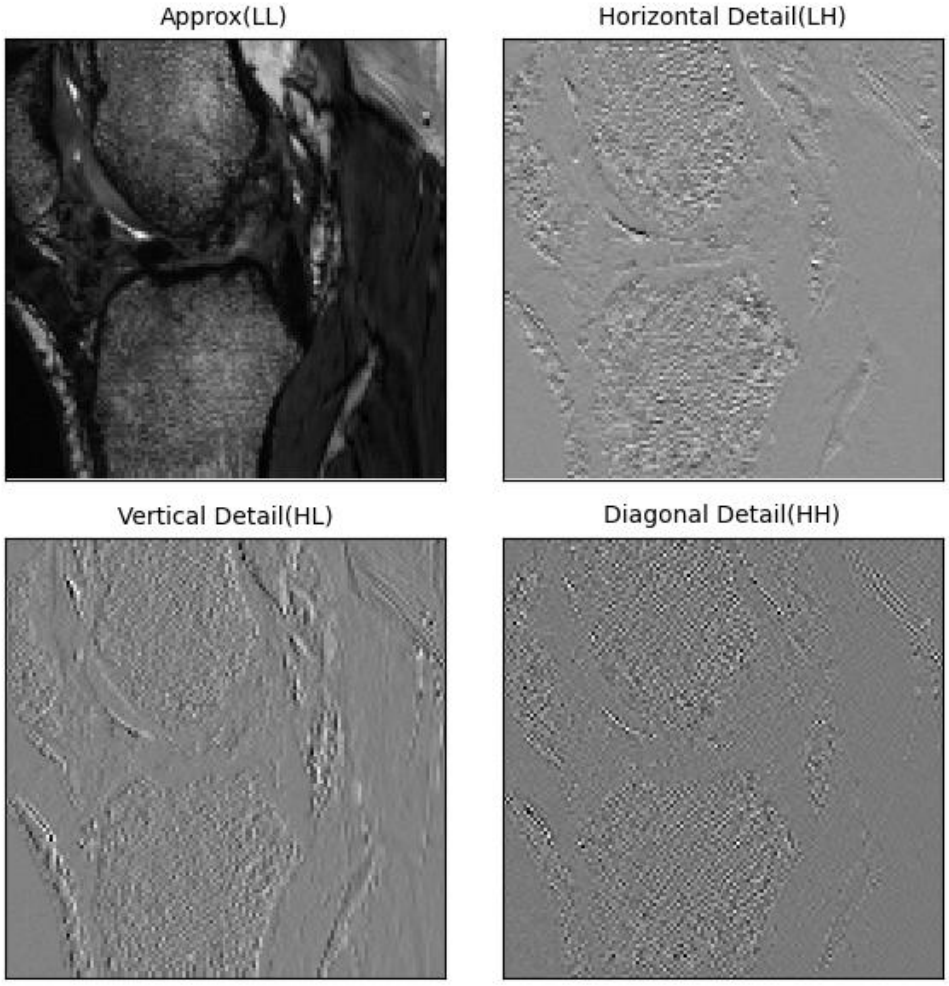

Figure 2. Discrete Wavelet Transformation four sub-bands; approximate (LL), horizontal detail (LH), vertical detail (HL) and diagonal detail (HH).

The DWT step highlights significant features by suppressing low-frequency information, allowing high-frequency content like edges and small structures to be

emphasized in every image slice in the MR image stack (Figure 2). In this way, DWT effectively isolates essential structural features by emphasizing high-frequency details while minimizing low-frequency content, which can aid in the artifact detection and segmentation tasks by creating distinct boundaries of the artifacts in MR images. The high-pass filtered image was then combined with the original MR image, which produced the sharpened image to be used as the input for the K-means model segmentation algorithm (Figure 3).

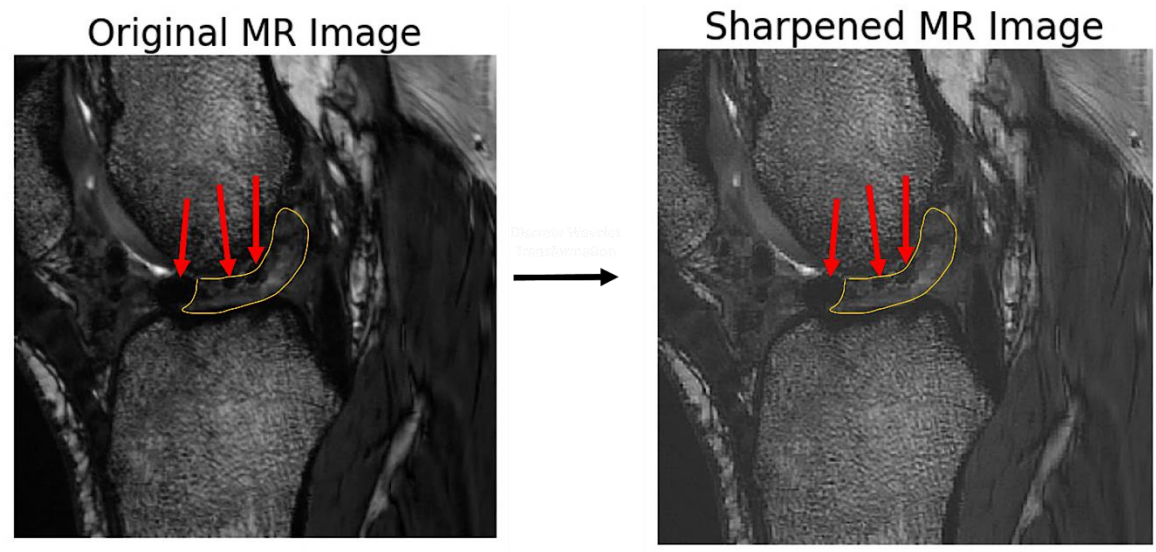

Figure 3. Original MR image before DWT and the sharpened MR image after DWT with red arrows pointing to metallic artifacts along the ACL (outlined in yellow).

3.3.3 K-means Algorithm

After processing the MR images with DWT, the resulting sharpened image stack served as the input for the K-means clustering algorithm (Figure 3). The use of K-means requires an ideal number of clusters, known as *k*, to be selected through prior knowledge of the data or extensive trial and error, as the suggested range of clusters varies between 3 and 10 (Figure 4).[141,142,153] The optimal number of clusters (*k*) selected for this study was determined by a method that measured the data through the intra-cluster distances and

inter-cluster distances of each voxel value in the image.[142,153] To identify the ideal number of clusters, the ratio between the intra-cluster and inter-cluster distances was minimized to determine the value of *k* that indicated more compact clusters.[142,147,153] The ideal number of clusters was determined to be 10 for this application. The K-means clustering algorithm was then applied to the image, grouping the voxels into 10 clusters. The algorithm groups the voxels into clusters based on their similarity, cluster centers are determined, and used to reconstruct the image according to their assigned labeled cluster center. Due to the dark voxel signal intensity of the metallic artifacts, the artifacts are clustered into the minimum voxel cluster center.

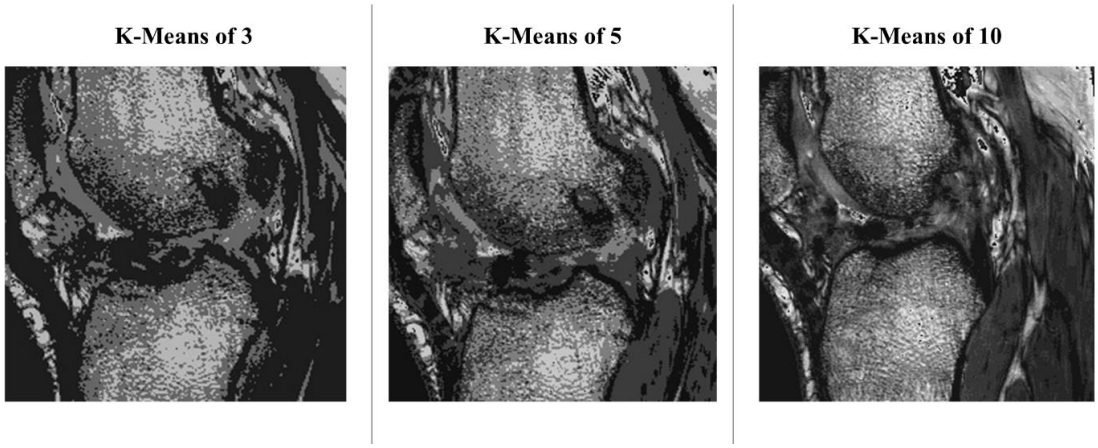

Figure 4. K-means relabeling of an MR image using k of 3, 5, and 10.

A binary mask from the automatic segmentation algorithm was used to isolate the region of interest, the ACL.[47,48] Contours were identified within the segmented image based on a predefined voxel area, creating a boundary around the minimum cluster center encapsulating the artifact regions on the MR image (Figure 5). The contours that represented artifact regions were subtracted from the original binary ACL mask, producing the final segmentation mask with the artifact regions removed (Figure 5). Once all slices in the MRI stack were processed, the stack was combined to create a 3D model

representation of the ACL with the artifacts removed crating a precise model with only ACL tissues for further ACL signal intensity analysis (Figure 5).

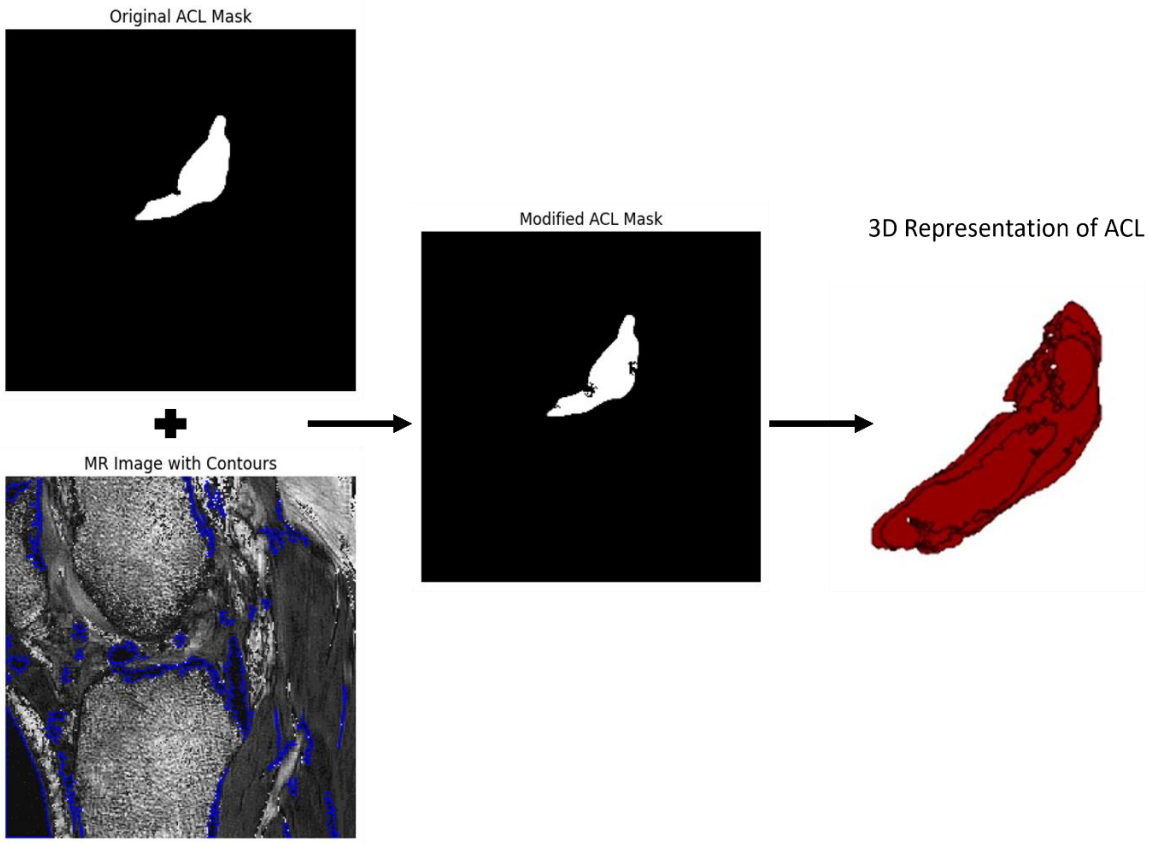

Figure 5. MR image with contours superimposed to original binary mask produced a modified ACL mask with artifacts removed. The mask was used to create a 3D representation of the ACL with artifacts removed.

3.3.4 Performance

Anatomical similarity between the manual and automatic methods was evaluated using three metrics: 1) Dice coefficient, 2) precision, and 3) sensitivity. The Dice coefficient quantifies the overlap between the automatic and manual segmentations, with values closer to 1 indicating a higher degree of similarity between the two segmentations.[47] Precision evaluates the proportion of correctly identified segments among those predicted as positive, reflecting the model's ability to avoid false positives.[47] Precision values

above 0.8 are considered good, representing at least 80% of the regions identified as ACL, minimizing the inclusion of artifacts in the segmentations.[47] A high precision ensures that the automatic segmentation accurately identifies the ACL without mistakenly labeling irrelevant regions or labeling artifacts as relevant regions. Sensitivity measures the ability of the automatic segmentation to correctly identify true positive (i.e., accurately segmented regions), indicating how well the model detects only the ACL.[47] A value above 0.8 is considered good, as it indicates that at least 80% of the true positives (i.e., actual ACL regions) are correctly identified by the automatic segmentation.[47] Collectively, these metrics provided a comprehensive evaluation of the segmentation performance, ensuring that the automatic method was both accurate in identifying ACL structures and precise in minimizing misclassifications and inclusion of artifacts.

3.3.5 Statistical Analysis

Generalized estimating equations (GEE) were used to assess the difference between segmentation types (i.e. manual vs automatic) (*proc glimmix,* SAS Version 9.4, SAS Institute Inc. Cary, NC) with interaction terms evaluated to test whether the differences of ACL signal intensities varied by treatment type (i.e. ACL reconstruction, ACL restoration) or the study trial from which the data were obtained (i.e. BEAR I, BEAR II, BEAR III). MR images were collected across the three clinical trials, and to ensure consistency among images, the signal intensity of the segmented ACLs for both the automatic and manual methods was normalized to cortical bone, scaled by the background noise ratio, and log-transformed.[49,118,120,154] A two-one-sided t-test (TOST) was conducted within the model to test whether the segmentation methods were accurate compared to each other within a 5% margin of error. The null hypothesis was that the

segmentation methods would yield differences outside the 5% margin of equivalence, while the alternative hypothesis was that the segmentation methods would be within the 5% margin of equivalence.

3.4 Results

The automatic segmentation model with the artifacts removed achieved good anatomic performance scores (Figure 6; Dice coefficient = 0.81±0.09, precision = 0.81±0.09, sensitivity = 0.82±0.12). Example segmentations are shown in Figure 7.

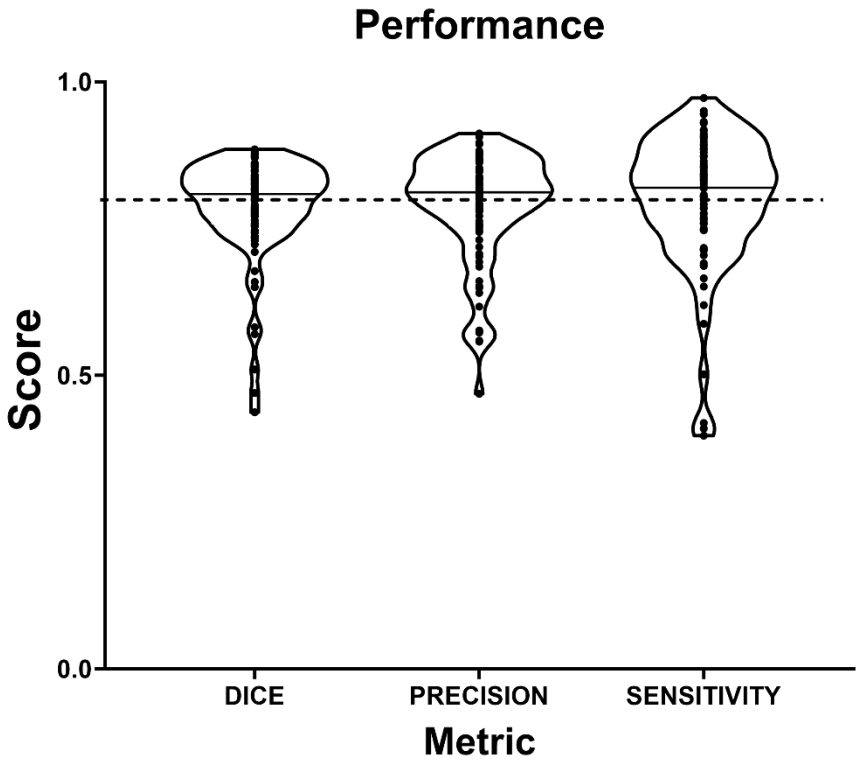

Figure 6. Violin plots that show the anatomic performance metrics for automatic segmentation. The dashed black line signifies a score of 0.8. The median score is represented as a solid black line and each patient's score as a black dot on the graph (n=82; median Dice coefficient=.81±0.09, precision=.81±0.09, sensitivity=.82±0.12).

The effect of segmentation type (i.e., manual vs automatic) on ACL signal intensities did not differ across treatment type (i.e., ACL reconstruction or ACL

restoration) (p = .10) or study trial (i.e., BEAR I, BEAR II, BEAR III) (p = .10). Therefore, the data were pooled across treatment type and study trial. Normalized average ACL signal intensity with the artifacts removed from the patients was 1.04(±0.23) for the manual segmentation (95% Confidence Interval= 1.00 to 1.09) and 106(±0.25) for automatic segmentation (95% Confidence Interval= 1.02 to 1.11), yielding a difference of 2% (95% Confidence Interval= 0.031 to 0.03, P<0.0001).

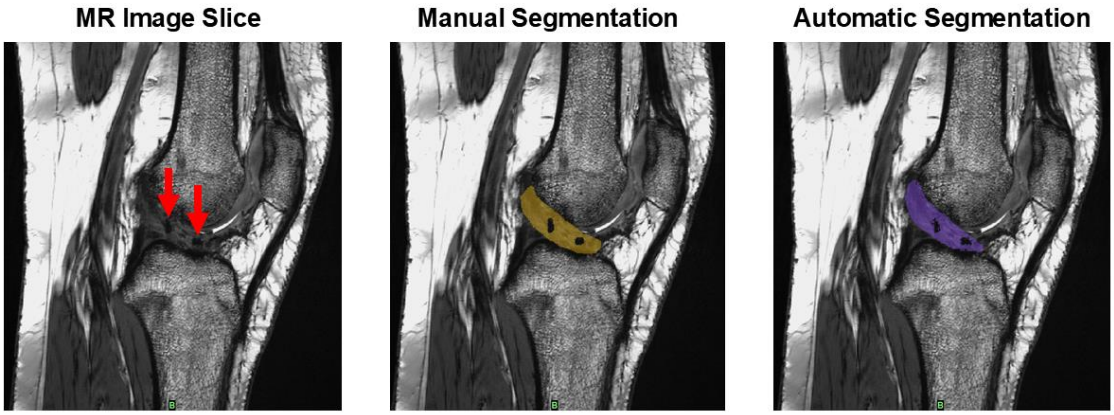

Figure 7. Example segmentation of ACL (left with red arrows pointing to artifacts), manually segmented (middle), and automatically segmented (right).

3.5 Discussion

This study presents the advancements to an automatic segmentation algorithm that was developed to address the challenges in segmenting ACL tissue affected by metallic susceptibility artifacts in MR images. By evaluating anatomical performance measures, we demonstrated the effectiveness of the method using MR images obtained at the 6-month post-operative time point, the time at which clinicians initially consider return to sport decisions.[66] The results demonstrated the good anatomical accuracy of the automatic segmentation process to remove artifacts.

Metallic artifacts pose significant challenges when using MRI post-surgery. Metal artifact reduction sequences such as Slice Encoding for Metal Artifact Correction (SEMAC) or Multi-Acquisition with Variable Resonance Image Combination Selective (MAVRIC) have been used to optimize imaging around metal, specifically large hardware such as orthopaedic implants.[66,75] However, our artifact correction pipeline focuses on the artifacts caused by micro-debris. Furthermore, our sequence was previously optimized for detecting changes in the ACL signal intensity.[15] It is possible that artifact reduction sequences for micro-debris could be developed to provide correction during ACL imaging in the future.

The previous automatic segmentation model without artifact removal produced a decrease in anatomical similarity performance for post-surgical ACL segmentation, which was largely driven by the presence of susceptibility artifacts.[47,136] These artifacts cause rapid magnetic field variations when acquiring images, leading to signal loss on portions of the ligament.[65] The loss of signal significantly affects segmentation accuracy and lowers the mean signal intensity values of the ligament or graft because of the signal loss due to the artifacts. Flannery et al. demonstrated that MR scans without metal artifacts were able to achieve automatic segmentations with the sensitivity and Dice coefficient increased by 2% while the precision increased by 4% when compared to the automatic segmentations of MR scans with artifacts.[47] Our processing algorithm addressed these limitations by incorporating DWT and K-means clustering for handling metallic artifacts, leading to enhanced precision in ACL segmentation. This advancement is not only critical for achieving accurate anatomical segmentations but also serves as a foundation for enhancing qMRI-based models that can predict structural properties from

ACL MR images containing metallic artifact distortions.[8] Ensuring reliable segmentation in the presence of artifacts is a necessary step toward the effective clinical application of these predictive models.[8]

The anatomical performance of the automatic segmentation pipeline was evaluated using key metrics such as the Dice coefficient, sensitivity, and precision, which collectively provide a robust measure of the segmentation's accuracy and reliability with manual segmentation. The Dice coefficient of 0.81 indicates a strong overlap between the automatic segmentation and the ground truth, suggesting reliable alignment with manual segmentation. While this level of agreement is promising and suggests that the algorithm can effectively replicate expert-defined boundaries, the slight deviation from the perfect alignment highlights the influence of metallic artifacts to cause distortions which can obscure tissue contrast ultimately affecting the precision of the automatic segmentation.

The precision (0.81) and sensitivity (0.82) values demonstrate a balanced ability to include relevant ligament tissue while avoiding false positives. The algorithm effectively identified true ACL tissue while minimizing inclusion of irrelevant surrounding tissue or artifacts (precision) and captures the full extent of the ligament structure (sensitivity). While these values demonstrate effective segmentation, they also highlight areas where performance could be improved, such as better artifact differentiation and enhanced model training with diverse datasets. At the same time, the consistency in values across all metrics highlights the robustness of the segmentation approach despite these challenges, providing a reliable framework for addressing the complexities of segmenting ACL tissues in the presence of metallic susceptibility artifacts.

As for clinical utility, signal intensity is essential for assessing tissue integrity during recovery, as it can provide valuable insight into ligament density and healing progression.[8,14,15,121] The similarity in average normalized signal intensity values between the manual (1.04 ± 0.23) and automatic (1.06 ± 0.25) methods, which fell within the 5% equivalence margin, suggests that the automatic pipeline preserves the relevant qMRI features. These findings demonstrate the effectiveness of the algorithm for anatomical segmentation, while also highlighting the importance of maintaining signal intensity equivalence. Ensuring reliable signal intensity readings, particularly in images affected by metallic artifacts. The consistent performance across metrics validates the advancements made to the automatic segmentation pipeline and provides a foundation for possible clinical translation.

This study leveraged DWT combined with K-means clustering to enhance the segmentation of the ACL in MR images. The advanced automatic segmentation approach successfully distinguished metallic artifacts in both ACL grafts and healing native ACLs, demonstrating its adaptability to different tissue conditions. This adaptability highlights the robustness of the algorithm in handling diverse anatomical and post-surgical scenarios, further advancing its potential for clinical applicability. Additionally, K-means clustering provides a computationally efficient method for classifying voxel intensities, making it easy to identify artifact regions through contouring around the minimum voxel intensity. [137] A current limitation of qMRI is the time it takes to manually segment important anatomical structures such as the ACL. An additional challenge with post-surgical segmentation is identifying and compensating for metal artifacts.[32,36,67,75,141,147] The advancements of more computationally efficient methods of post-processing MRIs,

such as automatic segmentation that can compensate for metallic artifact may increase the feasibility of implementing qMRI into clinical setting.[48]

This study is not without limitations. Due to the limited sample size of patients with metallic artifacts within the ACL boundaries, we were unable to utilize deep learning algorithms to retrain our automatic segmentation pipeline to avoid the artifact regions. Nonetheless, our method was determined to be robust based on the performance metrics. Another limitation was that the reliance on K-means clustering to relabel voxel values of an image can result in suboptimal outcomes if the initial cluster centers are poorly chosen.[141,153] Well-chosen clusters ensure that the relabeled voxel values accurately represent distinct image features, preserving essential details and enhancing the quality of subsequent analysis of artifact regions.[141,147,153] Furthermore, K-means is intensity threshold-based, meaning that its effectiveness can vary significantly across different MRI sequences or scanners, which may limit generalizability. Future work should explore the integration of a more sophisticated clustering algorithm or deep learning technique to further enhance segmentation performance regardless of MRI sequence or machine. Lastly, manual segmentation served as the ground truth metric, which could be observer-dependent.[49] The manual segmentations were performed by an observer with 9 years of experience, which have been previously shown to be reliable.[48]

There has been a longstanding challenge of dealing with artifacts present in MR images of healing ACL and/or graft tissues post-operation.[47,49,136] The presence of metallic micro-debris has made it exceedingly difficult to develop automatic post-image processes to acquire qMRI parameters such as ACL signal intensity.[47,49,136] The present study demonstrated that DWT in combination with K-means clustering can be integrated

into an automatic segmentation pipeline to automatically segment the ACL while removing artifact regions in a precise and efficient manner.

CHAPTER 4: Quantitative Mapping of Meniscal Morphology

Quantitative Mapping of Meniscus Morphology Using Advanced Imaging Analysis in Young Patients

Dominique A. Barnes, Crystal J. Murray, Mohammadreza Movahhedi, PhD, Jillian E. Beveridge, PhD, Ata M. Kiapour, PhD Martha M. Murray, MD Braden C. Fleming, PhD

The following chapter was published in *The Scientific Reports.*

2026 Mar doi: 10.1038/s41598-026-46590-y. Epub 2026 Mar 31

4.1 Abstract

Detailed location-specific meniscal size and MR-derived structural properties across meniscal regions to identify sex-based differences are not well established. The proposed advanced imaging method allows for localized measurements of meniscus CSA and SI along the arc length in females and males. We hypothesized that females would exhibit smaller normalized CSA values than males and that SI profiles would not differ between sexes. MR images of non-injured knees from 105 individuals (60 females; age 13-35) were analyzed to quantify CSA and SI along the medial and lateral meniscal arc lengths. Measurements were normalized to knee size to enable sex-based comparisons. Normalized lateral meniscus CSA did not differ significantly between females and males. In the medial meniscus, normalized anterior CSA was significantly smaller in females than males ($P < .001$; 0.04 mm^2/mm). No significant sex-based differences were observed in SI profiles along the arc length for either meniscus. This study demonstrates regional sex-based differences in normalized medial meniscus CSA but no differences in normalized SI for either meniscus. Given that differences of the normalized CSA were observed only in the anterior region of the medial meniscus, sex-based variations may not be globally distributed across the meniscus, but instead confined to specific anatomical regions. This underscores the importance of subregional analyses, as whole-structure analyses may exclude localized differences.

4.2 Introduction

The menisci are crescent-shaped fibrocartilaginous soft tissues with wedge-like CSA that are essential for load transmission and distribution, shock absorption, and stabilization.[2,46,104,113,163] The wedge-shaped cross-section of the meniscus allows for the transfer of axial forces between the round femoral condyles and flat tibial plateau.[104,108,181] The medial meniscus covers 51-74% of the articular surface of the medial tibial plateau, while the lateral meniscus covers 75-93% of the articular surface of the lateral tibial plateau.[133] Together, the menisci collectively transmit approximately 40-60% of the axial force through the knee, distributed between the medial and lateral compartments.[88] Biomechanically, the size and shape of the meniscus dictate how the contact force between the femoral condyles and tibial plateau can be distributed across the joint, with a greater contact area resulting in decreased tibiofemoral contact stress.[40] Disruption to the meniscal tissue due to injury or impact loading can severely alter joint biomechanics and result in pain.[40,87,174] Abnormalities can be observed on MRI, with increased SI indicating the presence of injury or tissue degradation.[89]

Significant knee size differences between sexes have been reported. Males were found to have, on average, a 9-mm larger mediolateral measurement of the femoral condyle and an average of 8-mm larger mediolateral measurement of the tibial plateau.[101] Sex-based differences were also found in the medial and lateral menisci length, width, horn distance, and normalized CSA, in which females had smaller menisci than age-matched boys (15-18 years).[78] A large-scale analysis revealed that female menisci covered less of the tibiofemoral joint surface.[55] Maximum articular contract stressed magnitude and distribution have been found to be predictors of knee osteoarthritis,

especially after a traumatic event such as an ACL tear, which can lead to post-traumatic osteoarthritis (PTOA).[160] The difference in meniscal features that are correlated with greater loading in females may partially explain why females are more likely to develop PTOA, even in the absence of injury.[55] Zonal MR T2 values have been previously evaluated in a young, healthy population, where medial and lateral menisci were averaged, and differences were reported primarily in the red and red/white zones, with men showing significantly lower T2 values than women.[175] However, these studies assessed broad zonal averages rather than detailed regional variation. Therefore, localized sex-based differences in meniscal size and MR-derived properties across the anterior, middle, and posterior regions are unknown.

The study aimed to systematically characterize the CSA and SI along the arc length of the contralateral, uninjured menisci in a cohort of females and males who had undergone ACL surgery. The contralateral limb was examined to characterize any potential underlying anatomical differences. We hypothesized that in the uninjured meniscus, 1) the regional CSA in females will be significantly smaller than in males, even when normalized by knee size, and 2) no significant difference would be found in the normalized meniscal SI profiles between females and males.

4.3 Methods

4.3.1 Data Source

The study protocol was carried out in accordance with all relevant guidelines and regulations. The de-identified MR images used for this analysis (n = 105, 60 females and 45 males, age: 13-35 years) were obtained from subjects enrolled in the IRB, and FDA-approved BEAR I and BEAR II clinical trials (Clinicaltrials.gov: NCT02292004;

NCT02664545; IRB#: P00012985 and P0002147).[118,119] All subjects provided their informed consent. The current analysis utilized the MRI scans of the uninjured contralateral knees of individuals who had undergone ACL surgery in their other knee. Patients missing contralateral images or with an injured or discoid meniscus in the contralateral knee were excluded (Figure 8).

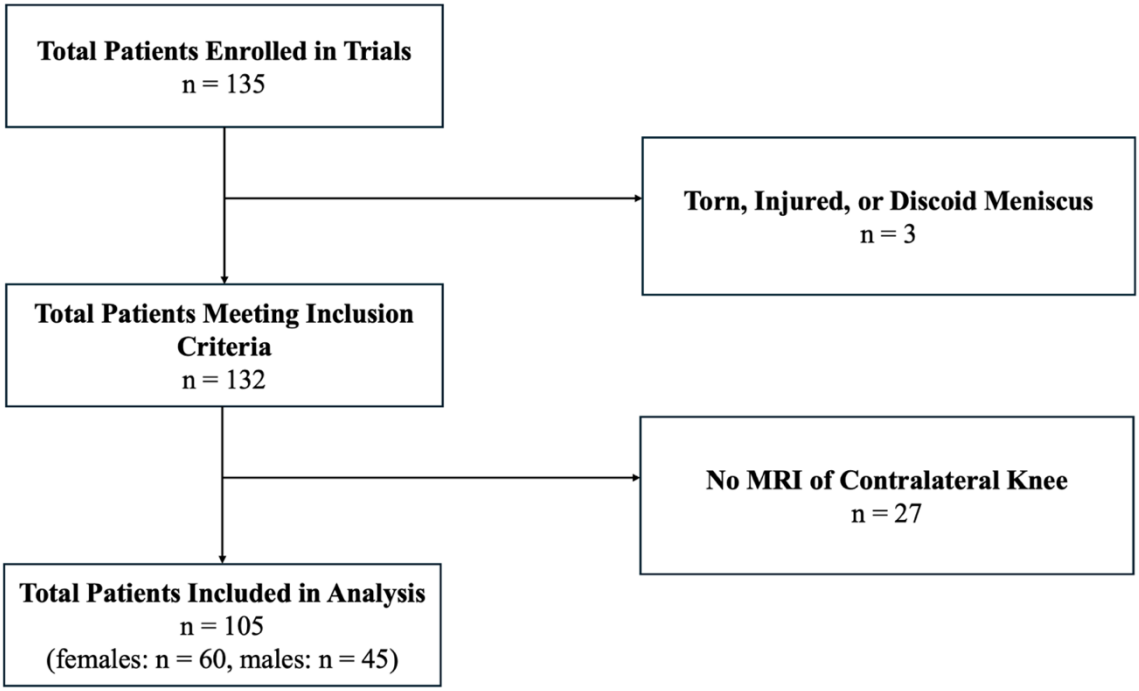

Figure 8. STROBE Diagram of patients included in the analysis

4.3.2 Image Data

Images of the knees were acquired using the three-dimensional Constructive Interference in Steady State (CISS) sequence (TR/TE = 14/7 msec, FA =35, Voxel Size = 0.4mmx0.4mmx1.5mm) using a 3T (Tim Trio, Siemens Healthcare, Erlangen, Germany) and a 15-channel knee coil (Siemens Healthcare, Erlangen, Germany). The menisci were automatically segmented from the 3D MR image stack using a 3D UNet based convolutional neural network (Dice coefficient score 0.98).[103] The automatic

segmentations were manually verified by two experienced examiners using commercial image processing software to visually confirm the proper alignment of the 3D segmented mesh of the menisci to the meniscal regions in the MRI (Mimics v23.0; Materialise) (Figure 9).

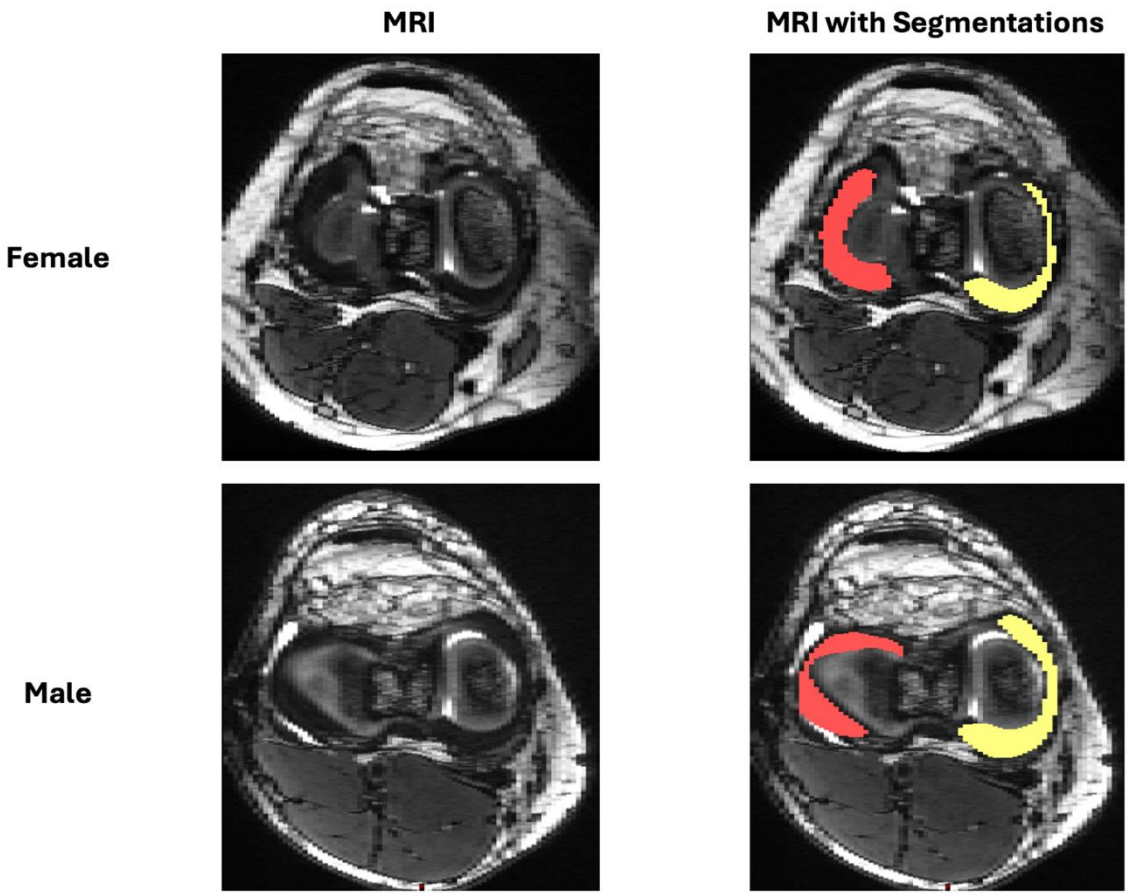

Figure 9. Axial view of a MRI of average knee sized female (top row) and male (bottom row) without (left column) and with (right column) segmentation masks where the lateral meniscus is masked in red and the medial meniscus is masked in yellow.

4.3.3 Imaging Outcomes

The CSA and corresponding SI values from the segmented menisci were analyzed using a custom MATLAB script (Mathworks). Each meniscus segmentation resulted in a mesh composed of faces and vertices.[106] Principal component analysis (PCA using Statistics

and Machine Learning Toolbox in MATLAB R2023a) was performed on the vertex coordinates to identify the primary anatomical axes for each mensici.[105] After transformation, the coordinate system had been orientated relative to the meniscus, where the Z-axis was orientated in the superior-inferior direction, the Y-axis in the anterior-posterior direction, and the X-axis in the medial-lateral direction. The transformations ensured that the coordinate system had the positive X-axis consistently pointed towards the center of the joint and the positive Z-axis pointed in the superior direction. However, due to the orientation of the X and Z axes, depending on the meniscus (lateral or medial) and the limb (right or left), the positive Y-axis would point either towards the anterior or posterior region of the meniscus.

The Taubin Circle Fit method was then used to fit a circle to the outer meniscus rim in the XY plane (Circle Fit (Taubin Method) version 1.0.0).[172] The center of which was used to standardize meniscal orientation and facilitate inter-patient comparisons.[172] The CSA measurements were incrementally performed at discrete steps along the arc length of the outer meniscus rim (Figure 10). These steps were located at approximately 2.5-degree increments to create sixty equally spaced sections, which were then normalized from 0 to 100% of the meniscus arc between the anterior root and posterior root insertions (Figure 10).

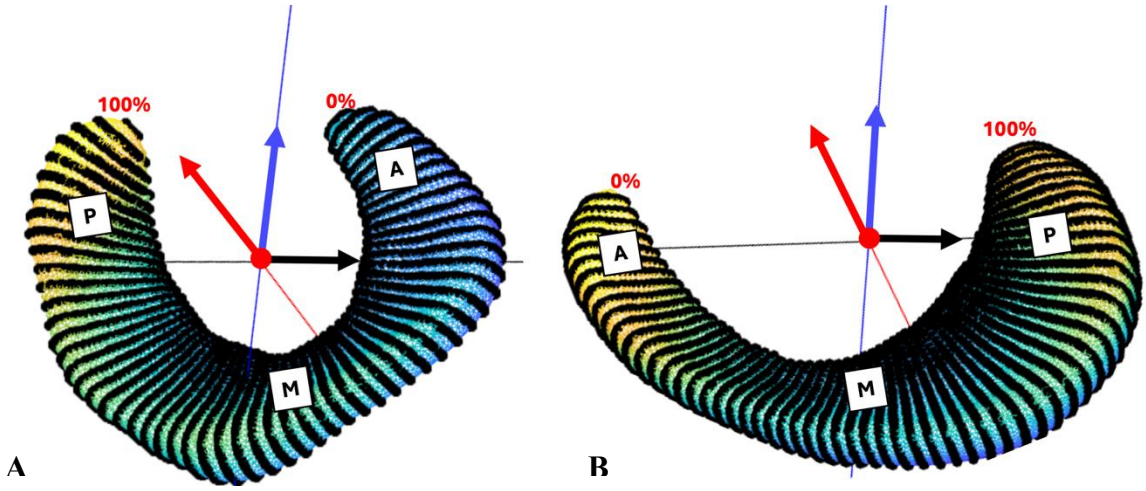

Figure 10. The sixty equally spaced CSA measurements taken over the arc of the lateral (A) and medial (B) meniscus shown by the black lines. Regions of the meniscus are denoted as [A] Anterior, [M] Middle, and [P] Posterior. The meniscal coordinate system: Superior-inferior axis (red), medial-lateral axis (blue)and anterior-posterior axis (black)

At each angular step, the CSA of the 3D meniscal surface in a plane perpendicular to the meniscus (i.e., along the z-axis) was computed along with the average SI (Figure 11). In addition to the CSA measurement, the mean SI within the intersecting region was calculated by averaging the voxel SI values corresponding to the intersected area. The same MR images were also used to measure the bicondylar width of the femur at the level of the popliteal groove in the coronal plane, measured with a straight line from the lateral to the medial epicondyles.[111] The CSA was normalized by dividing the patients' CSA values by their bicondylar width to ensure that accurate comparisons could be made between knees of various sizes.[80,121] The SI was normalized using a previously established post-processing protocol for ACL MR image analysis, which accounts for variations in noise texture across different MR scanners.[49] Although all images were acquired on the same scanner, normalization was applied to align with previously established workflows. This normalization method (Eq. 2) incorporated the SI of the anterior cortex of the femur (SI_{Bone}) with the SI of the meniscus slice ($SI_{Meniscus}$) ,

which is then log-base 2 transformed and scaled using the measure of background noise ($\Delta Noise$) to calculate the normalized SI of the meniscus slice ($SI_{Normalized}$).[49]

$$SI_{Normalized} = \log_2\left(\frac{SI_{Mensicus} + \Delta Noise}{SI_{Bone} + \Delta Noise}\right) \quad \text{(Eq. 2)}$$

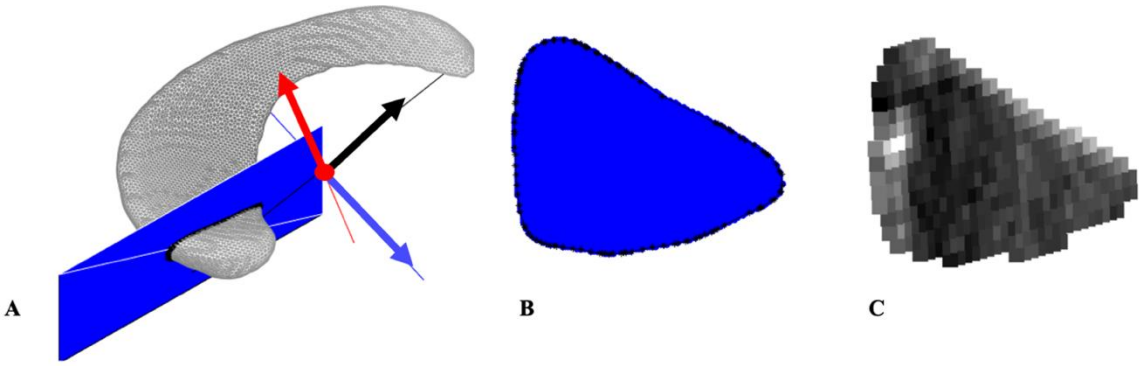

Figure 11. (A) Intersection of a plane to the 3D meniscus (B) the meniscal CSA and (C) the corresponding SI values. The meniscal coordinate system: Superior-inferior axis (red) medial-lateral axis (blue) and anterior-posterior axis (black).

4.3.4 Statistical Analysis

CSA, normalized CSA, and normalized SI values were extracted from both menisci to generate a continuous morphological profile at equally spaced intervals along the entire arc length. Mean values and corresponding 95% confidence intervals (CIs) were plotted to illustrate the CSA, normalized CSA, and normalized SI changes along the normalized arc length. Statistical Parametric Mapping (SPM, som1d MATLBA toolbox) was used to statistically compare CSA profiles between females and males.[134] The resulting SPM output included unpaired t-test statistics across the arc length of the meniscus, to highlight the regions that were significantly different. SPM utilizes Random Field Theory (RFT) to calculate the critical threshold for the t-statistic continuum, which accounts for the smoothness of the measurements calculated across the arc length.[134] RFT was shown to provide better correction than the standard Bonferroni correction because Bonferroni

assumes every point on the curve is independent, resulting in too many false negatives.[134] RFT adjusts to the specific search space of the curve or region of interest (ROI) and the continuous smoothness of the data to apply a correction factor to provide a proper correction to the t-test statistics across the arc length of the meniscus.[134]

4.4 Results

4.4.1 Cross-Sectional Area

The mean CSA values for the males were significantly greater than those of the females along the entire arc length for the lateral (Figure 12) and medial (Figure 13) menisci. The maximum mean standard deviation differences between the sexes were 6.0 ± 1.9 mm^2 and 8.0 ± 1.6 mm^2 for the lateral and medial menisci, respectively.

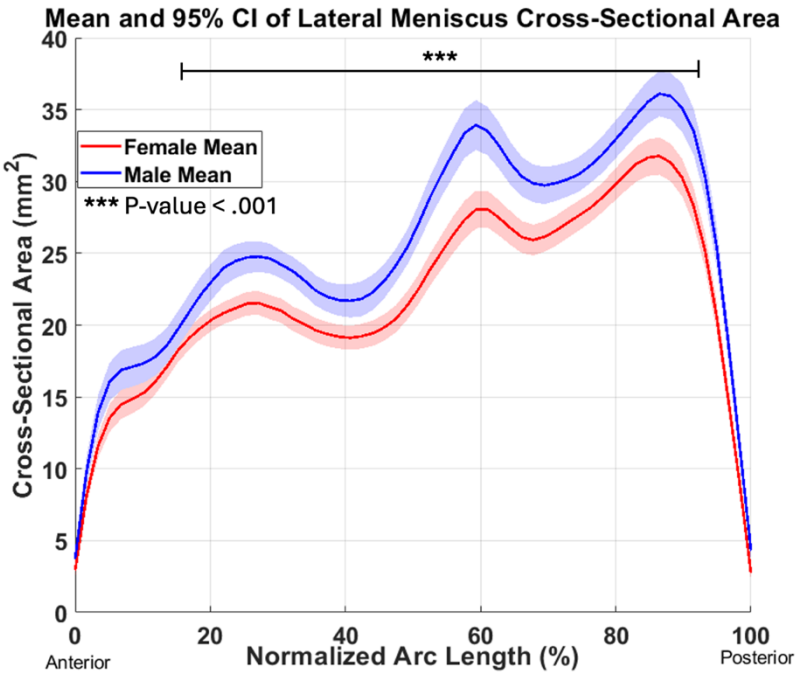

Figure 12. Mean and 95% Confidence Interval of the Lateral Meniscus (Unnormalized) CSA between Females and Males. The regions significantly different between males and females are marked by the horizontal bar.

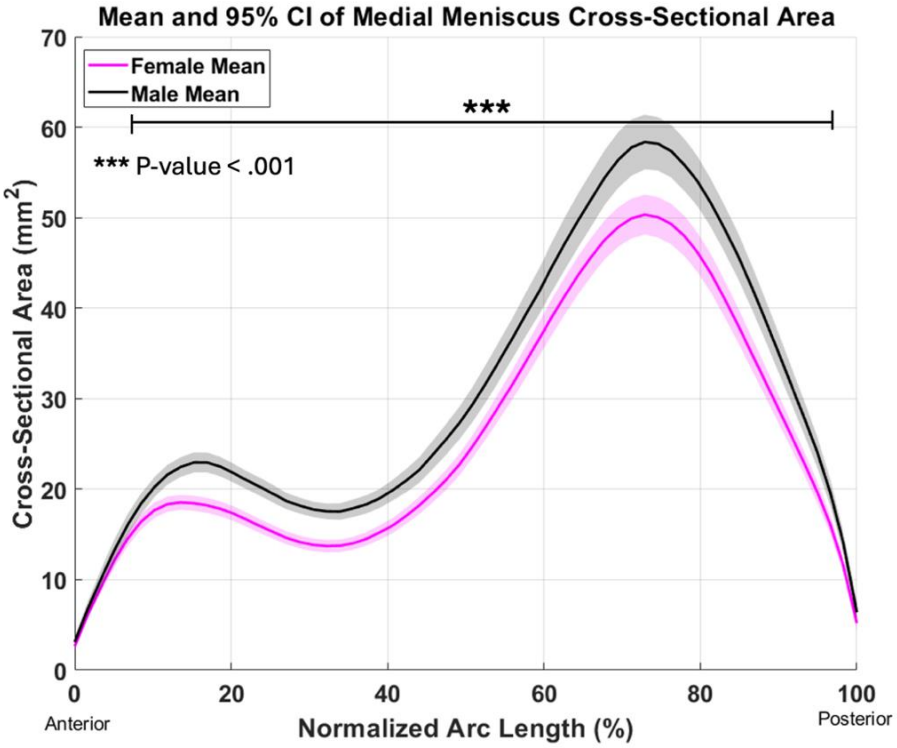

Figure 13 . Mean and 95% Confidence Interval of the Lateral Meniscus (Unnormalized) CSA between Females and Males. The regions significantly different between males and females are marked by the horizontal bar.

4.4.2 Normalized Cross-Sectional Area

The normalized CSA patterns varied along the lateral meniscus arc length. The largest normalized CSA was in the posterior region of the lateral meniscus in both males and females (Figure 14). There were no significant regional differences in lateral meniscus normalized CSA between females and males.

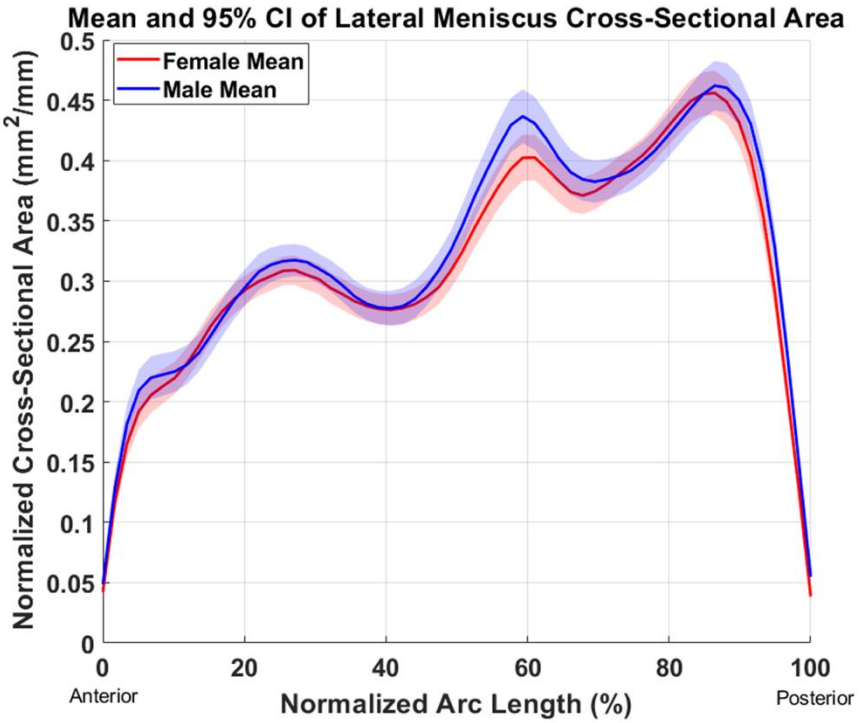

Figure 14. Mean and 95% Confidence Interval of the Lateral Meniscus Normalized CSA between Females and Males.

On average, the medial meniscus had similar normalized CSA patterns between females and males (Figure 15). The peak normalized medial meniscus CSA was between 70-80% of the meniscus arc length for both sexes. There were significant differences in the normalized medial meniscus CSA between females and males in the anterior region of the meniscus (arc length range: 10-45%), with females having a smaller CSA than males by 0.04 mm^2/mm ($P < .001$) (Figure 15).

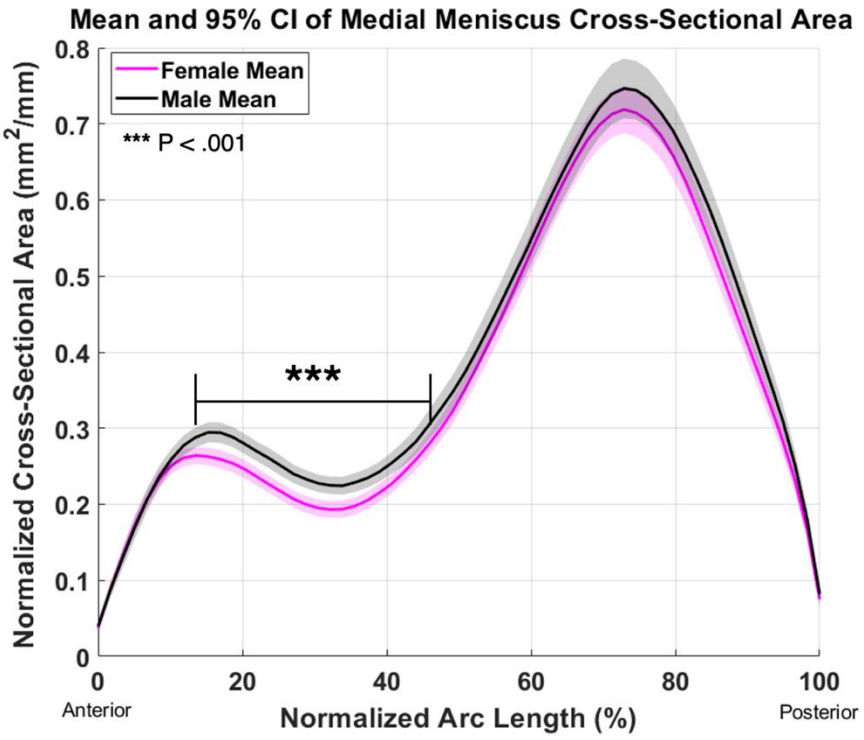

Figure 15 . Mean and 95% Confidence Interval of the Medial Meniscus Normalized CSA between Females and Males.

The bicondylar widths used for the CSA normalization of the female and male subjects had mean values of 70.3±4.87 mm and 77.1±4.13mm, respectively, values that were significantly different ($p < .001$). The average volumes and standard deviations of the lateral and medial menisci were calculated for the sexes, along with the minimum and maximum range. The lateral meniscus for males had an average volume of 1856.9±235.5 mm^3 (1261.4 – 2410.4 mm^3) while the average volume for females was 1447.59±225.4 mm^3 (1053.4 – 1972.99 mm^3). The average volume of the male medial meniscus was 2049.1±375.0 mm^3 (1280.0 – 3323.0 mm^3), while the female average was 1618.9±326.5 mm^3 (1002.4 – 2336.1 mm^3) (Figure 16).

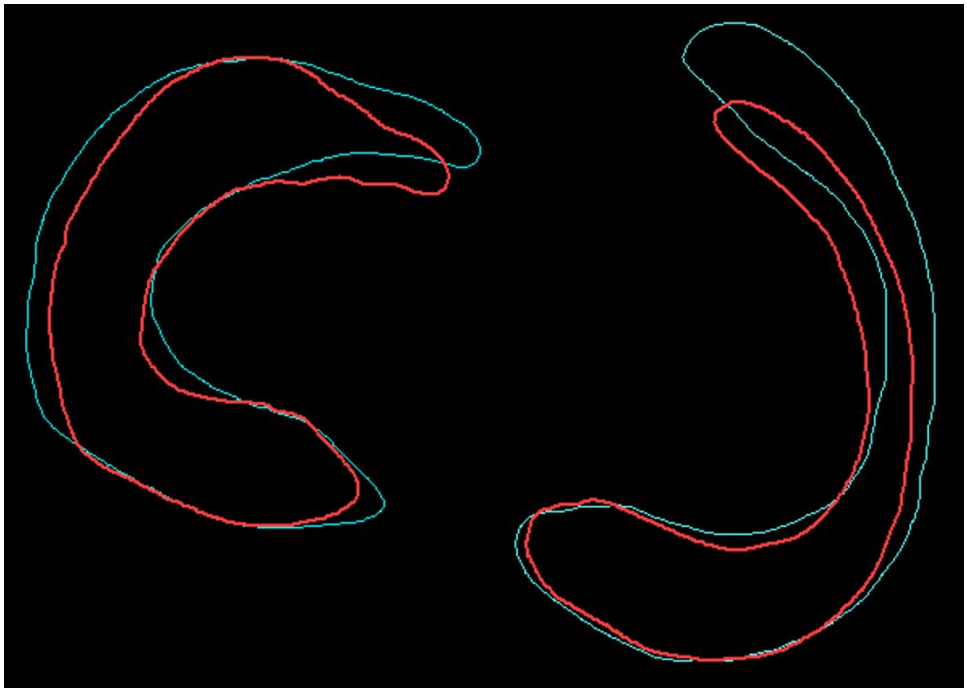

Figure 16. Contour comparisons between an average knee sized male (cyan) and female (red) lateral (left) and medial (right) menisci.

4.4.3 Normalized Signal Intensity

On average both females and males followed similar patterns with the highest average normalized SI in the anterior region of the lateral meniscus (range: 0-10%) The mean peak normalized SI values for the males and females were 0.78 ± 0.13 and 0.77 ± 0.12, respectively (Figure 17). The highest mean normalized SI was in the posterior region (range: 90-100%) of the medial meniscus with the female mean peak SI of 0.71 ± 0.13 and the peak male SI of 0.72 ± 0.13 (Figure 18). No significant differences were found in the lateral or medial menisci normalized SI profiles between females and males.

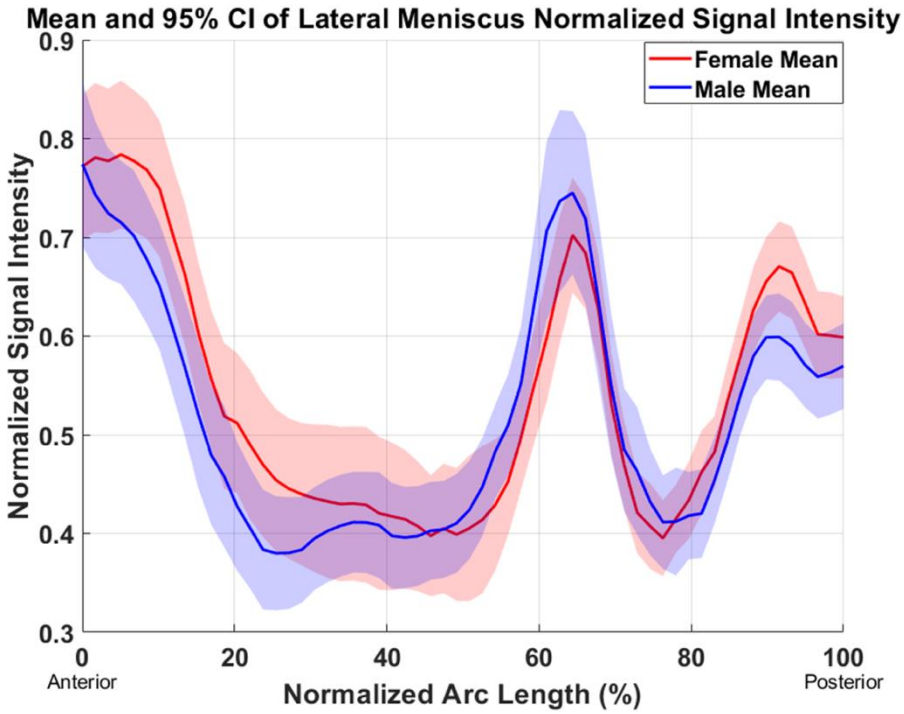

Figure 17. Mean and 95% Confidence Interval of the Lateral Meniscus SI between Females and Males

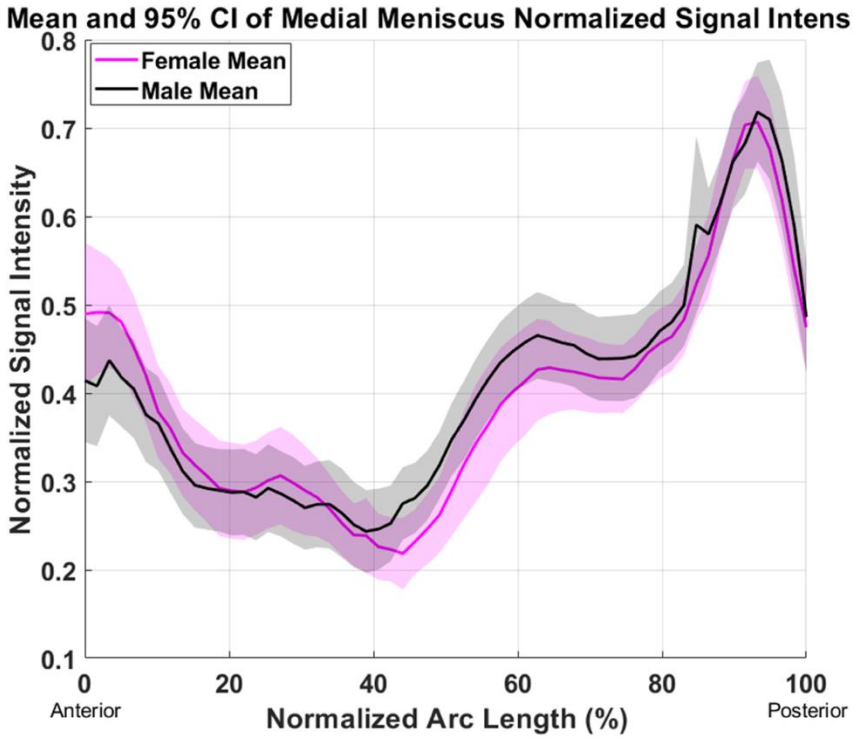

Figure 18. Mean and 95% Confidence Interval of the Lateral Meniscus SI between Females and Males

4.5 Discussion

This study demonstrated a novel methodological approach to detect differences in CSA and SI profiles along the arc length of the menisci between females and males. The current findings suggest that females and males have similar CSA profiles in the medial and lateral menisci. The CSA values of the menisci are dependent on knee size, as there were significant differences found along the entire arc length of both the medial and lateral menisci when the CSA values were not normalized to knee size. Females consistently had smaller meniscal CSA values. To account for knee size variations between males and females and to properly compare meniscal size differences, the CSA s were normalized to the bicondylar width.[111] When the CSA values were normalized, significant differences were only found in the medial meniscus, with females exhibiting smaller values in the anterior region. The findings do no support our initial hypothesis in stating that females would have significantly smaller menisci when normalized for knee size, as the CSAs were only significantly smaller when not normalized for knee size. As hypothesized, no significant differences were found in the SI values along the arc length between females and males, as the knees analyzed in this study were not injured.

Increased SI of the meniscus has been used to detect pathologic alterations.[63] A high SI indicates the location of an injury.[63] Previous research has also shown that the magnitude of SI is directly related to the severity of meniscal degeneration.[195] Studies have reported that the mean SI of the medial meniscus was significantly higher in arthritic knees compared to non-arthritic knees.[192] To our knowledge, no studies have investigated regional differences in normalized SI between sexes in uninjured knees. There were subtle differences in signal intensity profiles between the lateral meniscus,

which ranged from approximately 0.3 to 0.8, while the medial meniscus ranged from approximately 0.2 to 0.7. Regional meniscal signal intensities likely reflect vascularization and microstructural differences such as water content and collagen orientation.[104] The normalized SI values reported in this study were similar between sexes, suggesting that the material properties of the tissue may be consistent between females and males. Thus, this study provides baseline data that would be useful for future studies investigating the role that knee injury may play in the integrity of the meniscal tissue whereby normalized SI's that exceeded the threshold of 0.70-0.78 ($\pm$0.12) may be indicative of injury or tissue degeneration. Future studies could also examine longitudinal changes of SI in injured limbs to better understand how injury affects meniscal SI values and PTOA in females and males.

The lateral meniscus exhibited location-dependent variation in CSA along the arc length. In the lateral meniscus, normalized CSA peaked between 80-90% of its arc length, with males showing a slightly higher peak than females. Similarly, the medial meniscus CSA peaked in the posterior region (70-80% of the arc length). The larger normalized CSA of the lateral and medial meniscus in the posterior region correlates with the location where the menisci experience the highest pressure on the cartilage.[184] There was a significant difference in the normalized CSA observed in the anterior portion of the medial meniscus (9-23% of the arc length) between males and females. The anterior region of the medial meniscus plays a role in transmitting hoop stresses, particularly during full knee extension, and controlling anterior femoral displacement.[183] The sex implications of this are unknown. Nonetheless, these findings indicate that while the general shape and distribution of both meniscal CSA values are similar between sexes,

localized regions, especially in the anterior medial meniscus, show measurable differences that may have implications for sex-specific risk of injury.

The CSA observations found in this study are in line with prior reports of overall sex differences in meniscus size.[2,40,55,78,93,101,132] These data show that when normalizing CSA values by knee size, significant differences between the sexes remain present in the medial meniscus. Previous research has reported that males, on average, have a 5-mm larger femoral anteroposterior dimension than females. Studies have also reported overall smaller tibial mediolateral dimensions and tibial mediolateral/anteroposterior ratios in females than males.[101] Additionally, studies have reported significant meniscal size sex-based differences.[88] The current study builds on previous work as it determined that normalizing the CSA values by knee size, significant differences between the sexes was only present in the medial meniscus.

Although females are overall smaller than males when compared on a population level, a smaller meniscus CSA can be associated with higher stress, and potentially higher injury risk, especially in the presence of small changes in CSA, which can disproportionately elevate stress and promote PTOA.[40] Although only sex-based differences in the normalized CSA of the medial meniscus were identified in this study, they may not fully explain the higher incidence of knee PTOA or injury risk observed in females compared to males. A variety of additional intrinsic factors, such as differences in tissue composition, hormonal influences, and anatomical variations in surrounding joint structures, likely contribute to these disparities as well. These elements may interact in ways that influence joint mechanics and cartilage health. Future investigations should focus on the longitudinal evaluation of the changes in meniscal morphology in an injured

knee to determine how these intrinsic differences evolve over time and which ones may exacerbate sex-specific risks. Such insights could help identify the mechanisms that contribute to the increased risk of knee PTOA and inform prevention or treatment strategies.

There are several important study limitations to consider. First, the data were derived from the contralateral, uninjured limb of patients who had experienced a unilateral ACL injury. The ipsilateral ACL injury could introduce bias, as individuals with a history of ACL injury could possess intrinsic factors that predispose the knees and menisci to injury or degeneration. Second, previous studies have demonstrated that tibial and femoral cartilage thickness values decrease during physical activity, with the cartilage height gradually returning with rest, and the same response may also be true for meniscal tissue.[17] In the present study, we did not implement a standardized rest protocol before imaging, and therefore, there is some uncertainty about whether patients' menisci were under the influence of prior weight-bearing or activity-induced compression that could potentially influence the CSA measurements. To improve consistency and physiological relevance, future studies could implement a controlled unloading period before imaging and/or conduct the imaging within a consistent time of day to ensure that menisci are assessed in a standardized, non-compressed condition that better reflects the baseline geometry in the absence of loading. Future studies could use this approach to provide quantitative changes of CSA and SI between the patient's surgical and contralateral limb to identify differences in meniscal integrity post-ACL surgery. The inclusion of Finite Element Analysis of the tissue, along with this robust method of evaluating the menisci, would further advance the progress towards personalized

rehabilitation strategies (Appendix A). By identifying these baseline differences prior to surgical intervention, we can ensure that subsequent analyses of post-surgical tissue changes can be interpreted within the context of known anatomical variation.

Our findings provide a practical alternative method for meniscal assessment that is more robust than traditional approaches, such as single-slice measurement or averaged analyses. First, anatomical location selection should be explicitly defined and standardized, as our data demonstrate that meniscal morphology and signal characteristics naturally vary across the region regardless of sex. Measurements obtained from a single slice or generalized by a region may not reflect the meniscal properties and may exclude localized differences. Based on our analysis, the anterior horn of the medial meniscus demonstrated the greatest difference with regard to CSA measurement between the sexes. This region may be particularly important and suitable when a single-location measurement is absolutely required. However, if feasible, we recommend sampling consistently, such as along defined regions in a step-wise manner along the meniscal arc length rather than relying solely on mid-body slices or averaging along the total arc length to improve reproducibility and allow for further comparisons across studies.

This study offers new insights into the heterogeneity of meniscal CSA and SI along the arc lengths of both menisci. Sex-based differences in CSA, even when adjusting for knee size, are present, though there are no differences in the normalized SI. The SI finding indicates that there are no regional differences in the tissue integrity between the sexes in a healthy knee. The study emphasizes the importance of accounting for anatomical location when evaluating meniscal morphology in females and males.

CHAPTER 5: Longitudinal Mapping of Meniscal Morphology After ACL Surgery

Longitudinal Quantitative Mapping Reveals Persistent Meniscal Morphological and Signal Intensity Differences After ACL Surgery

Dominique A. Barnes, Crystal J. Murray, Mohammadreza Movahhedi, PhD, Jillian E. Beveridge, PhD, Ata M. Kiapour, PhD Martha M. Murray, MD Braden C. Fleming, PhD

The following chapter is currently under review in *The American Journal of Sports Medicine.*

5.1 Abstract

Meniscal tears are frequently associated with ACL injuries. Evaluating longitudinal changes in meniscus integrity using qMRI following ACL surgery may provide valuable insight into joint recovery and subsequent reinjury risk. We hypothesized that the CSA and normalized SI profiles of the lateral and medial menisci for the surgical knees would be greater than those of the contralateral uninjured knees observed at 6-, 12-, and 24-months post-surgery. We also hypothesized the CSA and SI profiles obtained at 24-months would be closer to those of the contralateral limb when compared to those of the 6- and 12-month time points. Deidentified post-surgical MR images of patients (n = 82; median age 17.6 years; 42 females and 40 males; 57 ACL restoration and 25 ACL reconstruction) were analyzed. CSA and normalized SI values were extracted from the lateral and medial menisci to create morphological profiles. Statistical Parametric Mapping (SPM) was used to compare the CSA and normalized SI profiles between the surgical and contralateral limbs to identify specific regions that were significantly different along the menisci at 6-, 12-, and 24-months. The CSA and normalized SI profiles of the anterior region of the medial menisci and lateral menisci for the surgical knees were greater than those of the contralateral uninjured knees, observed at 6-, 12-, and 24-month post-surgery, while the posterior region CSA of the medial menisci was smaller. The lateral meniscus on the operated limb had a larger CSA and higher normalized SI values than the lateral meniscus in the contralateral limb. The CSA and SI profiles obtained at 24-months did not approach those of the contralateral limb when compared to those of the 6- and 12-month time points. There were significant changes that occurred in both menisci post-ACL surgery that did not return to baseline levels

within 24 months. It is important to account for anatomical location when evaluating meniscal morphology in surgical knees and when evaluating the effects of ACL injuries on the surrounding tissues.

5.2 Introduction

The lateral and medial menisci are vital for normal knee function and joint longevity.[52] The menisci transmit load across the joint and decrease the stress placed on the articular cartilage.[52,104] Studies have shown that approximately 40-60% of the axial load from the femur is transmitted to the meniscus.[52,68,164] The wedge-like cross-section of the menisci allows for the tissue to modulate axial loads of the femur into hoop stresses.[34,51] Without the menisci's ability to convert axial stress into hoop stress, greater forces are concentrated onto the articular cartilage, which may lead to its degeneration and , ultimately, the development of OA.[34,104]

Meniscal tears are frequently associated with ACL injuries.[27,59,125] A previous study reported that concomitant meniscal injuries occurred in 61% of the patients presenting with an ACL injury, with the prevalence of concomitant lateral and medial meniscus injuries reported to be 48% and 25%, respectively.[145] Injury to the menisci and subsequent treatment, such as partial or complete meniscectomy, has been associated with an increased risk of reinjury to the ACL and increased risk of PTOA in patients who undergone ACL reconstruction surgery.[59,107,108,130,162]

Recovery and risk of reinjury for patients who undergo ACL surgery have largely been tracked using patient-reported outcomes, clinical outcomes, and asymmetries in dynamic joint function.[56,98,113,140] To supplement existing metrics, qMRI was introduced to non-invasively assess the structural properties of the ACL or ACL graft.[16,19,80,81,159,178]

Pathologic abnormalities of ligaments and grafts can be observed on qMRI as an increase in the structure's SI, indicating the presence of an injury or tissue degradation.[89] Furthermore, the combination of CSA and SI of the healing ACL has been shown to be predictive of the tissue's strength as well as revision risk within 2 years after ACL surgery.[8,14,16] qMRI has been used to quantify meniscal healing as well.[146] Ex vivo studies have shown that qMRI metrics can be reflective of morphological differences in the meniscus.[122,123] An in vivo human study further supported that qMRI metrics, specifically UTE-T2* mapping, are sensitive to meniscal compositional changes.[26] For this study, SI and CSA were included as qMRI metrics to be evaluated due to clinical relevance for the assessment of ACL pathologies during the rehabilitation period. Evaluating longitudinal changes in meniscus integrity using qMRI following ACL surgery may provide valuable insight into joint recovery and subsequent injury risk.

The objective of this longitudinal study was to evaluate early morphologic changes of the lateral and medial menisci using qMRI. Measurements were taken at 6, 12, and 24 months post-surgery in patients that underwent either ACL reconstruction or ACL restoration (Bridge-Enhanced ACL Restoration) surgery.[118,119] The CSA and SI profiles of the lateral and medial menisci were compared between surgical and intact contralateral knees. This comparison aimed to identify post-surgical morphological changes in the menisci. It was hypothesized that the CSA and SI profiles of the lateral and medial menisci of the surgical knees would be greater than those of the contralateral knees at all time points. Additionally, it was hypothesized that at 24 months, the CSA and SI profiles would align more closely to the contralateral limb than at earlier time points.

5.3 Methods

5.3.1 Data Source

Deidentified MR images of patients enrolled in the IRB and FDA approved ACL restoration trials (clinicaltrials.gov; NCT02292004; NCT02664545) were utilized in this study (n=82; median age 17.6 (range: 13-35) years; 42 females and 40 males; 57 ACL restoration and 25 ACL reconstruction) (IRB#:P00012985 and P00021470), both of which were performed at Boston Children's Hospital (Figure 19). [118,119] All subjects granted their informed consent. The included patients underwent unilateral ACL surgery, either ACL restoration or ACL reconstruction, and were pooled together for this analysis to increase sample size. The patients returned at 6, 12, and 24 months to undergo MR images of both knees. Patients with a reported injured or discoid menisci in the contralateral knee at the time of MR image acquisition or missing MR images at any of the three time points were excluded from this analysis (Figure 19).

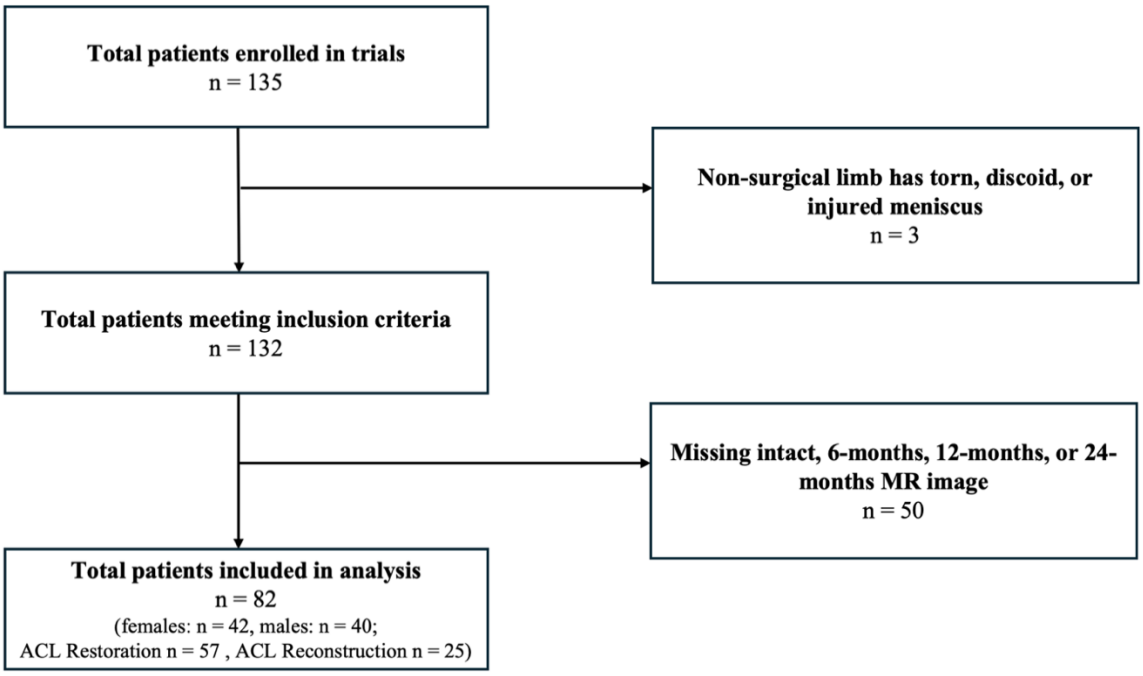

Figure 19. STROBE (Strengthening the Reporting of Observational Studies in Epidemiology) diagram detailing the flow of patients through the analysis.

Patients that had meniscal tears in their surgical limb were included in this analysis. Of the 82 patients included (Figure 19), 58 patients (71%) had reports of meniscal tears in their surgical limb (Table 6). At the time of surgery, 36 patients presented with lateral meniscal tears in the posterior region, accounting for 44% of the patient population, with 18 counts (22% of the patient population) of the posterior medial meniscus tears recorded at the same time point (Table 6).

Table 6. Reported Meniscus Injuries at Various Time Points

	At Time of Surgery	6-Months	12-Months	24-Months
Lateral Meniscus				
Anterior	3	1	0	2
Middle	3	1	1	1
Posterior	36	8	1	2
Medial Meniscus				
Anterior	0	0	0	2
Middle	2	0	0	1
Posterior	18	8	4	5

5.3.2 Surgical Procedures

The details of ACL restoration and ACL reconstruction procedures have been previously reported.[118,119] The imaging data from the cohort used in this analysis come from two previously published clinical trials.[118,119] Of the total number of patients included in the present analysis, 57 patients underwent ACL restoration, and 25 underwent ACL reconstruction (Figure 19). For the ACL restoration procedure, a scaffold, which was composed of extracellular matrix proteins, was implanted to provide a bridge over the torn ends of the ACL. The scaffold was then saturated with the patient's blood to stimulate the ACL to heal. The ACL reconstruction was performed following a standard procedure using a quadrupled semitendinosus-gracilis autograft.[118] A continuous-loop cortical button was used for proximal fixation and a bioabsorbable interference screw for tibial fixation.[118]

5.3.3 Image Data

MR images of the knees were acquired via the three-dimensional Constructive Interference in Steady State (CISS) sequence (TR/TE = 14/7 msec, FA = 35, 16 cm FOV, 80 x 512 x 512 [slice x frequency x phase]) using a 3T scanner (Tim Trio, Siemens) and a 15-channel knee coil. The images of the surgical knee were acquired at 6, 12, and 24 months. MR images of the contralateral knees were obtained at only one-time point (6-, 12-, or 24-months) to minimize scanner time. The menisci were automatically segmented from each patient's 3D image stack using a 3D UNet based convolutional neural network (Dice coefficient score 0.98).[103] The automatic segmentations were verified by two experienced examiners using commercial image processing software (Mimics v23.0; Materlise).

5.3.4 Imaging Outcomes

The post-processing method used to obtain the CSA and SI measurements from the menisci segmentation has been described in detail in the previous chapter. In summary, the segmented menisci were represented as 3-dimensional meshes, and their principal axes were defined using principal component analysis of the vertices.[105,106] The coordinate systems of each meniscus were orientated such that the Z-axis corresponded to the superior-inferior direction, the Y-axis to the anterior-posterior direction, and the X-axis to the medial-lateral direction. A Taubin circle fit was applied in the mid-zone of each menisci to identify the center point and standardize meniscal orientation for inter-patient comparisons.[172] For both menisci, CSA was computed at sixty equally spaced steps (~2.5 degree increments) along the meniscal arc length, normalized from anterior to posterior root where the anterior region was considered the first third of the normalized

length, the middle was the center third, and the posterior region was the final third of the normalized length (Figure 10).

At each step, the CSA was calculated by intersecting a plane perpendicular to the superior-inferior axis (Z-axis), and SI was obtained by averaging the voxel values that fell within the intersected plane (Figure 11). Differences in CSA were quantified by subtracting the surgical from the contralateral limb values for each meniscus at each step. SI values were normalized for inter-scan variability using a previously described postprocessing protocol incorporating the femoral cortex and scaled using the background noise (Eq. 2).[49]

5.3.5 Statistical Analysis

CSA and normalized SI values were extracted from both the lateral and medial menisci to generate continuous morphological profiles of each meniscus at equally spaced intervals along the entire arc length. Mean values and corresponding 95% confidence intervals (CI) were plotted to illustrate the CSA and normalized SI changes along the arc length. SPM was used to compare the CSA and normalized SI profiles between the surgical and contralateral limbs. All of the patients included in this study underwent imaging of their surgical limb at the 6, 12, and 24 months with the addition of the contralateral limb, therefore, no there were no missing data in this study. The resulting SPM outputs for each meniscus highlighted specific regions that were significantly ($P < .05$) different along the arc length of each meniscus.

5.4 Results

5.4.1 Cross-Sectional Area

There were no significant CSA differences observed between time points (6, 12, and 24 months) for the lateral meniscus of the surgical limb. Significant differences along the arc length of the lateral meniscus were found between the contralateral and surgical limbs ($P < .001$), specifically in the anterior and posterior regions at all time points (Figure 20). On average, the CSA was 27% larger in the surgical limbs' anterior region and a 16% larger difference in the posterior region across all time points.

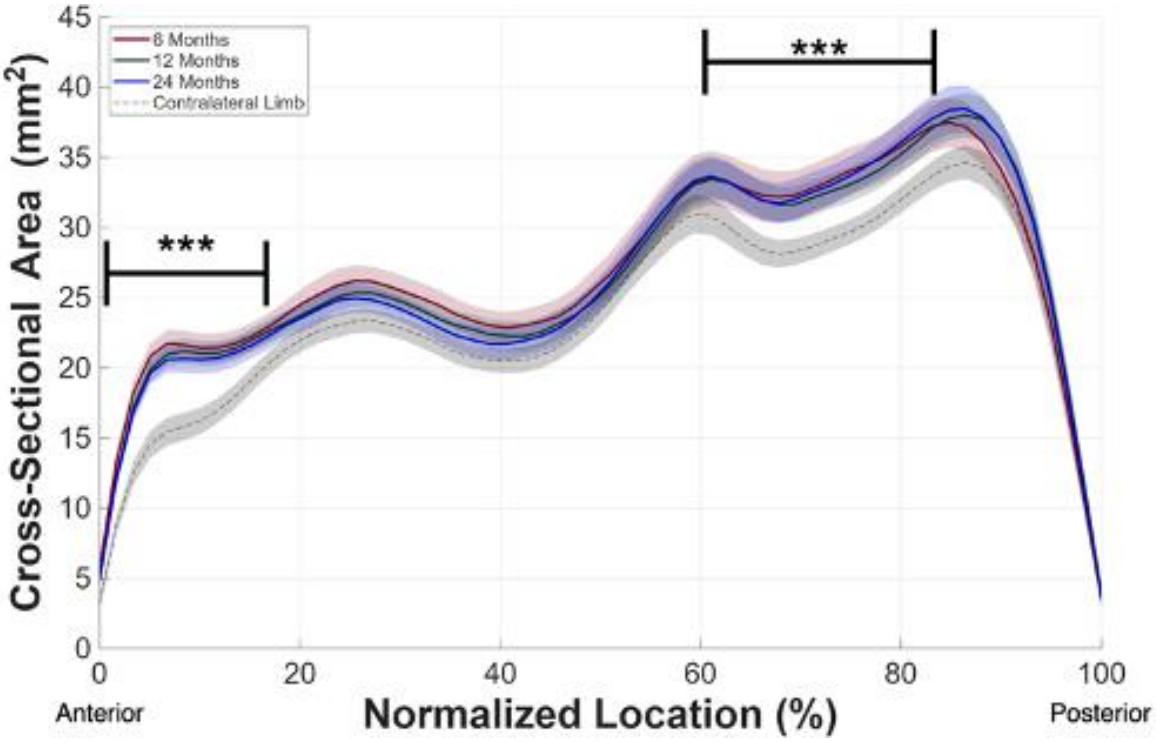

Figure 20. Mean and 95% Confidence Interval (CI) of the lateral meniscus and CSA between the contralateral limb (gray dashed) and the surgical limb at 6-months (blue), 12-months (yellow), and 24-months (red). Significant differences between surgical and contralateral limbs are marked with horizontal bars (***$p < .001$)

There were no significant differences observed between the time points (6, 12, and 24 months) for the medial meniscal CSA of the surgical limb. The CSA of the

surgical limb had a significantly larger CSA in the anterior region compared to the contralateral limb at all time points (p = .014) (Figure 21). On average across all time points, the CSA was 11% larger in the anterior region across all time points, however, the CSA of the posterior region was 10% smaller in the surgical limb compared to the contralateral limb at 24-months (p = .049).

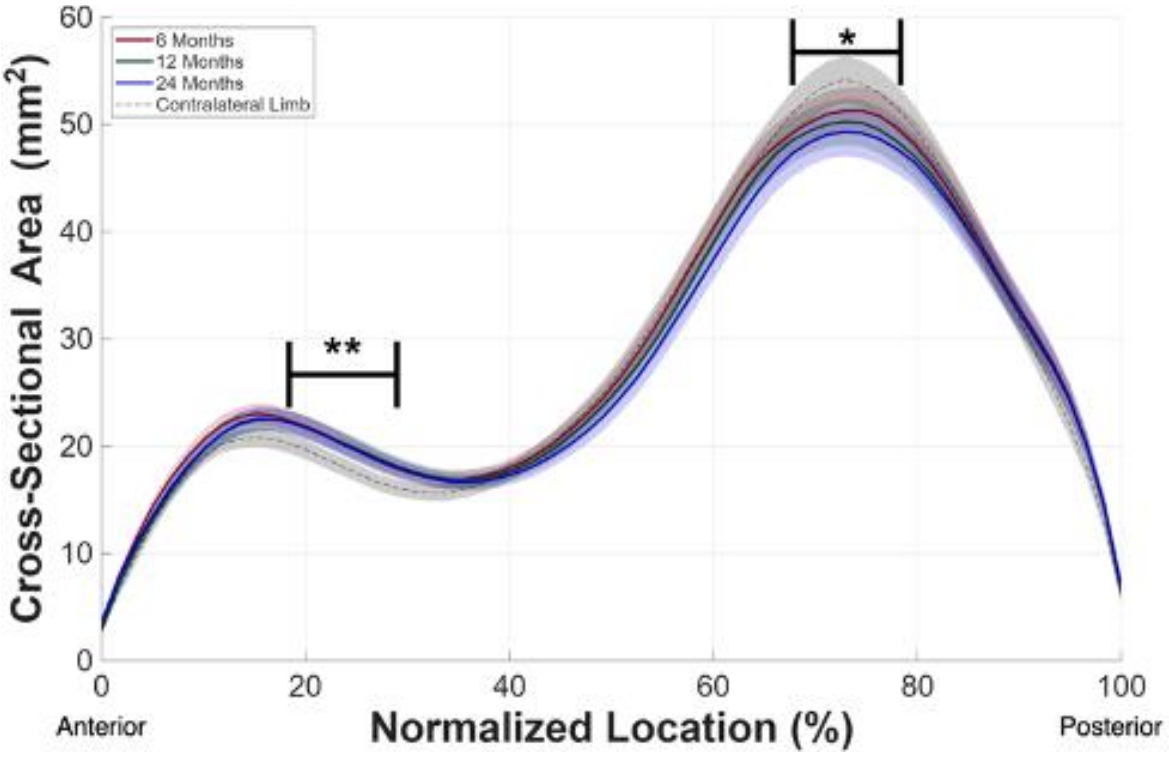

Figure 21. Mean and 95% Confidence Interval (CI) of the medial meniscus CSA between the contralateral limb (gray dashed) and the surgical limb at 6-months (red), 12-months (green) and 24-months (blue). Significant differences between surgical and the contralateral limbs are marked with horizontal bars (**p = .20; *p = .049).

5.4.2 Normalized Signal Intensity

There were no significant differences in the normalized SI profiles for the lateral meniscus imaged at 6, 12, and 24 months in the surgical limb. However, the normalized SI values were significantly higher (p < .001) in the anterior, middle, and posterior regions in the surgical limb compared to the contralateral limb (Figure 22). On average,

the surgical limb has a 15% higher normalized SI compared to the contralateral limb in the anterior, middle, and posterior regions.

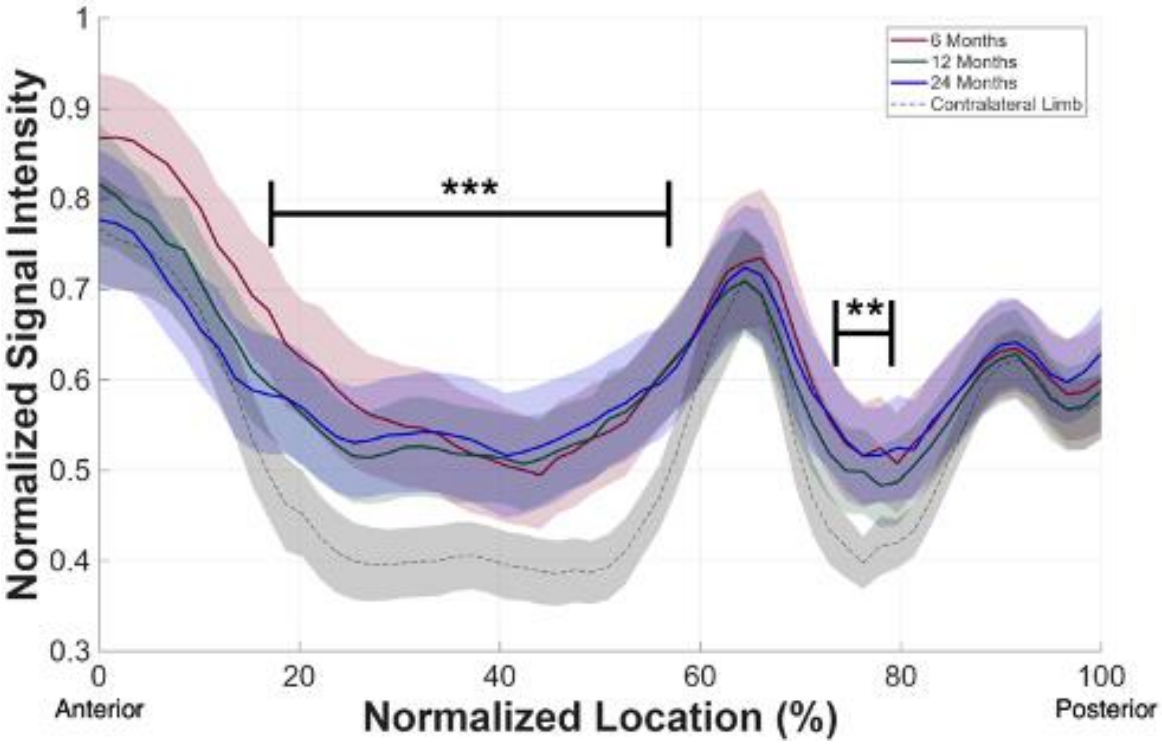

Figure 22. Mean and 95% Confidence Interval (CI) of the lateral meniscus normalized SI between the contralateral limb (gray dashed) and the surgical limb at 6 months (red) 12 months (green) and 24 months (blue). Significant differences between surgical and contralateral limbs are marked with horizontal bars (***p < .001; **p = .010)

No significant differences were detected between time points (6, 12, and 24 months) of the normalized SI profiles of the surgical limbs. A significant difference was found for the normalized SI in the middle and posterior regions of the medial meniscus between the surgical and contralateral limbs (Figure 23). On average, the surgical limb had a 12% higher normalized SI compared to the contralateral limb in the middle and posterior regions.

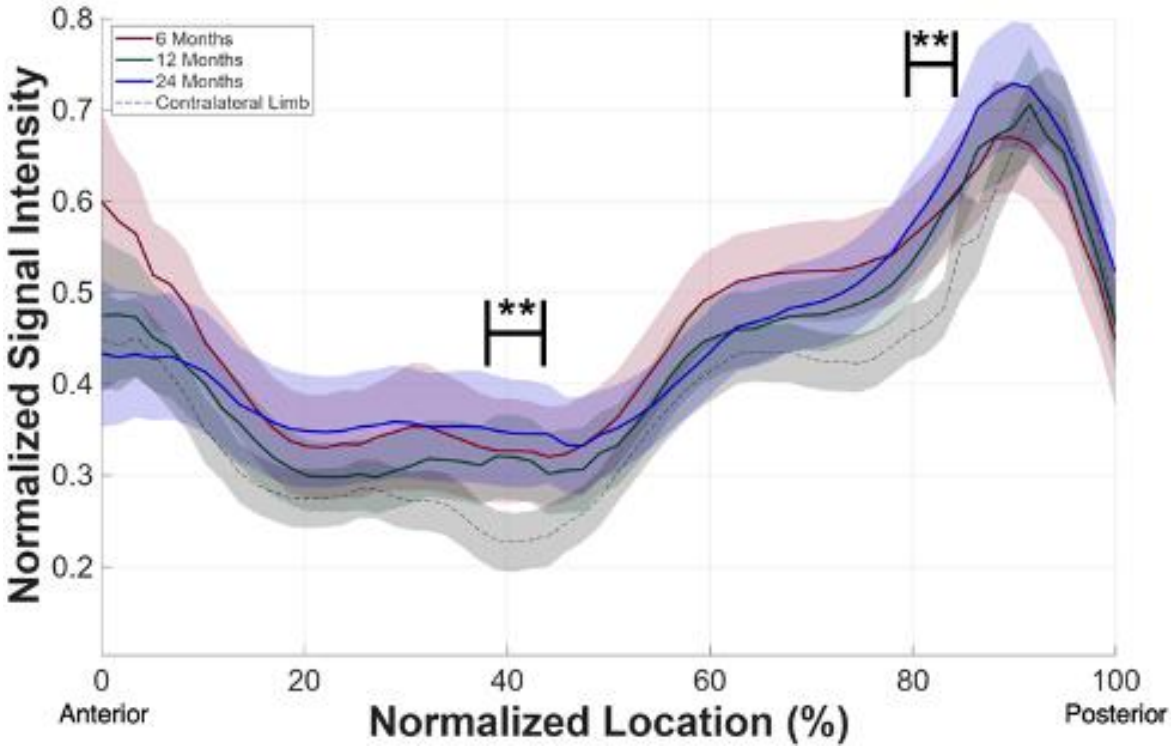

Figure 23. Mean and 95% Confidence Interval (CI) of the medial meniscus normalized SI between the contralateral limb (gray dashed) and the surgical limb at 6 months (red) 12 months (green) and 24 months (blue). Significant differences between surgical and contralateral limbs are marked with the horizontal bars (** p = .020).

5.5 Discussion

The most important finding of the study is that there were significant differences in CSA and normalized SI for both menisci of the surgical limb at all time points when compared to the contralateral limb. As hypothesized, the lateral meniscus has a larger CSA and higher normalized SI values in the surgical limb, which suggests that there may be swelling or remodeling of the tissue, specifically in the anterior and posterior regions post-surgery. The medial meniscus of the surgical limb has a larger CSA in the anterior region throughout time, but the posterior region was found to be smaller and had higher normalized SI than the contralateral limb at 24 months. Contrary to our hypothesis, the

CSA and normalized SI did not return to the contralateral limb's values at 24 months and remained at levels similar to those observed at 6 and 12 months.

qMRI has been used to detect pathological abnormalities through the use of SI, as an increased SI value indicates the presence of injury or tissue degradation.[89] Previous studies have shown the SI magnitude to be a direct representation of the severity of meniscal degeneration, where the mean SI of the medial meniscus was significantly higher in osteoarthritic knees compared to non-osteoarthritic knees.[63,192,195] Comparison between meniscal changes and qMRI values has been found, such as lower T2 values being associated with complete meniscal healing.[146,194] Whereas, an increase in relaxation times in multiple qMRI metric mapping techniques was found to be a measure of degeneration.[122,123] The normalized SI values reported in this study indicate that the surgical limb menisci have undergone structural property changes after the ACL injury despite surgery. These results also show that subsequent changes to the tissue's material property do not return to uninjured levels.

The lateral meniscus CSA was larger in the surgical limb compared to the contralateral limb in the anterior and posterior regions. A pre-operative MRI study of meniscus tears reported a correlation between ACL tears and lateral meniscus posterior tears.[86,128] Ninety-five percent of the patients presenting with a lateral meniscus posterior tear had an ACL injury compared to 14% of patients presenting with a medial meniscus posterior tear.[86,128] These values align with the cohort of patients included in this analysis, where 46% of patients presented with lateral posterior tears at the time of surgery compared to 22% of patients presenting with a medial meniscus posterior tear. The lateral meniscus plays a crucial role in restraining rotational translations.[38] Disruption to the

normal geometry of the lateral meniscus can lead to increased contact forces between the articulating cartilage surfaces during daily activity.[34] The observed increase in CSA in the anterior and posterior regions of the lateral meniscus may reflect alterations in meniscal morphology, such as swelling or tissue remodeling. Previous studies support the link between meniscal pathology changes following ACL injury, as injury to the posterior horn of the lateral meniscus has been associated with damage to the lateral tibial plateau and cartilage defects in the lateral femoral condyle.[71] Our findings demonstrate persistent elevation in meniscal SI, which may reflect early alterations in the meniscal tissue that could potentially contribute to similar degenerative changes.

A primary function of the medial meniscus is to serve as a secondary stabilizer of anterior tibial translation of the knee.[59] The demand of the medial meniscus in resisting anterior tibial loads is increased in the presence of an ACL injury in the absence of the ACL compared to an intact knee.[4] The anterior region of the medial meniscus is crucial for stabilizing external knee rotation, while the posterior region provides stabilization by absorbing approximately 50% of the anterior tibial shear force during full extension.[51,77] Small changes in the geometry of the medial meniscus can disproportionately elevate stress onto the articular cartilage.[40] Previous qMRI studies have shown that qMRI relaxometry values remains high in the articular cartilage of the central medial femoral condyle compared to the contralateral side three years after ACL surgery.[7] Early degenerative changes in the medial articular cartilage have also been observed at 2 years after ACL reconstruction.[176] Small changes in the CSA and the medial meniscus may concentrate stress onto regions of the articulating surfaces, in turn causing further degeneration of the meniscal tissue that would compound any damage sustained at the

time of ACL injury. This initial damage, followed by persistent changes in the structural properties and morphology of the menisci, could potentially accelerate the risk of PTOA, matching what is observed clinically.[192,195] However, a direct cartilage evaluation would need to be included in future studies to make definite conclusions relating changes in meniscal CSA and SI to future PTOA.

As anticipated, a substantial proportion of patients presented with concurrent meniscal injuries either at the time of ACL surgery or post-operatively. Seventy-one percent of patients demonstrated meniscal injury, with the majority occurring in the lateral meniscus, particularly within the posterior region. Lateral meniscal injuries remained consistently high across all time points. There was a progressive increase in medial meniscus injuries, rising from 29% before 6 months to 31% at 12 months and 37% at 24 months. Management of these injuries varied between 6 to 24months. Nearly half of patients with meniscal injury at the time of surgery underwent intervention at the time of surgery, most commonly meniscal repair, though partial meniscectomies and debridement were also performed. In contrast, some procedures were performed between 6 and 12 months, with repairs again predominating. By 24 months, surgical treatment increased, with partial meniscectomy more frequently utilized than meniscal repair. These findings are consistent with prior reports of meniscus injuries in conjunction with ACL injury and suggest that treatment decisions may reflect the timing of the injury detection and the type of tear.[44,126,128,149]

This study has several limitations. An inclusion criterion for this analysis was that the patient must have had their surgical limb imaged at all time points and a contralateral limb imaged at one time point. It should be noted that 62% of patients included in this

analysis had their contralateral limb imaged at 6 months, with the remainder at 12 or 24 months. An assumption was made that the contralateral limb would not change between 6 and 24 months. Therefore, the surgical limb at each time point was compared to the patient's contralateral limb imaged at the earliest time point available. The age of patients included in this analysis ranged from 13 to 25 years. Therefore, the findings reported may not be generalizable to an older or aging population. Future work should incorporate a wider age range to ensure that the findings are applicable to a broader population. There are also inherent limitations to the qMRI measurement techniques. The MR images were acquired using the CISS sequence, which is not a commonly used sequence in clinical practice. The CISS sequence was selected as it provides distinct boundaries between the ACL and menisci in high-resolution images. The addition of the CISS sequence to the routine MRI knee exam would increase scan time. Work is currently underway to adapt the findings from the CISS sequence to other MRI sequences. Finally, the analysis included a relatively small sample size (n=82). Patients from both surgical groups were pooled, which may have limited the ability to detect surgery-specific effects. Nonetheless, minor, non-significant differences were observed, with the ACL restoration group exhibiting lower average normalized SI and CSA compared with ACL reconstruction patients (data not shown). Future large-scale studies with both surgical types would be needed to further confirm the current findings and assess the utility of CSA and SI measurements of menisci in surgical knees in predicting OA.

This study offers new insight into the meniscal CSA and normalized SI profiles in the knees of patients who have undergone ACL surgery. Significant differences were found in the CSA and normalized SI of both the lateral and medial menisci, which

persisted from 6 to 24 months. The lateral meniscus was found to have the greatest differences in both the CSA and normalized SI between the surgical and contralateral limbs, specifically in the anterior and posterior regions. This study emphasizes the importance of accounting for anatomical location when evaluating meniscal morphology in surgical knees and the effects of ACL injuries on the surrounding tissues.

CHAPTER 6: Sequence-to-Sequence MR Image Synthesis using 3D-CycleGAN

Dominique Barnes

6.1 Abstract

This chapter explores a methodological framework for transforming MRI sequences to allow for direct implementation of qMRI into the clinical settings where various sequences are used for soft tissue analysis. The qMRI pipeline discussed in this dissertation has relied on the MRI scans that have been acquired using the Constructive Interference in Steady State (CISS) sequence. The advantages of this sequence are that it provides high-resolution visualization for the ACL tissue in contrast to the bony structures and other soft tissues surrounding the region of interest. This sequence has allowed for the advancements in automatic segmentation of the ACL, as well as the development of quantitative MRI analysis using the CSA and SI of the tissue to predict the failure load and predict patients at a higher risk of reinjury after ACL surgery. However, the Double Echo Steady State (DEES) MRI sequence allows for quantitative analysis of the cartilage and is commonly utilized in the clinic. While both sequences provide high-resolution visualization of the ACL for CISS and cartilage for DESS, their differing contrast mechanisms and signal characteristics limit direct comparability and translation of the current qMRI pipeline. To address this, we developed and evaluated a deep learning method that harmonizes CISS and DESS image domains. The proposed method leverages the CycleGAN model and architecture to attempt to transform the image domains while maintaining the distinct properties that make each sequence important for tissue analysis. However, the method proposed was not successful in transforming between MRI sequences, as the quantitative and qualitative metrics did not meet the threshold of good performance of the model. However, this work established

critical steps toward standardization of MRI sequence-to-sequence transformation to allow for multi-sequence qMRI workflows.

6.2 Introduction

ACL injuries are common in the young and active population.[98] For active patients, the desire to regain function and return to sport is high, thus, surgical treatments such as ACL reconstruction are commonly performed.[98] Lower postoperative patient-reported outcomes, clinical outcomes, and asymmetry in joint function have been used to track ACL reconstruction recovery and approximate reinjury risk.[72,129,144,179] However, studies have shown that patient-reported outcome measurements introduce bias and inconsistency when compared to more objective methods, and none of these outcome measures directly assess the structural integrity of the healing ACL or ACL graft.[24,179] To supplement existing patient-reported, clinical, and functional assessments, non-invasive quantitative imaging methods have been developed to evaluate graft maturity and to estimate the structural properties of the surgically treated ACL and other tissues in the knee using qMRI.[8,80,81]

Previous studies provide evidence that qMRI can detect soft tissue changes early in the degenerative process.[8,16] Collagen organization and tensile strength have been correlated with tissue quality that can be measured with SI, as a lower signal is shown on MRI, indicating a darker appearance and a more organized and mature ligament.[8,16,80,81] The size of the ACL graft and median SI of the healing tissue when combined have been shown to correlate with functional outcomes such as the 1-legged hop test and postoperative patient-reported outcomes.[14]

MR-based SI measurements are influenced by many factors such as image acquisition parameters, underlying hardware configurations, and the sequences used to acquire the images.[49,78] The double-echo steady state (DESS) sequence is an accepted sequence to measure structural properties of cartilage, while qMRI sequences, such as T2*-weighted and T1-weighted are commonly used to measure the ACL structural properties.[13,15,16,161] The constructive interference in steady state (CISS) sequence, which is a T2-weighted sequence, has also been shown to be associated with structural properties of the ACL.[15,121] An advantage of the CISS sequence, as compared to other sequences such as DESS, is enhanced fluid-tissue contrast of the ACL within the joint, which aids post-processing (Figure 24A).[47-49,81] Studies have determined that changes in qMRI parameters from CISS scans, such as SI and CSA of the ligament or graft, can be used to determine the biomechanical and histological integrity of healing structures.[13,15,16] However, DESS is advantageous when visualizing changes in cartilage structure, as the cartilage has a stark contrast compared to neighboring tissue and bone, as well as a relatively rapid acquisition time (Figure 24B). To pool MRI data collected across hospitals and clinical trials, there is a need to identify methods that enable transformation between commonly used MRI sequences, such as DESS, and more research-oriented sequences like CISS, to allow for consistent evaluation of qMRI variables such as SI and to reduce scan times.

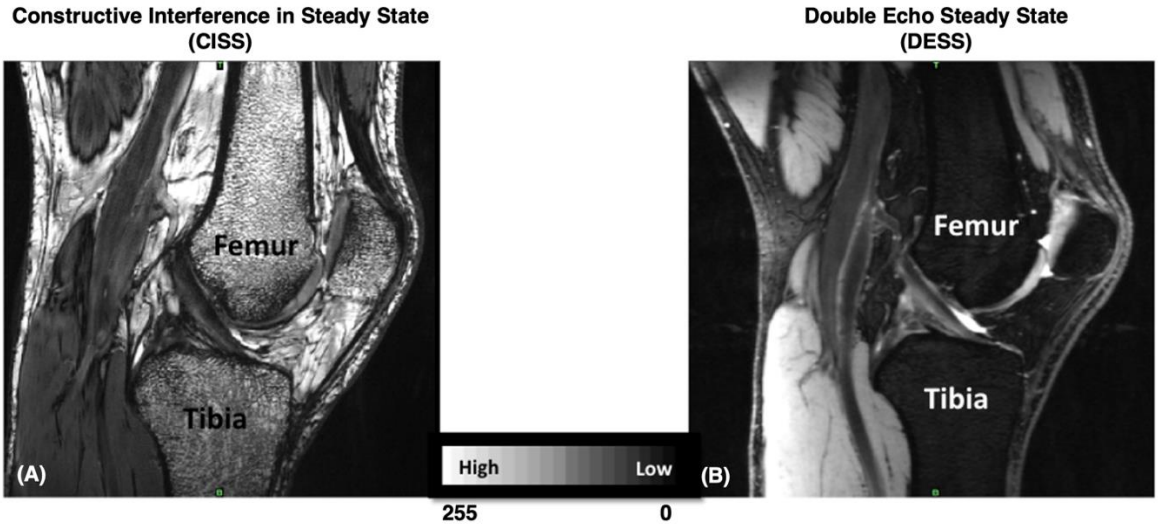

Figure 24. A) Constructive Interference in Steady State (CISS) MRI slice of a knee. B) Double Echo Steady State (DESS) MRI slice of a knee. A signal intensity scale from low (0) to high (255) is included.

To enable consistent evaluation of qMRI SI across MRI sequences, deep learning image generation algorithms could be employed. The introduction of generative adversarial networks (GANs) has advanced the field of generative modeling and data synthesis with growing usage by the medical imaging field due to its ability to generate high quality images.[167] The CycleGAN model developed by Zhu et al., allows for the generation of images without the necessity of paired images, which is advantageous in a medical setting where obtaining paired images for training can be difficult.[197] There are additional advantages to using a CycleGAN, such as the ability to generate images from one source to the target and to reverse the process by generating images from the target to the source image.[197]

It is currently unknown how the predicted failure load can be evaluated from SI values from the more commonly used DESS sequence, as previous studies have only evaluated SI to predict failure load using the CISS sequence.[14-16] If the DESS to CISS sequence transformation were possible, then only one sequence would be needed to

evaluate ACL biomechanical integrity using qMRI. Therefore, the primary purpose of this aim was to determine if CycleGAN can generate MR images from the source domain of DESS to the target domain of CISS. CycleGAN will also allow us to secondarily evaluate how well the model can generate MR images from the source of CISS to the target domain of DESS. The two-way nature of CycleGAN is important because it allows for image translation by learning a reversible mapping between two source domains without the need for a direct corresponding image pair.[197] The two-way nature is ideal in the clinical setting, where requiring multiple MR imaging sequences can be time-consuming and increase the cost of care. It was hypothesized that CycleGAN would successfully generate images from the source domains to the target domains that are qualitatively and quantitatively similar to the ground truth, specifically when evaluating and comparing the average SI of the overall generated image.

6.3 Methods

6.3.1 Data Source

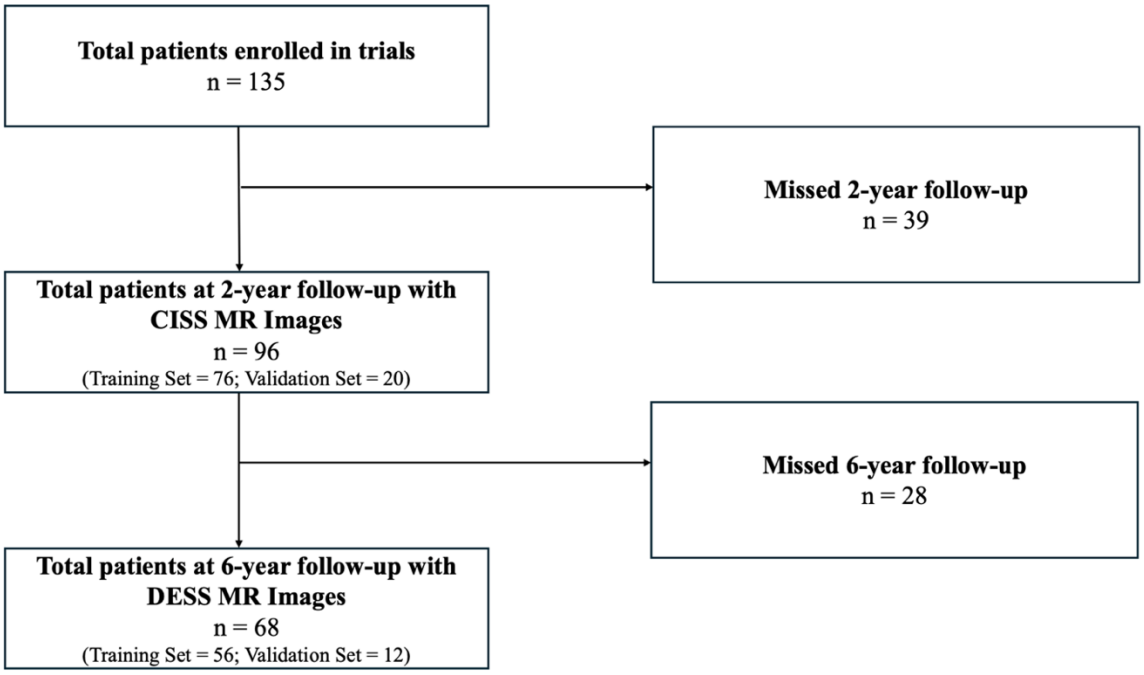

Figure 25. STROBE Diagram of patients included in the analysis.

MR Images were acquired from patients who underwent ACL surgery and were included in one of two ACL clinical trials (Clinicaltrials.gov; NCT02292004; NCT0266545).[50,119,120] All MR images were acquired on a 3T Trio (Siemens) with a 15-channel transmit/receive knee coil (Siemens). There were 96 patients who underwent CISS imaging 2-years post-operation (FA = 35°; TR = 12.78ms; TE = 6.39ms; FOV = 140mm; with voxel size 0.365mmx0.365mmx1.5mm) (Figure 25).[50,119,120] DESS images were acquired from 68 patients who returned for their 6-year follow-up and underwent imaging (FA = 30°; TR = 16.1ms; TE = 5.4ms; slice thickness = 0.8mm; with voxel size 0.300mmx0.300mmx0.800mm) (Figure 25). Only non-surgical limbs were included in

this dataset to ensure that no metallic artifacts would be present during training, to ensure that the model would not create metal artifact hallucinations in the generated images. The DESS data (n=68) were randomly divided into training (~80%; n = 56) and validation (~20%; n = 12) sets for the DESS to CISS transformation (Figure 25). The CISS data (n = 96) were randomly divided into training (~80%; n = 76) and validation (~20%; n = 20) sets (Figure 25) for the CISS to DESS transformation.

6.3.2 Data Preprocessing

Standardization of MR image volume size was done by automatically cropping the original size of 512x512x100 (widthxheightxslice) to 256x256x20 with only the center of the imaging volume retained to ensure the images included the ACL. The raw signal intensities of the MR image volumes were standardized by normalizing the voxel SI values from [0,255] to [-1,1]. Ground truth images were considered the originally acquired CISS or DESS images, depending on the transformation direction, and the model evaluated its performance relative to these ground truth images.

6.3.3 CycleGAN Model

The model training was conducted using a Google Cloud AI Notebook with a NVIDIA T4 GPU (16 vCPUs, 104 GB RAM) with an average time of 6 hours to run the model through 100 epochs. The original CycleGAN model was used to generate 2D images, however, for the use of this application, the model was adapted to train and generate 3-dimensional volumes.[197] The model utilizes two independent generators and discriminators to learn and capture specific characteristics of one collection of images to map and translate those characteristics to another collection of images in the absence of paired training examples.[41,197] The generator architecture was adapted from Johnson et

al., which contains two stride 3-dimensional convolutions, several residual blocks, and two half-stride 3-dimensional convolutions with instance normalization (Figure 26).[41,74,197] In this chapter, the generator that transformed the DESS images into CISS images is referred to as Generator C, while the generator that transformed the CISS images into DESS images is referred to as Generator D. The discriminator networks used a 70x70x20 PatchGAN to classify whether the region of the image patches is real or fake (Figure 26).[197] All networks were trained with a learning rate of 0.0002 using the Adam solver with an Adam optimizer of 10.[74,197]

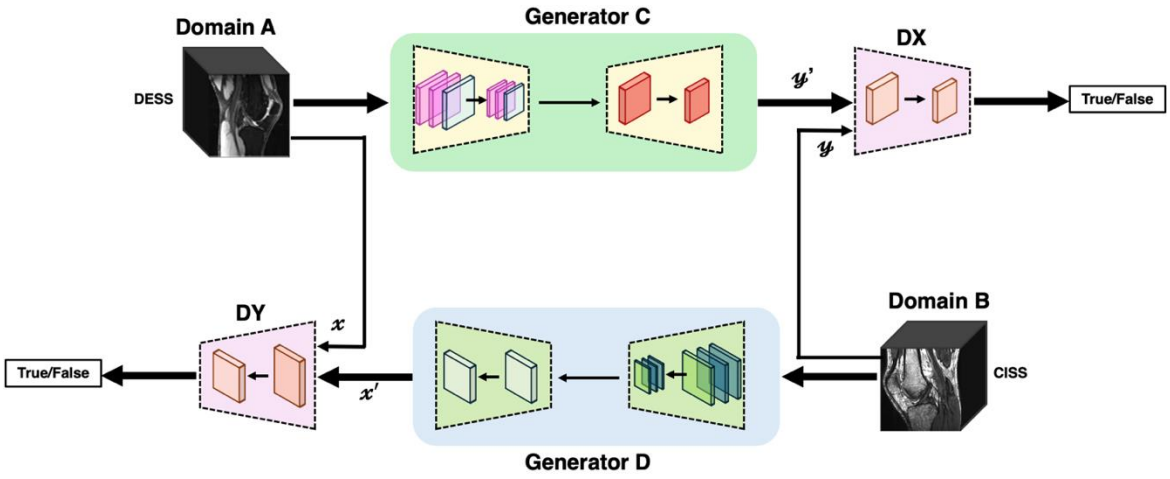

Figure 26. 3-dimensional CycleGAN architecture of (1) Generator C going from input of DESS to output target image of CISS, and (2) Generator D going from input of CISS to output target image of DESS. Both generators feed into a discriminator to distinguish between the true and fake image patches

6.3.4 CycleGAN Performance

The quality of the generated images was compared to the original ground truth images with several metrics. Mean Absolute Error (MAE) was used to measure the average voxel-wise difference between the generated image and ground truth image, with the values bounded by the distribution of the voxel values, -1 and 1, where a MAE value near

1 would indicate a large average difference between the two images' voxel values.[39] For the task of image translation, a good MAE value would be considered 0.15 or below.

A reported 84% of studies within the medical domain conducting image-to-image translation with GANs or convolutional neural networks have used the Structural Similarity Index (SSIM) for validating synthetic images, while 61% of studies have used Peak Signal-to-Noise Ratio (PSNR).[39,109] Therefore, these parameters served as secondary outcomes. Structural information of the generated image was measured using the SSIM quantified by a decimal number between boundaries of -1 and 1, where 1 would indicate perfect structural similarity, a value near zero would suggest no similarity, and a negative value would indicate inverse correlation of the structural similarity.[39] For this application of CycleGAN, a value of 0.8 or greater would be considered fair with regard of maintaining structural similarity. To measure the quality of the generated image on a voxel-level, PSNR was measured by quantifying how much of the signal from the original image was maintained in the generated image compared to the relative corrupting noise introduced during the generating process, with a lower PSNR value indicating more relative noise than true signal intensities.[39] Extremely poor PSNR results would be identified as values below 15dB, often implying that the generated image is heavily corrupted by noise.[31,39] There are no upward bounds to the measurement of PSNR, however, previous studies have shown that an image in which noise has no significant impact would result in a PSNR equivalent or greater than 40dB.[21,82,90]

6.4 Results

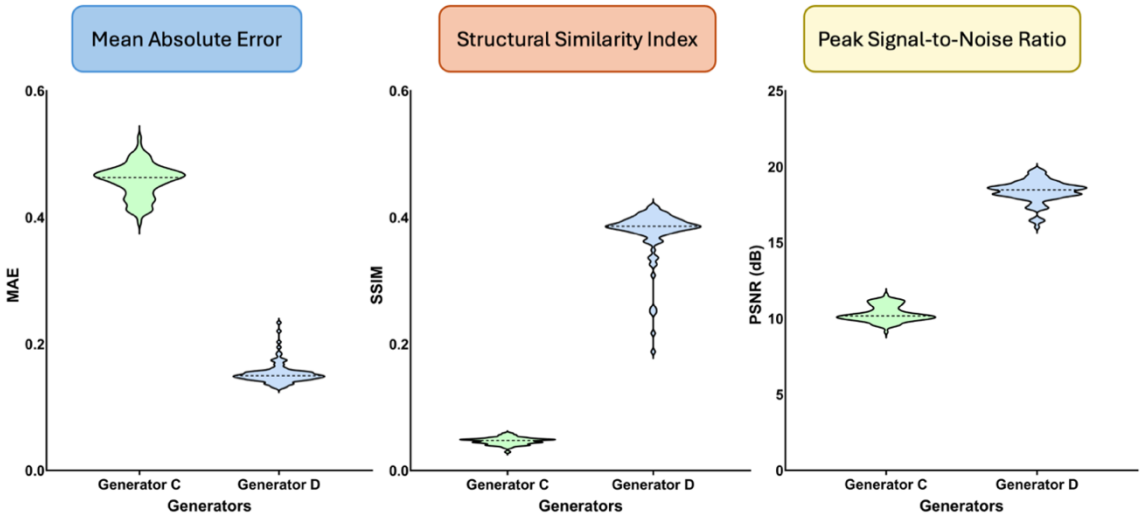

Figure 27. Comparison of Generator C and Generator D based on the following metrics: Mean Absolute Error (MAE), Structural Similarity Index (SSIM), and Peak Signal-to-Noise Ratio (PSNR)

Generator C (DESS to CISS)

The 3D CycleGAN Generator C demonstrated poor qualitative performance in generating CISS images from DESS inputs. The output image shown in Figure 28 demonstrates how the generator qualitatively progressed over the given epoch, ranging from 0 to 100. The images showed improvement from the first epoch, however, there is visible noise from the model when attempting to incorporate the granularity found in CISS images, specifically for the structure of the bone. The DESS MR images also have increased SI around the articular cartilage, whereas the CISS MR images do not. However, in the generated CISS images, the articular cartilage maintains a high signal that is not adjusted for during the image generation process, which may affect the quantitative results when compared to the ground truth of CISS.

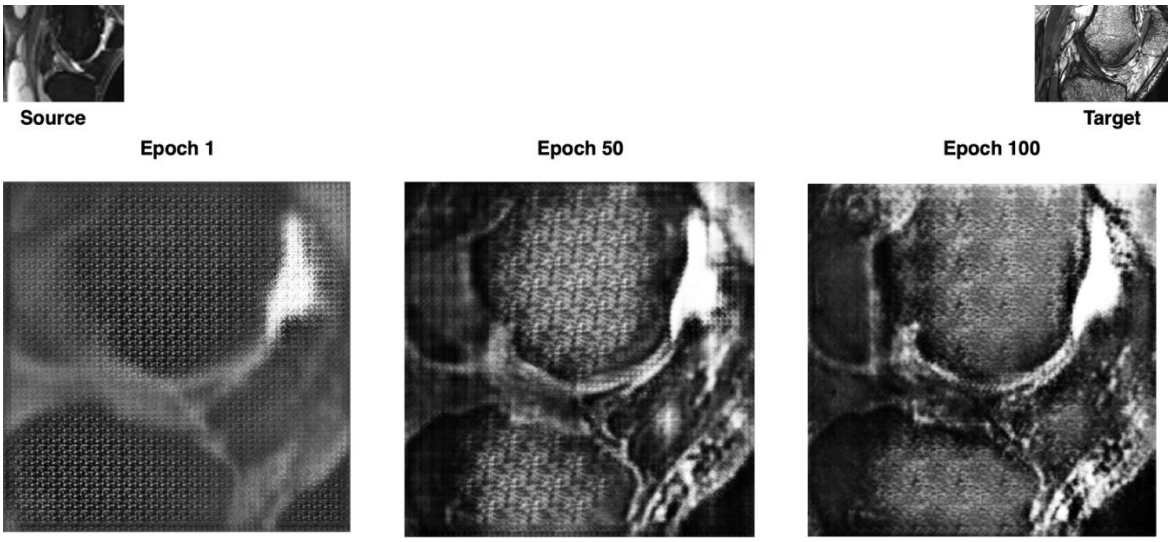

Figure 28. Qualitative performance of Generator C as the source image (upper left) is the DESS image and the target image (upper right) is CISS and the Generator C output images from the first epoch (left) to the last epoch (right)

For Generator C, the MAE was 0.46±0.026 (Figure 27), which is a relatively large error, as an error value three times larger than 0.15 would not be considered an acceptable value.[39] This value indicates that there was a large discrepancy with Generator C, as it had difficulties mapping the correct voxel values from the source DESS images to the target CISS image. The SSIM was calculated at 0.05±0.006, which is very low considering that 0.8 or greater would indicate good structural similarity (Figure 27).[39] The SSIM value of Generator C demonstrates that the generated CISS image bears almost no structural resemblance to the actual ground truth CISS image.[39] This is further verified by the PSNR, which was measured at 10.31±0.512dB, a value far below the threshold of 40dB to be considered a good PSNR (Figure 27).[31,39]

Generator D (CISS to DESS)

Generator D of the 3D CycleGAN demonstrated better performance in generating DESS images from CISS inputs. An output image was shown to demonstrate how the generator

qualitatively progressed over the given epochs, ranging from 0 to 100 (Figure 29). Qualitatively, it appears that fewer adjustments were needed from epoch 50 to epoch 100 to achieve an image that closely resembles the targeted output of a DESS MR image.

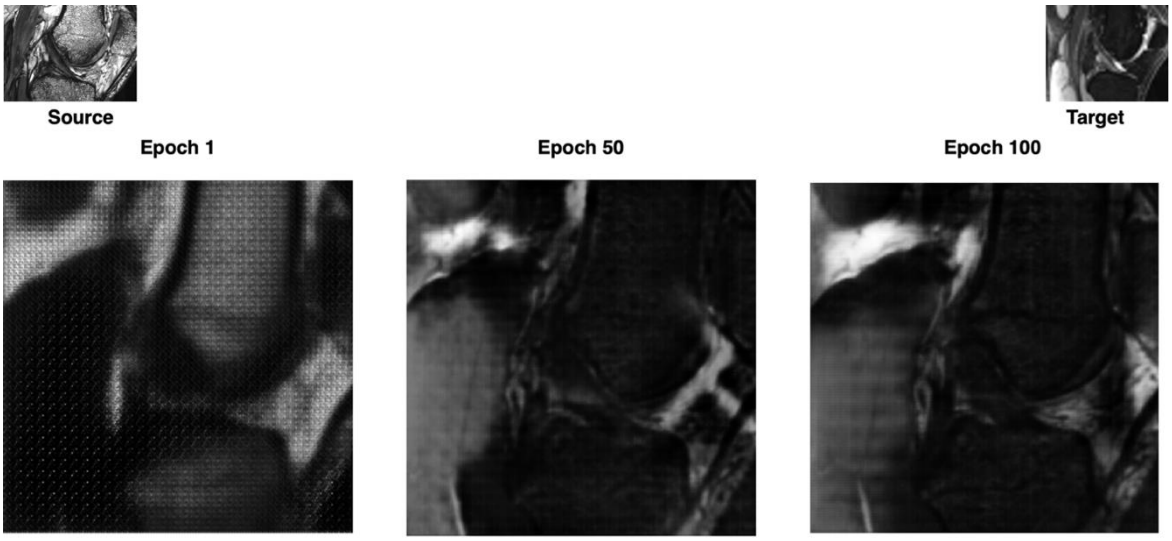

Figure 29. Qualitative performance of Generator D as the source image (upper left) is the CISS image, and the target image (upper right) is DESS, and the Generator D output images from the first epoch (left) to the last epoch (right).

The MAE of Generator D was measured at 0.16±0.016, which represents a relatively low error when compared to that of Generator C, a value that is considered good given that the target error value is 0.15 or below (Figure 27). This result indicates that the generated DESS image voxel intensities were similar to the true DESS image intensities across the image. The SSIM was calculated at 0.38±0.039, while not considered a high value (>0.8), it indicates that the generated image retained a moderate level of the underlying anatomical structure, but with some noise (Figure 27).[39] The PSNR was 18.39±0.725dB (Figure 27), which indicates that the signal is slightly stronger than the random noise generated, as the value is not near the accepted threshold of 40dB and near the value of 15dB, which would be considered poor performance.[31,39]

6.5 Discussion

The purpose of this study was to evaluate whether a 3D CycleGAN could successfully generate MR images from two different MR image sequence inputs to enable consistent evaluation of qMRI SI value across sequences. Contrary to our primary hypothesis, CycleGAN did not successfully generate MR images that could be utilized in a qMRI analysis due to high corruption of noise created during the image generation process. The MAE value was three times higher than the acceptable threshold, while the SSIM and PSNR were both considerably low for Generator C, which indicates that the model was unable to accurately generate image voxel intensities or preserve structural information of the target domain of CISS images. In contrast, the reverse translation of Generator D demonstrated somewhat improved performance, with an error value of 0.16, which is just above the acceptable threshold of 0.15. However, the SSIM and PSNR values did not meet the target of good performance for image generation. The outcome metrics suggest that the model could more effectively generate an image with the DESS signal distribution than the CISS sequence. However, the improvement is not enough to be of value for a qMRI analysis. These findings highlight the challenges of domain adaptation between MRI sequences with substantially different signal compositions and underscore the need for improved data harmonization techniques to improve translation quality.

The poor performance of Generator C may be attributed to the intrinsic signal properties and acquisition design of the CISS sequence. The CISS images had higher spatial definition and emphasized fluid-tissue interfaces, which defined more precise boundaries between joint structures. These characteristics made voxel-level mapping from DESS input challenging, as DESS images provided smooth signal transitions

between voxels. CycleGAN likely struggled to capture the signal variations of CISS imaging using the lower granularity features present in DESS input data. Although Generator D had improved performance, the MAE, SSIM, and PSNR were not acceptable when compared to values considered acceptable in the literature.[39,148,167,188] The outcome metrics indicate that the images generated by Generator D were not comparable to the target image, as noise still corrupted the image, where the structural similarities between the generated image and target image were low.

Previous studies using GAN networks for MRI transformation have reported variable success.[148,167,188] Applications involving translation between T_1 and T_2 weight sequences, or other sequences with comparable signal distribution, have demonstrated high structural similarity.[188] However, no studies have evaluated the transformation between the DESS and CISS sequences, which differ in their sensitivity to fluid-tissue interfaces. In contrast to models trained on large, paired datasets, our unpaired CycleGAN approach relied solely on intensity, which may not fully capture the complexities of CISS images, such as the signal distribution and tissue-specific contrasts.[31,188] By demonstrating the limitations of CycleGAN image synthesis, this study extends the knowledge and application of GAN-based medical imaging translation.

There are several limitations for the present study. The dataset for each domain was relatively small (n=68 DESS; n = 96 CISS), which likely restricted the model's ability to learn the complex mapping between the CISS and DESS domains. A larger, more diverse dataset could improve generalizability. There are also inherent differences between the acquisition parameters of the MR sequences. The voxel size for the DESS images was 0.3mm x 0.3mm x 0.8mm, while for the CISS image, the voxel size was

0.4mm x 0.4mm x 1.5mm. The preprocessing steps, which included cropping and voxel normalization, were steps used to minimize the effects of the different acquisition parameters of the MR sequences. Nonetheless, these differences may have introduced additional difficulties in mapping voxels between the two sequences. The use of convolutional layers also caused the output images to appear grid-like, which could have further caused the quantitative metrics to fall below the acceptable thresholds. In order to address this issue, another model was tested with the convolutional layers removed and replaced with upsampling layers. However, with the removal of the convolutional layers, the processing time increased exponentially. The run time with convolutional layers was approximately 30 minutes per epoch, while with the convolutional layers replaced with upsampling layers, the run time was approximately 3 hours per epoch. The instability of the model also further increased as the model could not converge effectively, which resulted in long run times and increasingly noisy images.

Future studies should ensure MR acquisition parameters are controlled to minimize variability and explore more advanced generative architectures, such as latent diffusion models.[83,116,138] Latent diffusion models operate within a compressed latent space and learn to remove noise and implement the structure and quantitative features of the target sequence.[79,83,138] The diffusion model begins by training and learning how to remove noise and reconstruct the target image.[83] Once the model is trained to reconstruct the target image, it iteratively removes noise from the source image and reconstructs it to the target, generating a new image using the noise-reducing capabilities learned during the training process.[83] Latent diffusion models have demonstrated a superior capability in preserving fine structural detail and capturing complex signal distributions in medical

imaging applications, which may improve the interpretability of the generated MR images.[37,73,116]

Although CycleGAN failed in generating CISS-equivalent images, the findings provided valuable insight into the challenges of cross-sequence translation for qMRI. The unbalanced performance between the two generators highlights the influence of sequence-specific signal properties on model learning and the need for advanced models to capture the complexity of MR images. These results establish an important foundation for future work incorporating larger datasets and advanced generative approaches, such as latent diffusion models. While the CycleGAN model evaluated in this study failed to produce accurate transformations, the development of reliable advanced deep-learning methods could potentially enhance the reproducibility of quantitative imaging studies and enable more consistent evaluation of ACL tissue properties across diverse acquisition protocols.

CHAPTER 7: Discussion

The primary objective of this dissertation was to advance qMRI as a robust, noninvasive tool for assessing the structural and functional integrity of the healing knee joint tissues, specifically the ACL and menisci, following ACL surgery. By shifting from qualitative image interpretation to precise quantitative mapping, this work establishes critical foundational steps toward the use of qMRI-derived metrics as predictive biomarkers in clinical practice.

A pipeline has been previously established to automatically segment the ACL and derive quantitative properties from the MRI, such as CSA and SI.[47,48] However, the long-term objective of this work was to advance the current pipeline to facilitate the clinical translation of qMRI, enabling clinicians to individualize rehabilitation protocols, refine return-to-sport decision making, and ultimately reduce the risk of reinjury and early-onset PTOA. Each chapter addressed a specific aim designed to systematically overcome existing barriers to clinical implementation and to strengthen the scientific and technical framework necessary for qMRI to serve as a reliable clinical tool.

The first and most foundational objective (Specific Aim 1) focused on validating qMRI biomarkers to determine their potential to identify patients at elevated risk of reinjury.[8] Establishing predictive validity is essential for any biomarker intended for clinical decision making. However, translation into clinical workflows introduces technical and methodological challenges that must also be addressed to ensure accuracy, reproducibility, and accessibility. Accordingly, Specific Aim 2 targeted one such critical barrier, the presence of imaging artifacts that may compromise accurate ACL SI measurements.[9] By developing and refining methods to reduce or eliminate these

artifacts, the reliability of qMRI-derived metrics has been improved, strengthening the potential of the method for clinical application.

qMRI has been applied to evaluate ACL graft and tissue integrity following surgery, as demonstrated in Aim 1. However, its application to the menisci has been limited. Given the integral role of the menisci in knee joint biomechanics, extending qMRI analyses to these tissues was essential for the advancement of the pipeline.[4,34,38,52,182,183] Specific Aim 3 translated and adapted qMRI biomarkers to robustly characterize meniscal tissue changes following ACL injury and surgery.[10,11] This expansion enhances understanding of the joint-wide tissue adaptations and advances qMRI toward a comprehensive assessment tool capable of evaluating multiple tissue structures affected by ACL injury and subsequent surgery. Additionally, an important consideration when developing clinically translatable qMRI is determining which MRI sequences these tools will be compatible with. While the CISS sequence enabled the advancements presented in this dissertation for both ACL and meniscal evaluation, broader clinical adoption would require advancing qMRI across various imaging sequences. The potential of using alternative sequences, such as DESS, would substantially increase the clinical applicability of the methodologies developed in this work (Aim 4).

Chapter 1 provided the scientific background and significance of this research, outlining the theoretical framework, purpose, and hypotheses associated with each specific aim. Collectively, the work presented in this dissertation advances qMRI from a research-based imaging approach toward a clinically useful, multi-tissue assessment with the potential to improve patient-specific care following ACL surgery.[35]

7.1 Specific Aim 1

Identify qMRI variables that predict patients at a higher risk of re-tearing their ACL after ACL Restoration surgery.

The goal of this study (Chapter 2) was to determine whether early qMRI variables obtained 6 to 9 months following ACL restoration surgery were associated with the risk of revision surgery within two years.[8] Using prospectively collected data from the BEAR clinical trials,[118-120] we evaluated whether the structural and compositional imaging variables of CSA, SI, and qMRI-predicted failure load demonstrated predictive ability for reinjury risk beyond clinical and functional outcome measures assessed at the same postoperative timepoint.

We hypothesized that qMRI variables obtained at 6 to 9 months postoperatively would be significantly associated with the odds ratio of revision ACL surgery within two years. Additionally, we hypothesized that these imaging-based biomarkers would demonstrate stronger predictive ability than commonly used clinical and functional assessments performed during return-to-sport evaluation.

The 6 to 9 month follow-up period represents a clinically meaningful time point as it coincides with the stage at which patients are typically evaluated for return to sport participation.[8] Decisions at this stage are mainly based on functional testing, strength assessments, and patient-reported outcomes, yet there is an absence of objective noninvasive measures of ligament structural integrity.[8] Therefore, identifying imaging biomarkers capable of predicting reinjury risk at this time has direct translational

relevance, as it may inform clinical decision-making regarding safe return to sport during a critical phase of rehabilitation.

We found that early qMRI variables were significantly associated with the risk of revision ACL surgery within two years.[8] Specifically, measures reflecting ligament size and tissue composition demonstrated predictive ability for reinjury risk, whereas traditional clinical and functional outcome measures showed limited association. Furthermore, when structural (CSA) and compositional (SI) variables were combined to derive a qMRI-predicted failure load, the predictive performance improved relative to individual parameters alone.

The association between CSA and revision risk likely reflects the importance of tissue remodeling during the healing process. A larger CSA may indicate more robust tissue incorporation and structural adaptation to mechanical loading.[13,16,80,121] Similarly, SI serves as a marker of tissue composition and organization, as variations in SI reflect differences in water content, collagen organization, and remodeling.[63,80,121] Lower SI values correspond to a more organized collagen structure, whereas persistently elevated SI may indicate incomplete remodeling.[14,63,80,121] At the 6 to 9 month return-to-sport timepoint, a low SI value may indicate readiness based on qMRI-predicted failure load. However, if driven by metallic artifacts, this could lead to a premature return to sport and increased risk of reinjury.[8,16] The derived qMRI-predicted failure load integrates both the structural size and compositional characteristics, providing a biomechanically meaningful estimate of ligament strength.

Specific Aim 1 presents work that extends beyond the current body of research that has demonstrated relationships between MRI-derived variables and structural

properties of the healing ligament by translating these findings to a clinical population and demonstrating that noninvasive qMRI metrics can predict revision surgery.[13-16] Therefore, the early qMRI metrics obtained at the time of return-to-sport evaluation were associated with the risk of revision ACL surgery within two years following ACL restoration.

Structural and compositional imaging parameters, particularly when combined into the qMRI-predicted failure load, demonstrated greater predictive utility than traditional clinical assessments alone. These findings provided an essential step toward establishing qMRI as a noninvasive assessment tool of ligament integrity. However, a limitation of the use of SI as a predictive tool is the possibility of metallic artifacts affecting the measurement of the SI value of the ACL. As mentioned previously, a higher SI corresponds to differences in collagen organization, even indicating incomplete remodeling of the tissue, while a lower SI corresponds to a more organized collagen structure of the tissue. If the tissue is measured at a lower value due to the artifacts found in the MR image, the predictive ability of the qMRI-predicted failure load would not accurately represent the patient's tissue. Therefore, in Specific Aim 2 (Chapter 3), metallic artifacts were detected, isolated, and removed automatically to ensure the accuracy of the SI measurement of the ACL.

7.2 Specific Aim 2

Advancement of an automatic segmentation pipeline for metallic artifact removal in post-surgical ACL MRI

The objective of this work (Chapter 3) was to advance the accuracy of an automated segmentation pipeline for identifying ACL tissue in postoperative MR images while minimizing the influence of metallic artifacts.[9] Postoperative MR image evaluation of the ACL can be distorted by metallic artifacts resulting from micro-debris from the tools used to drill osseous tunnels for surgical fixation of the ACL or graft.[9,65] These artifacts can obscure tissue boundaries, distort signal characteristics of the ACL, and introduce variability in both manual and automatic segmentation.[47-49] Accurate segmentation of the ACL is critical for the measurement of qMRI predicted failure load. Therefore, improving segmentation accuracy, specifically in artifact-prone regions, is an important step toward the broader implementation of qMRI-metrics being used in clinical settings. We hypothesized that the signal intensity obtained from the automatic segmentation pipeline with artifact removed would not be significantly different from the ground truth (manual segmentation) and statistically equivalent within a 5% margin of error.

The work presented in Chapter 3 demonstrates how K-means clustering can refine an automatic segmentation algorithm to remove the lost signal intensity values induced by the metallic artifacts in the image so that the SI data are not skewed. MRI data were obtained from 82 patients enrolled in three prospective BEAR clinical trials of ACL surgery.[118,119] The results demonstrate that the Dice coefficient, precision, and sensitivity were comparable to the ground truth, which was the manual segmentation of the ACL and artifact for this work. The artifact-removing approach allowed for more reliable identification of the ACL boundaries despite the presence of metallic distortion along the tissue. The automatic capability of this segmentation pipeline to identify and remove artifacts also allowed for the segmentations of ACLs with artifacts to be reduced from

about an hour of manual segmentation of the ligament to about 30 seconds. The time-saving aspect also contributes to the adaptation of qMRI-metrics in clinical settings.

Previous studies have explored the use of machine learning and deep learning approaches to address metal artifact reduction in postoperative MRI.[1,45,94] These methods often employ neural network architectures that must be trained on large image datasets to learn the complex signal distortions caused by metallic implants or other artifacts observed in MRIs. These approaches typically require thousands of labeled training images or paired datasets consisting of artifact MRIs and artifact-free MRIs. The development of such datasets can be challenging, particularly in orthopaedic applications, where the ground-truth of artifact-free images is not available. By leveraging the distinct signal properties associated with metallic artifacts, this method was able to reduce the variability of SI due to artifacts without the need for extensive training datasets or computationally intensive models. As a result, the proposed pipeline provides a solution that can be easily applied to the current automatic segmentation method without requiring retraining.

The automated segmentation pipeline developed in this study improved the accuracy and robustness of ACL tissue identification, and accurate measurements of ACL SI in postoperative MR images affected by metallic artifacts. Improving the reliability of qMRI-metrics, such as SI, further strengthens the foundation necessary for clinical implementation of qMRI-based biomarkers. Altogether with the qMRI-predicted failure load ability to identify patients at a higher risk of reinjury described in Aim 1, these findings continue to advance the overall goal of this dissertation to establish qMRI as a clinically accessible tool for analyzing ligament healing and predicting reinjury risk

following ACL surgery. However, ACL injuries rarely occur in isolation. Meniscal injuries are frequently present at the same time of ACL rupture and play an important role in long-term knee health.[59,114] Evaluating meniscal morphology during postoperative recovery may provide additional insight into joint health beyond the status of the ACL alone, which is further explored in Specific Aim 3.

7.3 Specific Aim 3

Evaluate the influence of ACL surgery on the morphological integrity of the meniscus as measured by qMRI.

Specific Aim 3 was addressed in Chapters 4 and 5. The objectives of these studies were evaluated in two sub-aims: 1) to identify significant CSA and SI differences of the menisci due to sex and anatomical variations; and 2) to evaluate the influence of ACL surgery on the morphological integrity of the menisci using qMRI. Understanding how the menisci's structure and composition change following ACL surgery may provide important insight into the long-term health of the knee joint. To assess meniscal integrity post-surgery, qMRI variables, specifically CSA and SI, were analyzed as these measures have shown predictive value in assessing the structural and compositional integrity of healing ligaments, as demonstrated in Chapter 2.[8]

To better establish a reference for interpreting postoperative changes in meniscal morphology, an initial analysis was performed to characterize baseline CSA and SI values in intact menisci and to evaluate potential anatomical differences between sexes using our qMRI approach (Chapter 4).[11,104,182,192] CSA and SI profiles of the contralateral intact limb were compared between male and female subjects of the BEAR clinical trials.

We hypothesized that the CSA of the menisci in males would be significantly larger than in females, even when normalized for knee size, reflecting known sex-related differences in joint morphology.[11] However, we expected SI profiles to be similar between sexes, as intact menisci exhibited comparable tissue composition,[11,52,195] which was found to be true in our study. However, once the CSA was normalized by knee size, only the anterior region of the medial meniscus was found to be smaller in females than in males. Previous studies have shown that geometric changes of the medial meniscus had an effect on the contact variables of the lateral meniscus.[40] The study showed that increasing the cross-sectional height of the medial meniscus by 1 standard deviation decreased the maximum pressure by 32% and mean pressure by 24%.[40] Therefore, although the significant change in CSA between the sexes was only found in the medial meniscus, studies have shown that this change could have significant impact on the surrounding tissues.[4,59,86,183]

Following the baseline characterization between the sexes (Chapter 4), the CSA and SI profiles of the menisci were compared between each patient's surgical and contralateral limb across the 6-, 12-, and 24-month postoperative timepoints (Chapter 5).[10] This longitudinal comparison allowed for the ability to identify potential morphological changes in the menisci following ACL surgery. We hypothesized that the CSA and SI of both the medial and lateral menisci in the surgical knees would be higher than those of the contralateral knees, potentially reflecting morphological changes associated with structural and compositional changes of the tissue following ACL injury and subsequent surgery. Additionally, we hypothesized that the CSA and SI values measured at 24-months would be closer to the values of the contralateral limb menisci, which may indicate that the morphological and compositional differences due to surgery

had returned to those of the patient's contralateral knee, which were considered to be baseline.

The results of this work demonstrated that qMRI-derived measurements of meniscal CSA and SI provide valuable insight into meniscal morphology following ACL surgery. The characterization of male and female differences allowed for an accurate interpretation of postoperative changes, particularly when considering the CSA changes of the menisci after ACL surgery. The differences observed between surgical and contralateral knees suggest that ACL injury and surgery influence the structural and compositional characteristics. The CSA changes suggest that there is swelling of the menisci during postoperative recovery over the 24-month healing period. These findings also highlight the importance of evaluating specific regions of the menisci. Current methods typically rely on averaging values across the entire meniscus, which may obscure meaningful changes in localized areas.[52,192] Evaluating discrete locations along the meniscal arc length is particularly important because characterizing meniscal morphology and compositional changes through qMRI may provide additional markers of joint adaptation processes that are not captured through ACL-focused assessments alone.

This work not only expands the application of qMRI beyond ligament evaluation but has presented a novel method on evaluating regional meniscal changes of CSA and SI across patient-specific groups longitudinally. Previous studies evaluating postoperative meniscal health using MRI have relied on dividing the meniscus into three broad anatomical regions and averaging across these regions, as well as evaluating SI on a single representative MRI slice.[86,114,192] While these approaches have provided important

insights into meniscal tissue changes, they do not fully capture the spatial changes of meniscal morphology. This study demonstrates how the broader joint environment responds to ACL injury, further demonstrating that ACL injury is a whole-joint injury.

The meniscal qMRI-derived metrics may be valuable for identifying patients at risk for reinjury or future joint degeneration, which would be beneficial for guiding patient-specific rehabilitation strategies aimed at protecting meniscal health. For example, if a patient presents at 6-months post-surgery with a smaller anterior medial CSA and elevated SI in both the medial and lateral menisci relative to their contralateral, these findings would indicate present and possibly persistent structural and compositional abnormalities. This finding might suggest delaying return to sport and modifying rehabilitation to reduce the risk of reinjury and progression of early onset PTOA. Together with the findings from Aims 1 and 2, this work further supports and advances the potential of qMRI as a comprehensive and noninvasive tool for evaluating knee joint health and improving clinical decision-making following ACL surgery. The final aim of this dissertation focused on optimizing a deep learning algorithm capable of transforming MR images across sequences to improve the accessibility of imaging data used for qMRI analysis.

7.4 Specific Aim 4

Optimize a deep learning algorithm to transform MR images across sequences.

Specific Aim 4 was addressed in Chapter 6. Chapters 2 through 5 highlighted the value of qMRI-derived metrics for characterizing the healing and morphological changes of tissues in the knee following ACL surgery. However, the analyses presented in these

chapters relied exclusively on images acquired using the CISS sequence on a Siemens 3T MRI system. While the CISS sequence provides high spatial resolution and excellent contrast for visualizing fine anatomical structures such as ligaments and menisci, it is not as commonly acquired in routine clinical musculoskeletal imaging protocols. The DESS sequence is more widely used in clinical studies and practice as it enhances contrast to the articular cartilage structure and composition. As a result, the qMRI-based predictive models developed in this dissertation have not been evaluated using MRI sequences that are more routinely obtained in clinical settings. Therefore, the objective of this aim was to investigate whether a deep learning image transformation framework could translate images acquired with the DESS sequence into the CISS domain. We began by trying various methods that may have achieved this task, such as ratio mean intensities, histogram matching, and adjusting the current CycleGAN method proposed. These methods are further explored in Appendix B. However, none of these methods proved to be as successful as the CycleGAN presented in Chapter 6. Therefore, we hypothesized that a CycleGAN architecture would be able to learn the mapping between the source domain (DESS) and the target domain (CISS), allowing synthetic CISS-like images to be generated from DESS inputs. We determined that CycleGAN was not an effective approach.

Generative adversarial networks such as CycleGAN have been previously explored in medical imaging tasks for image synthesis and domain translation.[116,188] These models are typically selected because of their ability to allow image-to-image translation without requiring perfectly paired training data.[31,188,197] However, the CycleGAN architecture implemented in this study did not reliably generate CISS-like

images from DESS inputs that preserved the structure necessary for the quantitative analysis. These findings highlight an important challenge associated with cross-sequence MRI translation. The technical and hardware differences add more complexities and variabilities when attempting to find mapping patterns between the sequences to allow for an accurate transformation. CISS imaging emphasizes a high signal-to-noise ratio and strong contrast between fluid and surrounding soft tissues, making it well-suited for visualizing complex anatomical boundaries.[18,43,58,95] In contrast, DESS images provide SI mapping across the cartilage that is particularly valuable for evaluating morphological changes that can be related to OA.[42,43,84,158,170] Previous work has shown that signal-to-noise ratio is significantly lower in DESS images than in CISS images, as well as the contrast-to-noise ratio, which resulted in CISS images having better performance in identifying anatomically complex microstructures.[43] Because these sequences capture different aspects of tissue signal behavior, accurately transforming one sequence into another while preserving the quantitative information will require more sophisticated modeling approaches than those offered by traditional GAN-based architectures.

The CycleGAN approach did not achieve the desired transformation performance in this study, as the generated images failed to meet the quantitative thresholds for similarity to the ground truth. This failure was largely driven by image noise, which reduced both the quantitative and qualitative agreement with the ground truth. Nonetheless, the process of implementing and evaluating this model provided important insight into the challenges of cross-sequence MRI translation. In particular, this study highlighted the sensitivity of quantitative imaging analyses to the differences in signal characteristics and spatial detail of various MRI sequences. These observations show that

visual similarity alone is not sufficient when synthetic images are intended for quantitative measurements, as even minor changes in tissue signal may influence the qMRI biomarkers.

This aim explored the ability of using deep learning-based image translation to bridge the differences between various MRI imaging protocols used in research and those used in the clinic. While CycleGAN did not produce the desired CISS-like images, the findings provide valuable insight and highlight important considerations for future model development. Particularly, this work highlighted the challenges associated with translating between MRI sequences with fundamentally different signal characteristics, the impact of noise on generative model performance, and the need for alternative architectures that better preserve quantitative and structural features crucial for qMRI analyses. Continued advances in deep learning may ultimately enable more flexible use of qMRI across diverse imaging protocols, further supporting the goal of this dissertation to expand the accessibility and clinical use of qMRI for evaluating knee joint health following ACL injury. In the meantime, the qMRI pipeline for these applications requires the CISS sequence to be used.[49]

7.5 Future Directions

Collectively, the studies presented in this dissertation provide important steps toward advancing qMRI as a clinical tool for evaluating ligament healing. However, several opportunities remain for future investigation. Future research should focus on validating the predictive findings of qMRI in larger, multi-center cohort studies. Longitudinal modeling of healing trajectories may further improve predictive accuracy. Additionally, integration of these qMRI biomarkers with biomechanical outcomes, functional tests, and

potentially the use of machine learning-based predictive modeling could advance clinically deployable decision-making tools.

Performance evaluation of the automated segmentation pipeline across imaging datasets acquired from multiple institutions, scanners, and imaging protocols should also be considered for future work. Metallic artifact characteristics can vary depending on size, metallic composition of the artifacts, MRI acquisitions parameters, and scanner manufacturer. Validating the pipeline in diverse clinical environments will be essential to ensure the generalizability of the artifact removal feature of the automatic segmentation tool. Similarly, future work should be directed at improving sequence-to-sequence transformations. MR acquisition is dependent on scanners and sequence selection,[49] therefore, sequence would also ensure qMRI pipeline accessibility in the clinical setting. While the CycleGAN approach was not successful, other machine learning algorithms, such as latent diffusion modeling, may be successful.[73,83,116,138] As discussed in Chapter 6, more advanced deep learning models need to be evaluated for transforming MRI sequences for ACL qMRI assessments. These future research directions could further refine the pipeline and framework developed in this dissertation and expand the application of qMRI toward a comprehensive tool for knee joint health assessment.

7.6 Conclusion

ACL injuries remain a significant challenge in orthopaedic medicine due to the high risk of reinjury and the long-term consequences for joint health following surgical restoration. Current clinical assessments used to guide rehabilitation and return-to-sport decisions rely primarily on functional performance measures and patient-reported outcomes, which do not directly evaluate the structural integrity of the healing tissues. The goal of this

dissertation was to advance the use of qMRI as a noninvasive and clinically accessible tool for assessing ligament healing and overall knee joint health following ACL surgery. This work has shown that early qMRI measures of ligament morphology and composition were predictive of identifying patients at increased risk of reinjury. Advances were also developed to enhance the reliability of qMRI analysis through an automated segmentation pipeline capable of reducing metallic artifact influence and a deep learning framework designed to transform images across MRI sequences. The automated segmentation pipeline was also expanded by characterizing longitudinal morphological changes in the menisci following ACL surgery. Collectively, these findings contribute to the growing body of research supporting qMRI as a tool for evaluating tissue integrity and provide foundational steps toward integrating qMRI biomarkers into clinical decision-making to improve patient outcomes following ACL injury and surgery.

References

1. Ahmad A, Parker D, Dheer S, Samani ZR, Verma R. 3D-QCNet–A pipeline for automated artifact detection in diffusion MRI images. *Computerized Medical Imaging and Graphics.* 2023;103:102151.
2. Ahmed A, Burke D. In-vitro of measurement of static pressure distribution in synovial joints—Part I: Tibial surface of the knee. 1983.
3. Al-Dadah O, Shepstone L, Donell ST. Clinical outcome measures in anterior cruciate ligament reconstruction: Clinician vs patient completed knee scores. *The Surgeon.* 2021;19(6):e353-e360.
4. Allen CR, Wong EK, Livesay GA, et al. Importance of the medial meniscus in the anterior cruciate ligament-deficient knee. *Journal of Orthopaedic Research.* 2000;18(1):109-115.
5. Anderson MJ, Browning III WM, Urband CE, Kluczynski MA, Bisson LJ. A systematic summary of systematic reviews on the topic of the anterior cruciate ligament. *Orthopaedic journal of sports medicine.* 2016;4(3):2325967116634074.
6. Ardern CL, Taylor NF, Feller JA, Webster KE. Return-to-sport outcomes at 2 to 7 years after anterior cruciate ligament reconstruction surgery. *The American journal of sports medicine.* 2012;40(1):41-48.
7. Bae J-H, Hosseini A, Wang Y, et al. Articular cartilage of the knee 3 years after ACL reconstruction: A quantitative T2 relaxometry analysis of 10 knees. *Acta orthopaedica.* 2015;86(5):605-610.
8. Barnes DA, Badger GJ, Yen Y-M, et al. Quantitative MRI Biomarkers to Predict Risk of Reinjury Within 2 Years After Bridge-Enhanced ACL Restoration. *The American Journal of Sports Medicine.* 2023:03635465221142323.

9. Barnes DA, Murray CJ, Molino J, et al. Advancement of an automatic segmentation pipeline for metallic artifact removal in post-surgical ACL MRI. *Magnetic Resonance Imaging.* 2025:110417.

10. Barnes DA, Murray CJ, Movahhedi M, et al. Longitudinal Quantitative Mapping Reveals Persistent Meniscal Morphological and Signal Intensity Differences After ACL Surgery *The American Journal of Sports Medicine.* 2026:In Review.

11. Barnes DA, Murray CJ, Movahhedi M, et al. Quantitative Mapping of Meniscus Morphology Using Advanced Imaging Analysis in Young Patients *Scientific Reports.* 2026.

12. Barnett SC, Murray MM, Badger GJ, et al. Earlier resolution of symptoms and return of function after bridge-enhanced anterior cruciate ligament repair as compared with anterior cruciate ligament reconstruction. *Orthop J Sports Med.* 2021;9(11):23259671211052530.

13. Beveridge JE, Machan JT, Walsh EG, et al. Magnetic resonance measurements of tissue quantity and quality using T2 * relaxometry predict temporal changes in the biomechanical properties of the healing ACL. *J Orthop Res.* 2018;36(6):1701-1709.

14. Biercevicz AM, Akelman MR, Fadale PD, et al. MRI volume and signal intensity of ACL graft predict clinical, functional, and patient-oriented outcome measures after ACL reconstruction. *Am J Sports Med.* 2015;43(3):693-699.

15. Biercevicz AM, Miranda DL, Machan JT, Murray MM, Fleming BC. In situ, noninvasive, T2*-weighted MRI-derived parameters predict ex vivo structural properties of an anterior cruciate ligament reconstruction or bioenhanced primary

repair in a porcine model. *The American Journal of Sports Medicine.* 2013;41(3):560-566.

16. Biercevicz AM, Murray MM, Walsh EG, et al. T2* MR relaxometry and ligament volume are associated with the structural properties of the healing ACL. *Journal of Orthopaedic Research.* 2014;32(4):492-499.

17. Bradley PX, Kim-Wang SY, Blaisdell BS, et al. Tibiofemoral cartilage strain and recovery following a 3-mile run measured using deep learning segmentation of bone and cartilage. *Osteoarthritis and Cartilage Open.* 2025;7(1):100556.

18. Cavallaro M, Coglitore A, Tessitore A, et al. Three-dimensional constructive interference in steady state (3D CISS) imaging and clinical applications in brain pathology. *Biomedicines.* 2022;10(11):2997.

19. Cavanaugh JT, Powers M. ACL rehabilitation progression: where are we now? *Current reviews in musculoskeletal medicine.* 2017;10(3):289-296.

20. Cerulli G, Placella G, Sebastiani E, et al. ACL reconstruction: choosing the graft. *Joints.* 2013;1(1):18.

21. Chervyakov N, Lyakhov P, Nagornov N. Analysis of the quantization noise in discrete wavelet transform filters for 3D medical imaging. *Applied Sciences.* 2020;10(4):1223.

22. Chhadia AM, Inacio MC, Maletis GB, et al. Are meniscus and cartilage injuries related to time to anterior cruciate ligament reconstruction? *The American journal of sports medicine.* 2011;39(9):1894-1899.

23. Christensen JJ, Krych AJ, Engasser WM, et al. Lateral tibial posterior slope is increased in patients with early graft failure after anterior cruciate ligament reconstruction. *Am J Sports Med.* 2015;43(10):2510-2514.

24. Christino MA, Fleming BC, Machan JT, Shalvoy RM. Psychological factors associated with anterior cruciate ligament reconstruction recovery. *Orthopaedic journal of sports medicine.* 2016;4(3):2325967116638341.

25. Chu CR, Williams AA. Quantitative MRI UTE-T2* and T2* show progressive and continued graft maturation over 2 years in human patients after anterior cruciate ligament reconstruction. *Orthopaedic journal of sports medicine.* 2019;7(8):2325967119863056.

26. Chu CR, Williams AA, West RV, et al. Quantitative magnetic resonance imaging UTE-T2* mapping of cartilage and meniscus healing after anatomic anterior cruciate ligament reconstruction. *The American journal of sports medicine.* 2014;42(8):1847-1856.

27. Church S, Keating J. Reconstruction of the anterior cruciate ligament: timing of surgery and the incidence of meniscal tears and degenerative change. *The Journal of Bone & Joint Surgery British Volume.* 2005;87(12):1639-1642.

28. Cinque ME, Dornan GJ, Chahla J, Moatshe G, LaPrade RF. High rates of osteoarthritis develop after anterior cruciate ligament surgery: an analysis of 4108 patients. *The American journal of sports medicine.* 2018;46(8):2011-2019.

29. Coleman GB, Andrews HC. Image segmentation by clustering. *Proceedings of the IEEE.* 1979;67(5):773-785.

30. Cristiani R, Mikkelsen C, Forssblad M, Engström B, Stålman A. Only one patient out of five achieves symmetrical knee function 6 months after primary anterior cruciate ligament reconstruction. *Knee Surgery, Sports Traumatology, Arthroscopy.* 2019;27(11):3461-3470.

31. Czobit C, Samavi R. Cyclegan models for MRI image translation. *arXiv preprint arXiv:240100023.* 2023.

32. Dalmiya S, Dasgupta A, Datta SK. Application of wavelet based K-means algorithm in mammogram segmentation. *International Journal of Computer Applications.* 2012;52(15).

33. Daniel DM, Stone ML, Sachs R, Malcom LL. Instrumented measurement of anterior knee laxity in patients with acute anterior cruciate ligament disruption. *Am J Sports Med.* 1985;13(6):401-407.

34. Danso EK, Oinas JM, Saarakkala S, et al. Structure-function relationships of human meniscus. *Journal of the mechanical behavior of biomedical materials.* 2017;67:51-60.

35. DeFroda SF, RM OD, Fadale PD, Owens BD, Fleming BC. The role of magnetic resonance imaging in evaluating post-operative ACL reconstruction healing and graft mechanical properties: A new criterion for return to play? *Phys Sportsmed.* 2021;49(2):123-129.

36. Dhanachandra N, Manglem K, Chanu YJ. Image segmentation using K-means clustering algorithm and subtractive clustering algorithm. *Procedia Computer Science.* 2015;54:764-771.

37. Dhariwal P, Nichol A. Diffusion models beat gans on image synthesis. *Advances in neural information processing systems.* 2021;34:8780-8794.

38. Di Paolo S, Grassi A, Lucidi GA, et al. Biomechanics of the lateral meniscus: evidences from narrative review. *Annals of Joint.* 2022;7:19.

39. Dohmen M, Klemens MA, Baltruschat IM, Truong T, Lenga M. Similarity and quality metrics for MR image-to-image translation. *Scientific Reports.* 2025;15(1):3853.

40. Donahue TLH, Hull M, Rashid MM, Jacobs CR. The sensitivity of tibiofemoral contact pressure to the size and shape of the lateral and medial menisci. *Journal of Orthopaedic Research.* 2004;22(4):807-814.

41. Du X, Cozzi FM, Jena R. Revolutionizing Brain Tumor Imaging: Generating Synthetic 3D FA Maps from T1-Weighted MRI using CycleGAN Models. *arXiv preprint arXiv:250503662.* 2025.

42. Eckstein F, Hudelmaier M, Wirth W, et al. Double echo steady state magnetic resonance imaging of knee articular cartilage at 3 Tesla: a pilot study for the Osteoarthritis Initiative. *Annals of the rheumatic diseases.* 2006;65(4):433-441.

43. Fan X, Ding C, Zhao G, Hou Y. Comparing the Double-Echo Steady-State with Water Excitation and Constructive Interference in Steady-State Sequence Techniques for Identifying Extracranial Facial Nerve and Tumor Positions in Patients with Parotid Tumors. *American Journal of Neuroradiology.* 2024;45(9):1355-1362.

44. Feroe AG, Clark SC, Hevesi M, et al. Management of Meniscus pathology with concomitant anterior cruciate ligament injury. *Current Reviews in Musculoskeletal Medicine.* 2024;17(8):321-334.

45. Feuerriegel GC, Sutter R. Managing hardware-related metal artifacts in MRI: current and evolving techniques. *Skeletal Radiology.* 2024;53(9):1737-1750.

46. Fithian DC, Kelly MA, Mow VC. Material properties and structure-function relationships in the menisci. *Clinical Orthopaedics and Related Research (1976-2007).* 1990;252:19-31.

47. Flannery SW, Kiapour AM, Edgar DJ, et al. A transfer learning approach for automatic segmentation of the surgically treated anterior cruciate ligament. *Journal of Orthopaedic Research®.* 2022;40(1):277-284.

48. Flannery SW, Kiapour AM, Edgar DJ, Murray MM, Fleming BC. Automated magnetic resonance image segmentation of the anterior cruciate ligament. *Journal of Orthopaedic Research®.* 2021;39(4):831-840.

49. Flannery SW, Walsh EG, Sanborn RM, et al. Reproducibility and postacquisition correction methods for quantitative magnetic resonance imaging of the anterior cruciate ligament (ACL). *Journal of Orthopaedic Research®.* 2022;40(12):2908-2913.

50. Fleming BC, Baranker B, Badger GJ, et al. Bridge-enhanced anterior cruciate ligament restoration: 6-year results from the first-in-human cohort study. *Orthopaedic Journal of Sports Medicine.* 2024;12(8):23259671241260632.

51. Fox AJ, Bedi A, Rodeo SA. The basic science of human knee menisci: structure, composition, and function. *Sports health.* 2012;4(4):340-351.

52. Fox AJ, Wanivenhaus F, Burge AJ, Warren RF, Rodeo SA. The human meniscus: a review of anatomy, function, injury, and advances in treatment. *Clinical anatomy.* 2015;28(2):269-287.

53. Friel NA, Chu CR. The Role of ACL Injury in the Development of Posttraumatic Knee Osteoarthritis. *Clinics in Sports Medicine.* 2013;32(1):1-12.

54. Fu FH, Bennett CH, Ma CB, Menetrey J, Lattermann C. Current trends in anterior cruciate ligament reconstruction: Part II. Operative procedures and clinical correlations. *The American journal of sports medicine.* 2000;28(1):124-130.

55. Gao KT, Xie E, Chen V, et al. Large-Scale Analysis of Meniscus Morphology as Risk Factor for Knee Osteoarthritis. *Arthritis & Rheumatology.* 2023;75(11):1958-1968.

56. Gebre RK, Senjem ML, Raghavan S, et al. Cross–scanner harmonization methods for structural MRI may need further work: A comparison study. *NeuroImage.* 2023;269:119912.

57. Geeslin AG, Moatshe G, Chahla J, et al. Anterolateral knee extra-articular stabilizers: a robotic study comparing anterolateral ligament reconstruction and modified Lemaire lateral extra-articular tenodesis. *The American journal of sports medicine.* 2018;46(3):607-616.

58. Gonçalves FG, do Amaral LLF. Constructive interference in steady state imaging in the central nervous system. *European Neurological Review.* 2011;6(2):138.

59. Grassi A, Dal Fabbro G, Di Paolo S, et al. Medial and lateral meniscus have a different role in kinematics of the ACL-deficient knee: a systematic review. *Journal of ISAKOS.* 2019;4(5):233-241.

60. Graves MJ. 3 T: the good, the bad and the ugly. *The British Journal of Radiology.* 2022;95(1130):20210708.

61. Group MK, Spindler KP, Huston LJ, et al. Ten-year outcomes and risk factors after anterior cruciate ligament reconstruction: a MOON longitudinal prospective cohort study. *The American journal of sports medicine.* 2018;46(4):815-825.

62. Gupta RK, Aggarwal S, Aggarwal V, Garg SK, Kumar S. Preserved insertions of the semitendinosus and gracilis tendons (STG) in ACL reconstruction: a new surgical technique with preliminary results. *Current Orthopaedic Practice.* 2010;21(4):409-414.

63. Hajek PC, Gylys-Morin VM, Baker LL, et al. The high signal intensity meniscus of the knee magnetic resonance evaluation and in vivo correlation. *Investigative radiology.* 1987;22(11):883-890.

64. Hardy PA, Recht MP, Piraino D, Thomasson D. Optimization of a dual echo in the steady state (DESS) free-precession sequence for imaging cartilage. *Journal of Magnetic Resonance Imaging.* 1996;6(2):329-335.

65. Hargreaves BA, Worters PW, Pauly KB, et al. Metal-induced artifacts in MRI. *American Journal of Roentgenology.* 2011;197(3):547-555.

66. Harris JD, Abrams GD, Bach BR, et al. Return to sport after ACL reconstruction. *Orthopedics.* 2014;37(2):e103-e108.

67. Hartigan JA. *Clustering algorithms.* John Wiley & Sons, Inc.; 1975.

68. Hazleman B, Riley G, Speed C. *Soft tissue rheumatology.* Oxford University Press; 2004.

69. Hewett TE, Di Stasi SL, Myer GD. Current Concepts for Injury Prevention in Athletes After Anterior Cruciate Ligament Reconstruction. *The American Journal of Sports Medicine.* 2013;41(1):216-224.

70. Höher J, Bach T, Münster A, Bouillon B, Tiling T. Does the mode of data collection change results in a subjective knee score? Self-administration versus interview. *The American journal of sports medicine.* 1997;25(5):642-647.

71. Huang Z, Cui J, Zhong M, et al. Risk factors of cartilage lesion after anterior cruciate ligament reconstruction. *Frontiers in Cell and Developmental Biology.* 2022;10:935795.

72. Irrgang JJ, Ho H, Harner CD, Fu FH. Use of the International Knee Documentation Committee guidelines to assess outcome following anterior cruciate ligament reconstruction. *Knee Surgery, Sports Traumatology, Arthroscopy.* 1998;6:107-114.

73. Jiang L, Mao Y, Wang X, Chen X, Li C. Cola-diff: Conditional latent diffusion model for multi-modal mri synthesis. *International Conference on Medical Image Computing and Computer-Assisted Intervention.* 2023:398-408.

74. Johnson J, Alahi A, Fei-Fei L. Perceptual losses for real-time style transfer and super-resolution. *European conference on computer vision.* 2016:694-711.

75. Jungmann PM, Agten CA, Pfirrmann CW, Sutter R. Advances in MRI around metal. *Journal of Magnetic Resonance Imaging.* 2017;46(4):972-991.

76. Kaeding CC, Pedroza AD, Reinke EK, et al. Risk Factors and Predictors of Subsequent ACL Injury in Either Knee After ACL Reconstruction. *The American Journal of Sports Medicine.* 2015;43(7):1583-1590.

77. Kan A, Oshida M, Oshida S, et al. Anatomical significance of a posterior horn of medial meniscus: the relationship between its radial tear and cartilage degradation of joint surface. *BMC Sports Science, Medicine and Rehabilitation.* 2010;2(1):1.

78. Kaushal SG, Barnett SC, Hosseinzadeh S, Perrone GS, Kiapour AM. Changes in Functional Meniscal Morphology During Skeletal Growth and Maturation. *Orthopaedic Journal of Sports Medicine.* 2024;12(3):23259671241237810.

79. Khader F, Müller-Franzes G, Tayebi Arasteh S, et al. Denoising diffusion probabilistic models for 3D medical image generation. *Scientific Reports.* 2023;13(1):7303.

80. Kiapour AM, Ecklund K, Murray MM, et al. Changes in cross-sectional area and signal intensity of healing anterior cruciate ligaments and grafts in the first 2 years after surgery. *The American journal of sports medicine.* 2019;47(8):1831-1843.

81. Kiapour AM, Flannery SW, Murray MM, et al. Regional differences in anterior cruciate ligament signal intensity after surgical treatment. *The American journal of sports medicine.* 2021;49(14):3833-3841.

82. Kim J, Lee J, Lee S, Lee M. Development of 3-D stereo endoscopic PACS viewer. *ISIE 2001 2001 IEEE International Symposium on Industrial Electronics Proceedings (Cat No 01TH8570).* 2001;1:278-280.

83. Kim J, Park H. Adaptive latent diffusion model for 3d medical image to image translation: Multi-modal magnetic resonance imaging study. *Proceedings of the IEEE/CVF Winter conference on applications of computer Vision.* 2024:7604-7613.

84. Knuesel PR, Pfirrmann CW, Noetzli HP, et al. MR arthrography of the hip: diagnostic performance of a dedicated water-excitation 3D double-echo steady-state sequence to detect cartilage lesions. *American Journal of Roentgenology.* 2004;183(6):1729-1735.

85. Koga H, Zaffagnini S, Getgood AM, Muneta T. ACL graft selection: state of the art. *Journal of ISAKOS.* 2018;3(3):177-184.

86. Koo JH, Choi SH, Lee SA, Wang JH. Comparison of Medial and Lateral Meniscus Root Tears. *PLoS One.* 2015;10(10):e0141021.

87. Kornaat PR, Bloem JL, Ceulemans RY, et al. Osteoarthritis of the knee: association between clinical features and MR imaging findings. *Radiology.* 2006;239(3):811-817.

88. Kuczyński N, Boś J, Białoskórska K, et al. The Meniscus: Basic Science and Therapeutic Approaches. *Journal of Clinical Medicine.* 2025;14(6):2020.

89. Kumm J, Roemer FW, Guermazi A, Turkiewicz A, Englund M. Natural history of intrameniscal signal intensity on knee MR images: six years of data from the osteoarthritis initiative. *Radiology.* 2016;278(1):164-171.

90. Lalithakumari S, Pandian R, Rani J, et al. Selection of optimum compression algorithms based on the characterization on feasibility for medical image. *Biomedical Research (0970-938X).* 2017;28(13).

91. Lansdown DA, Xiao W, Zhang AL, et al. Quantitative imaging of anterior cruciate ligament (ACL) graft demonstrates longitudinal compositional changes and relationships with clinical outcomes at 2 years after ACL reconstruction. *Journal of Orthopaedic Research®.* 2020;38(6):1289-1295.

92. Lee J-J, Choi Y-J, Shin K-Y, Choi C-H. Medial meniscal tears in anterior cruciate ligament-deficient knees: effects of posterior tibial slope on medial meniscal tear. *Knee Surgery and Related Research.* 2011;23(4):227-230.

93. Li P, TSAi T-Y, Li J-S, et al. Morphological measurement of the knee: race and sex effects. *Acta Orthop Belg.* 2014;80(2):260-268.

94. Liu S, Thung K-H, Qu L, et al. Learning MRI artefact removal with unpaired data. *Nature Machine Intelligence.* 2021;3(1):60-67.

95. Liudahl AA, Davis AB, Liudahl DS, et al. Diagnosis of small vestibular schwannomas using constructive interference steady state sequence. *The Laryngoscope.* 2018;128(9):2128-2132.

96. Losina E, Weinstein AM, Reichmann WM, et al. Lifetime risk and age at diagnosis of symptomatic knee osteoarthritis in the US. *Arthritis care & research.* 2013;65(5):703-711.

97. Luczkiewicz P, Daszkiewicz K, Witkowski W, et al. The influence of a change in the meniscus cross-sectional shape on the medio-lateral translation of the knee joint and meniscal extrusion. *PLoS One.* 2018;13(2):e0193020.

98. Luhmann SJ. Acute traumatic knee effusions in children and adolescents. *Journal of Pediatric Orthopaedics.* 2003;23(2):199-202.

99. Maas SA, Ellis BJ, Ateshian GA, Weiss JA. FEBio: finite elements for biomechanics. 2012.

100. Macaulay AA, Perfetti DC, Levine WN. Anterior cruciate ligament graft choices. *Sports health.* 2012;4(1):63-68.

101. Mahfouz M, Fatah EEA, Bowers LS, Scuderi G. Three-dimensional morphology of the knee reveals ethnic differences. *Clinical Orthopaedics and Related Research®.* 2012;470(1):172-185.

102. Maletis GB, Granan L-P, Inacio MC, Funahashi TT, Engebretsen L. Comparison of community-based ACL reconstruction registries in the US and Norway. *JBJS.* 2011;93(Supplement_3):31-36.

103. Mallika Singh J-YK, Alexandra Santos, Leah Gilreath, Biya Brooks, Shankar G. Kaushal, Dominique A. Barnes, Braden C. Fleming, Ata M. Kiapour. A Fully Automated Multi-Tissue Multi-Sequence Knee Segmentation Pipeline For Studying Soft Tissue And Bony Structures in 3D. *Orthopaedic Research Society.* 2024.

104. Mameri ES, Dasari SP, Fortier LM, et al. Review of meniscus anatomy and biomechanics. *Current reviews in musculoskeletal medicine.* 2022;15(5):323-335.

105. MathWorks. pca (R2023a). 2025:MATLAB function that returns the principal component analysis of raw data.

106. MathWorks. stlread (R2023a). 2025:MATLAB function to import STL files.

107. McDermott I, Amis A. The consequences of meniscectomy. *The Journal of Bone & Joint Surgery British Volume.* 2006;88(12):1549-1556.

108. McDermott ID, Masouros SD, Amis AA. Biomechanics of the menisci of the knee. *Current Orthopaedics.* 2008;22(3):193-201.

109. McNaughton J, Fernandez J, Holdsworth S, et al. Machine learning for medical image translation: A systematic review. *Bioengineering.* 2023;10(9):1078.

110. McRobbie DW, Moore EA, Graves MJ, Prince MR. *MRI from Picture to Proton.* Cambridge university press; 2017.

111. Menghini D, Kaushal SG, Flannery SW, et al. Three-Dimensional MRI Analysis Shows Sex-Specific Patterns in Changes in Anterior Cruciate Ligament Cross-Sectional Area Along Its Length. *Journal of orthopaedic research: official publication of the Orthopaedic Research Society.* 2022;41(4):771.

112. Middleton K, Hamilton T, Irrgang J, et al. Anatomic anterior cruciate ligament (ACL) reconstruction: a global perspective. Part 1. *Knee Surgery, Sports Traumatology, Arthroscopy.* 2014;22(7):1467-1482.

113. Mohamadi A, Momenzadeh K, Masoudi A, et al. Evolution of knowledge on meniscal biomechanics: a 40 year perspective. *BMC Musculoskeletal Disorders.* 2021;22:1-13.

114. Moksnes H, Engebretsen L, Risberg MA. Prevalence and incidence of new meniscus and cartilage injuries after a nonoperative treatment algorithm for ACL tears in skeletally immature children: a prospective MRI study. *The American Journal of Sports Medicine.* 2013;41(8):1771-1779.

115. Muller B, Yabroudi MA, Lynch A, et al. Defining thresholds for the patient acceptable symptom state for the IKDC subjective knee form and KOOS for patients who underwent ACL reconstruction. *The American journal of sports medicine.* 2016;44(11):2820-2826.

116. Müller-Franzes G, Niehues JM, Khader F, et al. A multimodal comparison of latent denoising diffusion probabilistic models and generative adversarial networks for medical image synthesis. *Scientific Reports.* 2023;13(1):12098.

117. Murray MM, Fleming BC. Use of a Bioactive Scaffold to Stimulate Anterior Cruciate Ligament Healing Also Minimizes Posttraumatic Osteoarthritis After Surgery. *The American Journal of Sports Medicine.* 2013;41(8):1762-1770.

118. Murray MM, Fleming BC, Badger GJ, et al. Bridge-Enhanced Anterior Cruciate Ligament Repair Is Not Inferior to Autograft Anterior Cruciate Ligament Reconstruction at 2 Years: Results of a Prospective Randomized Clinical Trial. *The American Journal of Sports Medicine.* 2020;48(6):1305-1315.

119. Murray MM, Flutie BM, Kalish LA, et al. The bridge-enhanced anterior cruciate ligament repair (BEAR) procedure: an early feasibility cohort study. *Orthopaedic Journal of Sports Medicine.* 2016;4(11):2325967116672176.

120. Murray MM, Kalish LA, Fleming BC, et al. Bridge-Enhanced Anterior Cruciate Ligament Repair: Two-Year Results of a First-in-Human Study. *Orthopaedic Journal of Sports Medicine.* 2019;7(3):232596711882435.

121. Murray MM, Kiapour AM, Kalish LA, et al. Predictors of healing ligament size and magnetic resonance signal intensity at 6 months after bridge-enhanced anterior cruciate ligament repair. *The American journal of sports medicine.* 2019;47(6):1361-1369.

122. Nebelung S, Dötsch L, Shah D, et al. Functional MRI mapping of human meniscus functionality and its relation to degeneration. *Scientific reports.* 2020;10(1):2499.

123. Nebelung S, Tingart M, Pufe T, et al. Ex vivo quantitative multiparametric MRI mapping of human meniscus degeneration. *Skeletal radiology.* 2016;45(12):1649-1660.

124. Ng H, Ong S, Foong K, Goh P-S, Nowinski W. Medical image segmentation using k-means clustering and improved watershed algorithm. *2006 IEEE southwest symposium on image analysis and interpretation.* 2006:61-65.

125. Nordenvall R, Bahmanyar S, Adami J, Mattila VM, Felländer-Tsai L. Cruciate ligament reconstruction and risk of knee osteoarthritis: the association between cruciate ligament injury and post-traumatic osteoarthritis. a population based nationwide study in Sweden, 1987–2009. *PloS one.* 2014;9(8):e104681.

126. Noyes FR, Barber-Westin SD. Treatment of meniscus tears during anterior cruciate ligament reconstruction. *Arthroscopy: The Journal of Arthroscopic & Related Surgery.* 2012;28(1):123-130.

127. Noyes FR, Butler D, Grood ES, Zernicke RF, Hefzy M. Biomechanical analysis of human ligament grafts used in knee-ligament repairs and reconstructions. *JBJS.* 1984;66(3):344-352.

128. Nukuto K, Konstantinou E, Wackerle AM, et al. Meniscus tears in the setting of anterior cruciate ligament injury. *Journal of Joint Surgery and Research.* 2024;2(4):180-188.

129. Oak SR, O'Rourke C, Strnad G, et al. Statistical comparison of the pediatric versus adult IKDC subjective knee evaluation form in adolescents. *The American Journal of Sports Medicine.* 2015;43(9):2216-2221.

130. Papageorgiou CD, Gil JE, Kanamori A, et al. The biomechanical interdependence between the anterior cruciate ligament replacement graft and the medial meniscus. *The American journal of sports medicine.* 2001;29(2):226-231.

131. Pappas TN, Jayant NS. An adaptive clustering algorithm for image segmentation. *International Conference on Acoustics, Speech, and Signal Processing.* 1989:1667-1670.

132. Parsons F. The characters of the English thigh-bone. *Journal of Anatomy and physiology.* 1914;48(Pt 3):238.

133. Pasiński M, Zabrzyńska M, Adamczyk M, et al. A current insight into human knee menisci. *Translational Research in Anatomy.* 2023;32:100259.

134. Pataky TC, Robinson MA, Vanrenterghem J. Region-of-interest analyses of one-dimensional biomechanical trajectories: bridging 0D and 1D theory, augmenting statistical power. *PeerJ.* 2016;4:e2652.

135. Paterno MV, Rauh MJ, Schmitt LC, Ford KR, Hewett TE. Incidence of second ACL injuries 2 years after primary ACL reconstruction and return to sport. *The American journal of sports medicine.* 2014;42(7):1567-1573.

136. Peterfy C, Gold G, Eckstein F, et al. MRI protocols for whole-organ assessment of the knee in osteoarthritis. *Osteoarthritis and cartilage.* 2006;14:95-111.

137. Pham DL, Xu C, Prince JL. Current methods in medical image segmentation. *Annual review of biomedical engineering.* 2000;2(1):315-337.

138. Pinaya WH, Tudosiu P-D, Dafflon J, et al. Brain imaging generation with latent diffusion models. *MICCAI workshop on deep generative models.* 2022:117-126.

139. Pruneski JA, Heyworth BE, Kocher MS, et al. Prevalence and predictors of concomitant meniscal and ligamentous injuries associated with ACL surgery: an analysis of 20 years of ACL reconstruction at a tertiary care children's hospital. *The American Journal of Sports Medicine.* 2024;52(1):77-86.

140. Putnis SE, Oshima T, Klasan A, et al. Magnetic resonance imaging 1 year after hamstring autograft anterior cruciate ligament reconstruction can identify those at higher risk of graft failure: An analysis of 250 cases. *Am J Sports Med.* 2021:363546521995512.

141. Rabottino G, Mencattini A, Salmeri M, Caselli F, Lojacono R. Mass contour extraction in mammographic images for breast cancer identification. *16th IMEKO TC4 Symposium, Exploring New Frontiers of Instrumentation and Methods for Electrical and Electronic Measurements, Florence, Italy.* 2008:11-15.

142. Ray S. Determination of number of clusters in k-means clustering and application in colour image segmentation. *Proc 4th International Conference on Advances in Pattern Recognition and Digital Techniques (ICAPRDT'99).* 1999:137-143.

143. Read PJ, Michael Auliffe S, Wilson MG, Graham-Smith P. Lower Limb Kinetic Asymmetries in Professional Soccer Players With and Without Anterior Cruciate Ligament Reconstruction: Nine Months Is Not Enough Time to Restore "Functional" Symmetry or Return to Performance. *The American Journal of Sports Medicine.* 2020;48(6):1365-1373.

144. Reinke EK, Spindler KP, Lorring D, et al. Hop tests correlate with IKDC and KOOS at minimum of 2 years after primary ACL reconstruction. *Knee Surgery, Sports Traumatology, Arthroscopy.* 2011;19:1806-1816.

145. Reist H, Vacek PM, Endres N, et al. Risk factors for concomitant meniscal injury with sport-related anterior cruciate ligament injury. *Orthopaedic Journal of Sports Medicine.* 2023;11(9):23259671231196492.

146. Retzky JS, Koff MF, Nwawka OK, Rodeo SA. Novel noninvasive imaging techniques to assess structural, functional, and material properties of tendon, ligament, and cartilage: a narrative review of current concepts. *Orthopaedic Journal of Sports Medicine.* 2025;13(2):23259671251317223.

147. Rezaee K, Haddadnia J. Designing an algorithm for cancerous tissue segmentation using adaptive k-means cluttering and discrete wavelet transform. *Journal of biomedical physics & engineering.* 2013;3(3):93.

148. Roca V, Kuchcinski G, Pruvo J-P, Manouvriez D, Lopes R. IGUANe: A 3D generalizable CycleGAN for multicenter harmonization of brain MR images. *Medical Image Analysis.* 2025;99:103388.

149. Roman MD, Mohor CI, Melinte PR, et al. Meniscal tear management associated with ACL reconstruction. *Applied Sciences.* 2022;12(12):6175.

150. Røtterud JH, Sivertsen EA, Forssblad M, Engebretsen L, Årøen A. Effect of meniscal and focal cartilage lesions on patient-reported outcome after anterior cruciate ligament reconstruction: a nationwide cohort study from Norway and Sweden of 8476 patients with 2-year follow-up. *The American journal of sports medicine.* 2013;41(3):535-543.

151. Salmon LJ, Heath E, Akrawi H, et al. 20-Year Outcomes of Anterior Cruciate Ligament Reconstruction With Hamstring Tendon Autograft: The Catastrophic Effect of Age and Posterior Tibial Slope. *Am J Sports Med.* 2018;46(3):531-543.

152. Saltzman CL, Zimmerman MB, O'Rourke M, et al. Impact of comorbidities on the measurement of health in patients with ankle osteoarthritis. *JBJS.* 2006;88(11):2366-2372.

153. Salvador S, Chan P. Determining the number of clusters/segments in hierarchical clustering/segmentation algorithms. *16th IEEE international conference on tools with artificial intelligence.* 2004:576-584.

154. Sanborn RM, Badger GJ, Fleming BC, et al. Preoperative Risk Factors for Subsequent Ipsilateral ACL Revision Surgery After an ACL Restoration Procedure. *The American Journal of Sports Medicine.* 2023;51(1):49-57.

155. Sasaki N, Farraro KF, Kim KE, Woo SL. Biomechanical evaluation of the quadriceps tendon autograft for anterior cruciate ligament reconstruction: a cadaveric study. *The American journal of sports medicine.* 2014;42(3):723-730.

156. Sathya B, Manavalan R. Image segmentation by clustering methods: performance analysis. *International Journal of Computer Applications.* 2011;29(11):27-32.

157. Scheffler K, Lehnhardt S. Principles and applications of balanced SSFP techniques. *European radiology.* 2003;13(11):2409-2418.

158. Schleich C, Hesper T, Hosalkar HS, et al. 3D double-echo steady-state sequence assessment of hip joint cartilage and labrum at 3 Tesla: comparative analysis of magnetic resonance imaging and intraoperative data. *European radiology.* 2017;27(10):4360-4371.

159. Schmitz RJ, Wang H-M, Kraft RA, et al. Regional differences in anterior cruciate ligament imaging biomarkers: T2 and T2* values. *Muscles, Ligaments & Tendons Journal (MLTJ).* 2018;8(2).

160. Segal NA, Anderson DD, Iyer KS, et al. Baseline articular contact stress levels predict incident symptomatic knee osteoarthritis development in the MOST cohort. *Journal of orthopaedic research.* 2009;27(12):1562-1568.

161. Shapiro LM, McWalter EJ, Son MS, et al. Mechanisms of osteoarthritis in the knee: MR imaging appearance. *Journal of magnetic resonance imaging.* 2014;39(6):1346-1356.

162. Shelbourne KD, Roberson TA, Gray T. Long-term evaluation of posterior lateral meniscus root tears left in situ at the time of anterior cruciate ligament reconstruction. *The American Journal of Sports Medicine.* 2011;39(7):1439-1443.

163. Shimomura K, Hamamoto S, Hart DA, Yoshikawa H, Nakamura N. Meniscal repair and regeneration: Current strategies and future perspectives. *Journal of clinical orthopaedics and trauma.* 2018;9(3):247-253.

164. Shrive N, O'connor J, Goodfellow J. Load-bearing in the knee joint. *Clinical Orthopaedics and Related Research (1976-2007).* 1978;131:279-287.

165. Shybut TB, Vega CE, Haddad J, et al. Effect of lateral meniscal root tear on the stability of the anterior cruciate ligament–deficient knee. *The American journal of sports medicine.* 2015;43(4):905-911.

166. Sinaga KP, Yang M-S. Unsupervised K-means clustering algorithm. *IEEE access.* 2020;8:80716-80727.

167. Skandarani Y, Jodoin P-M, Lalande A. Gans for medical image synthesis: An empirical study. *Journal of Imaging.* 2023;9(3):69.

168. Slauterbeck JR, Kousa P, Clifton BC, et al. Geographic mapping of meniscus and cartilage lesions associated with anterior cruciate ligament injuries. *The Journal of Bone and Joint Surgery American Volume.* 2009;91(9):2094.

169. Sommerfeldt M, Raheem A, Whittaker J, Hui C, Otto D. Recurrent instability episodes and meniscal or cartilage damage after anterior cruciate ligament injury:

a systematic review. *Orthopaedic journal of sports medicine.* 2018;6(7):2325967118786507.

170. Staroswiecki E, Granlund KL, Alley MT, Gold GE, Hargreaves BA. Simultaneous estimation of T2 and apparent diffusion coefficient in human articular cartilage in vivo with a modified three-dimensional double echo steady state (DESS) sequence at 3 T. *Magnetic resonance in medicine.* 2012;67(4):1086-1096.

171. Sun X, Shi L, Luo Y, et al. Histogram-based normalization technique on human brain magnetic resonance images from different acquisitions. *BioMedical Engineering OnLine.* 2015;14(1).

172. Taubin G. Estimation of planar curves, surfaces, and nonplanar space curves defined by implicit equations with applications to edge and range image segmentation. *IEEE Transactions on Pattern Analysis & Machine Intelligence.* 1991;13(11):1115-1138.

173. Tibor L, Chan PH, Funahashi TT, et al. Surgical technique trends in primary ACL reconstruction from 2007 to 2014. *JBJS.* 2016;98(13):1079-1089.

174. Torres L, Dunlop DD, Peterfy C, et al. The relationship between specific tissue lesions and pain severity in persons with knee osteoarthritis. *Osteoarthritis and cartilage.* 2006;14(10):1033-1040.

175. Tsai P-H, Chou M-C, Lee H-S, et al. MR T2 values of the knee menisci in the healthy young population: zonal and sex differences. *Osteoarthritis and cartilage.* 2009;17(8):988-994.

176. Ushio T, Okazaki K, Osaki K, et al. Degenerative changes in cartilage likely occur in the medial compartment after anterior cruciate ligament reconstruction. *Knee Surgery, Sports Traumatology, Arthroscopy.* 2019;27(11):3567-3574.

177. Van der Walt S, Schönberger JL, Nunez-Iglesias J, et al. scikit-image: image processing in Python. *PeerJ.* 2014;2:e453.

178. Van Dyck P, Zazulia K, Smekens C, et al. Assessment of Anterior Cruciate Ligament Graft Maturity With Conventional Magnetic Resonance Imaging: A Systematic Literature Review. *Orthopaedic Journal of Sports Medicine.* 2019;7(6):232596711984901.

179. van Eck CF, Loopik M, van den Bekerom MP, Fu FH, Kerkhoffs GM. Methods to diagnose acute anterior cruciate ligament rupture: a meta-analysis of instrumented knee laxity tests. *Knee Surgery, Sports Traumatology, Arthroscopy.* 2013;21:1989-1997.

180. Vavken P, Fleming BC, Mastrangelo AN, Machan JT, Murray MM. Biomechanical Outcomes After Bioenhanced Anterior Cruciate Ligament Repair and Anterior Cruciate Ligament Reconstruction Are Equal in a Porcine Model. *Arthroscopy: The Journal of Arthroscopic & Related Surgery.* 2012;28(5):672-680.

181. Voloshin AS, Wosk J. Shock absorption of meniscectomized and painful knees: a comparative in vivo study. *Journal of biomedical engineering.* 1983;5(2):157-161.

182. Vrancken A, Crijns S, Ploegmakers M, et al. 3D geometry analysis of the medial meniscus–a statistical shape modeling approach. *Journal of anatomy.* 2014;225(4):395-402.

183. Walker PS, Arno S, Bell C, et al. Function of the medial meniscus in force transmission and stability. *Journal of biomechanics.* 2015;48(8):1383-1388.

184. Walker PS, Erkiuan MJ. The role of the menisci in force transmission across the knee. *Clinical Orthopaedics and Related Research®.* 1975;109:184-192.

185. Wang L, Lai HM, Barker GJ, Miller DH, Tofts PS. Correction for variations in MRI scanner sensitivity in brain studies with histogram matching. *Magnetic Resonance in Medicine.* 1998;39(2):322-327.

186. Webb JM, Salmon LJ, Leclerc E, Pinczewski LA, Roe JP. Posterior tibial slope and further anterior cruciate ligament injuries in the anterior cruciate ligament–reconstructed patient. *The American journal of sports medicine.* 2013;41(12):2800-2804.

187. Weiler A, Peters G, Maurer J, Unterhauser FN, Sudkamp NP. Biomechanical properties and vascularity of an anterior cruciate ligament graft can be predicted by contrast-enhanced magnetic resonance imaging - A two-year study in sheep. *Am J Sports Med.* 2001;29(6):751-761.

188. Welander P, Karlsson S, Eklund A. Generative adversarial networks for image-to-image translation on multi-contrast mr images-a comparison of cyclegan and unit. *arXiv preprint arXiv:180607777.* 2018.

189. Welling W, Benjaminse A, Seil R, et al. Low rates of patients meeting return to sport criteria 9 months after anterior cruciate ligament reconstruction: a

prospective longitudinal study. *Knee Surgery, Sports Traumatology, Arthroscopy.* 2018;26(12):3636-3644.

190. Wellsandt E, Failla MJ, Axe MJ, Snyder-Mackler L. Does anterior cruciate ligament reconstruction improve functional and radiographic outcomes over nonoperative management 5 years after injury? *The American journal of sports medicine.* 2018;46(9):2103-2112.

191. Widner M, Dunleavy M, Lynch S. Outcomes following ACL reconstruction based on graft type: are all grafts equivalent? *Current reviews in musculoskeletal medicine.* 2019;12(4):460-465.

192. Wirth W, Frobell RB, Souza RB, et al. A three-dimensional quantitative method to measure meniscus shape, position, and signal intensity using MR images: A pilot study and preliminary results in knee osteoarthritis. *Magnetic Resonance in Medicine.* 2010;63(5):1162-1171.

193. Xergia SA, Pappas E, Zampeli F, Georgiou S, Georgoulis AD. Asymmetries in functional hop tests, lower extremity kinematics, and isokinetic strength persist 6 to 9 months following anterior cruciate ligament reconstruction. *Journal of Orthopaedic & Sports Physical Therapy.* 2013;43(3):154-162.

194. Yamasaki S, Hashimoto Y, Nishida Y, et al. Assessment of meniscal healing status by magnetic resonance imaging T2 mapping after meniscal repair. *The American Journal of Sports Medicine.* 2020;48(4):853-860.

195. Zarins Z, Bolbos R, Pialat J, et al. Cartilage and meniscus assessment using T1rho and T2 measurements in healthy subjects and patients with osteoarthritis. *Osteoarthritis and cartilage.* 2010;18(11):1408-1416.

196. Zheng X, Lei Q, Yao R, Gong Y, Yin Q. Image segmentation based on adaptive K-means algorithm. *EURASIP Journal on Image and Video Processing.* 2018;2018(1):1-10.

197. Zhu J-Y, Park T, Isola P, Efros AA. Unpaired image-to-image translation using cycle-consistent adversarial networks. *Proceedings of the IEEE international conference on computer vision.* 2017:2223-2232.

Appendix A: Finite Element Analysis of Meniscal Contact Mechanics and Morphological Changes Following ACL Surgery

Dominique A. Barnes, Crystal J. Murray, Ata M. Kiapour, Jillian E. Beveridge,

Mohammadreza Movahhedi, Martha M. Murray, Braden C. Fleming

Introduction: The meniscus' primary function is to distribute load, a function dependent on its shape and size.[182] Meniscal injuries often occur concurrently with ACL injuries to increase the risk of early-onset OA.[139] These injuries can compromise the morphological structure of the meniscus, which may impair its ability to distribute axial tibiofemoral forces, a key function in stabilizing the joint during articulation.[97] Therefore, this study aimed to compare the CSA profiles of medial and lateral menisci between male and female subjects using SPM.[134] Furthermore, we investigate whether differences in CSA correspond to variations in contact areas and pressures experienced during static loading. We hypothesized that the female medial and lateral menisci CSA profiles, even when normalized by knee size, are smaller than male profiles following ACL surgery.

Methods: Data were collected from 105 subjects (70 females and 35 males, median age 17.6) who underwent unilateral ACL surgery and MRI at six months post-surgery. The medial and lateral menisci of the surgical knee were automatically segmented from CISS image stack using a custom software (Figure A. 1).[103] Cross-sectional profiles that describe the changes throughout the menisci were generated by rotating an intersecting plane around the meniscus (Figure A. 2). Sixty CSA measurements, equally spaced about the rotational axis, were made ranging from the anterior root (0%) to the posterior root (100%) (Figure A. 3). Each CSA values were normalized to the mediolateral bicondylar width of the knee to account for differences due to knee size. SPM was used to conduct two-tailed t-tests at each of the sixty positions to compare the CSA profile differences between sexes. A finite element model (FEM) was developed in FEBio using the automatically segmented geometry from an MRI of a randomly selected female subject included in our cohort (Figure A. 4).[99] The model consisted of the femur and tibia

represented as rigid bodies, with the tibia fixed in 6 degrees of freedom and the femur fixed in 5 degrees of freedom, with axial displacement (z-axis) not fixed. No ligaments were included in the model. The menisci and articular cartilages were modeled as a hyperelastic material. The femoral cartilage was rigidly fixed to the femur, and the tibial cartilages and menisci were fixed to the tibia. Sliding contacts were applied between the articular cartilages and the menisci. Axial displacement in the z-axis was placed to the femur in full extension to identify the peak contact areas between the femur and menisci, specifically the medial meniscus.

Results: No significant differences were found between the normalized lateral meniscus CSA of the surgical knee in males and females. However, in the medial meniscus, females exhibited a mean percent difference of 129% and 13.1% CSA compared to males in the anterior and posterior region respectively ($p<.001$) (Figure A. 5). The FE model revealed that peak contact between the femur and medial meniscus during static axial displacement occurred in the same region where we identified significant CSA differences (Figure A. 5).

Discussion: The spatial overlap between the changes in CSA and peak contact area between the medial meniscus and the femur emphasizes the biomechanical relationship between load distribution and meniscal morphology. The similarities between the significant differences in the medial meniscus CSA and high-contact area may indicate altered load distribution in female patients post-ACL surgery, potentially increasing the risk of early osteoarthritic changes. Identifying the specific regions of the meniscus that undergo changes after surgery, particularly in female patients, may inform the development of targeted rehabilitation strategies aimed at reducing post-surgical OA risk.

Future research should focus on incorporating dynamic loading conditions into the subject-specific FE models to better capture the complex biomechanics of the femur-meniscus interaction. By integrating patient-specific geometries and loading scenarios, we can improve the accuracy of contact stresses and better understand how post-ACL surgery morphological changes influence joint mechanics over time.

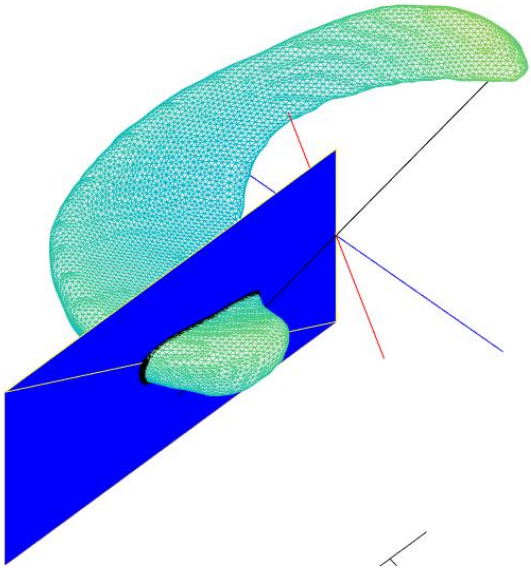

Figure A. 1. Plane perpendicular to meniscal arc length intersecting 3D model of medial meniscus

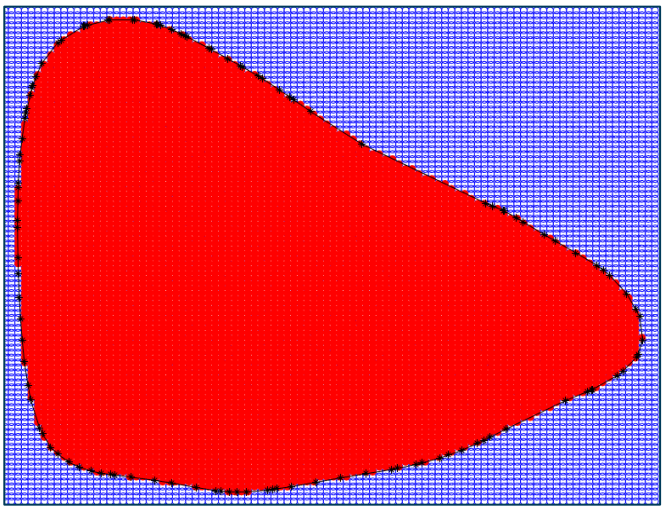

Figure A. 2. Cross-sectional area profile of medial meniscus intersected with plane.

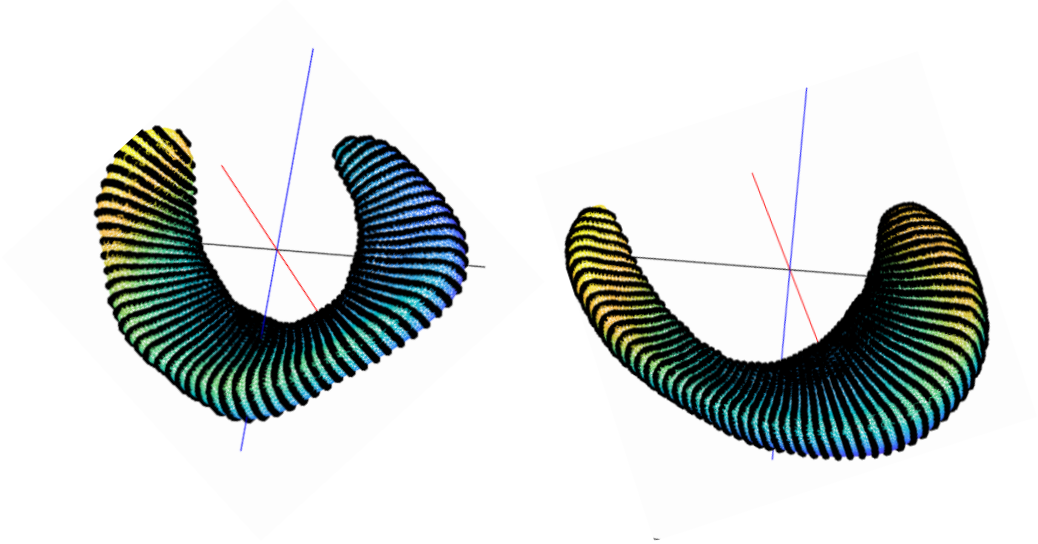

Figure A. 3. Sixty equally spaced CSA measures of the lateral (left) and medial (right) menisci

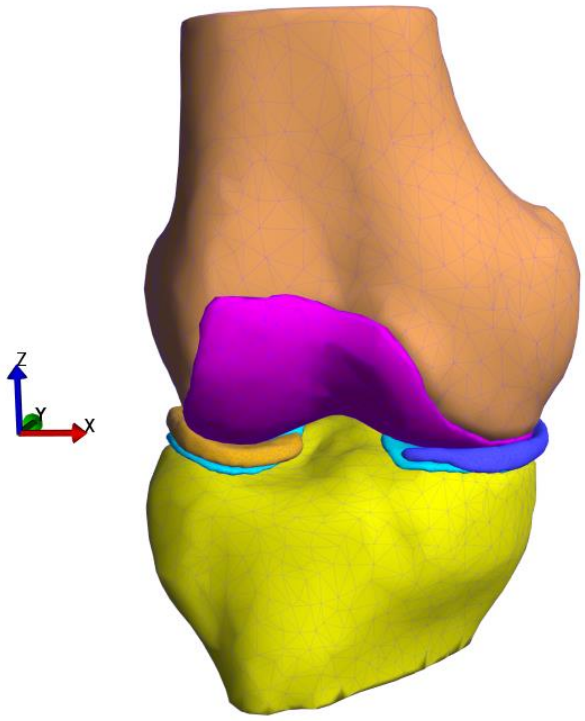

Figure A. 4. FEBio Model of female subject's knee using segmented geometry from MRI

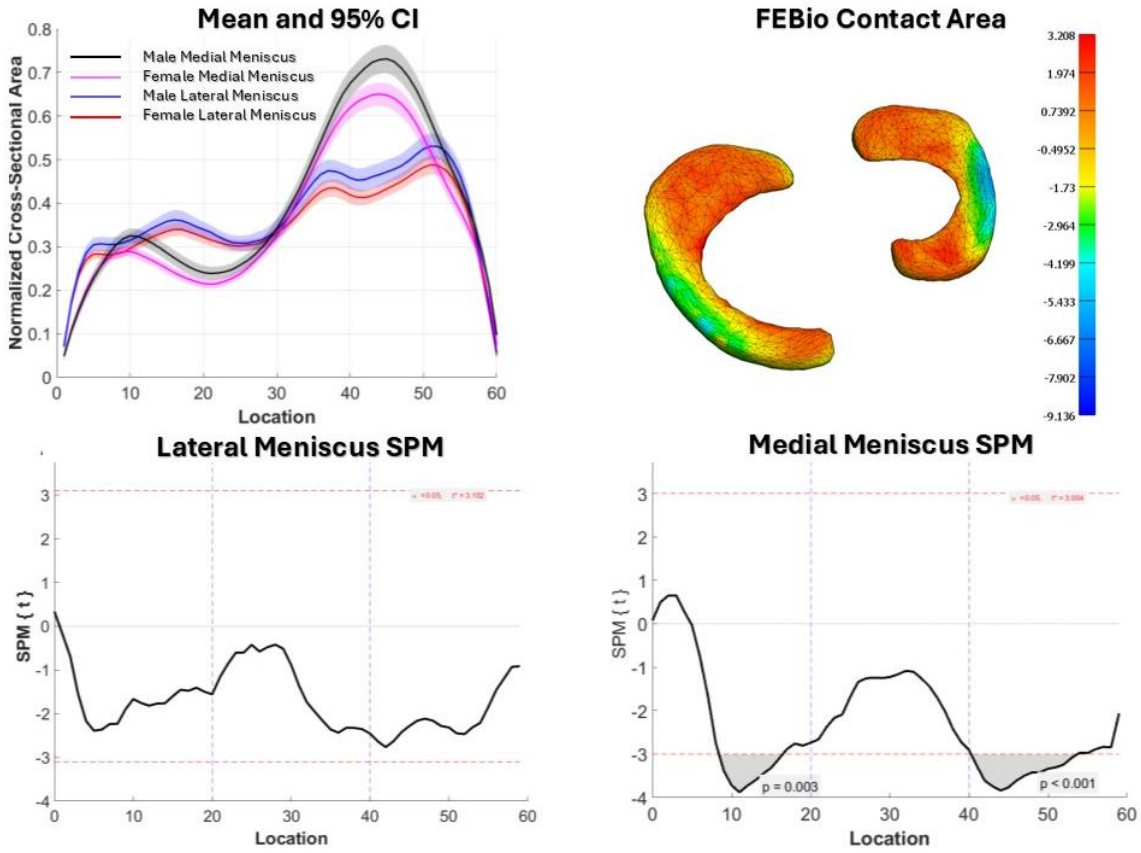

Figure A. 5. Mean and 95% Confidence Interval of the lateral and medial menisci of both sexes (top left); FEBio Contact Area analysis of femur-meniscus contact (top right); Lateral meniscus SPM (bottom left); Medial meniscus SPM (bottom right)

Appendix B: Previous Methods Used to Attempt DESS to CISS MRI Sequence Transformations

Dominique A. Barnes

Introduction: Chapter 6 develops the work on utilizing CycleGAN networks to accomplish the tasks of MRI sequence-to-sequence transformation. However, the CycleGAN did not prove to be successful in capturing the intricate details of the CISS sequence when using a DESS image to do the transformation. Previous methods were used before implementing machine learning to complete this task. The first method was called Ratio of Mean Intensities (RMI).[185] RMI was calculated by collecting the average signal intensities of the subject's ACL and bone and using the values to scale the DESS scans to CISS scans. The next method used was called histogram matching, which works similarly to RMI, but focuses on scaling the histograms of the signal intensities to match the DESS distribution to the CISS distribution.[171] The final method was to advance the presented CycleGAN to remove the grid-like patterns from the output images when transforming between the DESS and CISS-like images. However, none of these methods proved to perform better than the CycleGAN method proposed in Chapter 6. The remainder of this appendix will evaluate the advantages and disadvantages of the three additional methods: 1) Ratio of Mean Intensities; 2) Histogram Matching; 3) Non-Grid CycleGAN.

Methods

All MRI scans of the patients included in this study were conducted on a 3T TRIO (Siemens; Erlangen, Germany) using a 15-channel transmit/receive knee coil (Siemens). Data were collected from CISS (FA = 35deg; TR = 12.78ms; TE = 6.39ms; FOV = 140mm) scans and DESS (FA = 25deg; TR = 16.48ms; TE = 4.83ms) scans. Only MR images of the non-injured contralateral limbs were used for these studies.

Ratio of Means Intensities: Data was acquired from patients enrolled in the BEAR I, BEAR II, and ACL reconstruction subjects of the tension trial. CISS scans were collected from BEAR I (CISS = 16; DESS = 11) and BEAR II (CISS = 49; DESS = 35) patients.[118] DESS scans were collected from 35 patients from the ACL reconstruction tension trial. The ACL was segmented from the patient's MR image stack. RMI was calculated by collecting the average SI of the ACL of all the patients for both the CISS and DESS scans. The averages were then divided by each other to create the RMI value (Eq. 1). The SI values of the DESS scans were then scaled using the RMI value (Eq. 1). The process was repeated for the cortical bone values from the DESS scans. The adjusted average bone and ACL values were then used in the log normalization equation (Eq. 2). BEAR I and BEAR II had paired data, therefore, a Wilcoxon signed-rank test was performed to determine significant differences between the CISS and DESS adjusted SI values. The tension study had no CISS scans, therefore, this test was not able to be performed.

$$RMI = \frac{Average\ SI\ ACL_{DESS}}{Average\ SI\ ACL_{CISS}} \quad \text{(Eq. 3)}$$

$$SI_{scaled} = \log_2\left(\frac{SI_{ACL} + \Delta Noise}{SI_{Bone} + \Delta Noise}\right) \quad \text{(Eq.2)}$$

Histogram Matching: Data was acquired from patients enrolled in the BEAR I and BEAR II. CISS scans were collected from BEAR I (CISS = 16; DESS = 11) and BEAR II (CISS = 49; DESS = 35) patients.[118] The goal of histogram matching can be thought of as a "transformation", where the contents of the histogram do not change, but rather the distribution of pixel intensities matches the distribution of the target histogram. Histogram matching uses piecewise linear interpolation between the pixel values of the

input image and counts from the flattened 1-Dimensional version along with the source image.[56,177] The cumulative distribution function of the source image pixel values is then calculated, and this step is repeated for the reference image. The source image quantities based on the reference image quantiles are used to find the interpolated values. The interpolated values are then used to reshape the resulting histogram of the source image to match that of the reference image's shape.[56,177] MAE was calculated using Equation 3 between the CISS histogram values (reference image) and the adjusted DESS histogram values (source image).

$$MAE = \frac{1}{n} * \Sigma \, |DESS\ Matched\ SI - CISS\ SI| \qquad \text{(Eq. 4)}$$

Non-Grid CycleGAN: Reference Chapter 6.3.1 and Chapter 6.3.2 for the data source and data preprocessing used for this study. The architecture for the CycleGAN was relatively the same, with the exception of updating the convolutional layers to include upsampling layers. The goal of this approach was to ensure that uniformity was maintained along the spatial scaling, and smoother outputs were observed, removing the grid-like artifacts.

Results

Ratio of Means Intensities: The Wilcoxon signed-rank test with a p-value less than or equal to 0.05 would indicate significance for this study, however, this test could not be performed on the tension study patients. The p-value for BEAR I was found to be 0.10, and for BEAR II was 0.002. This indicated that the difference between CISS and DESS adjusted value was not significantly different for BEAR I, however, for BEAR II, the values were found to be significantly different (Figure B. 1)

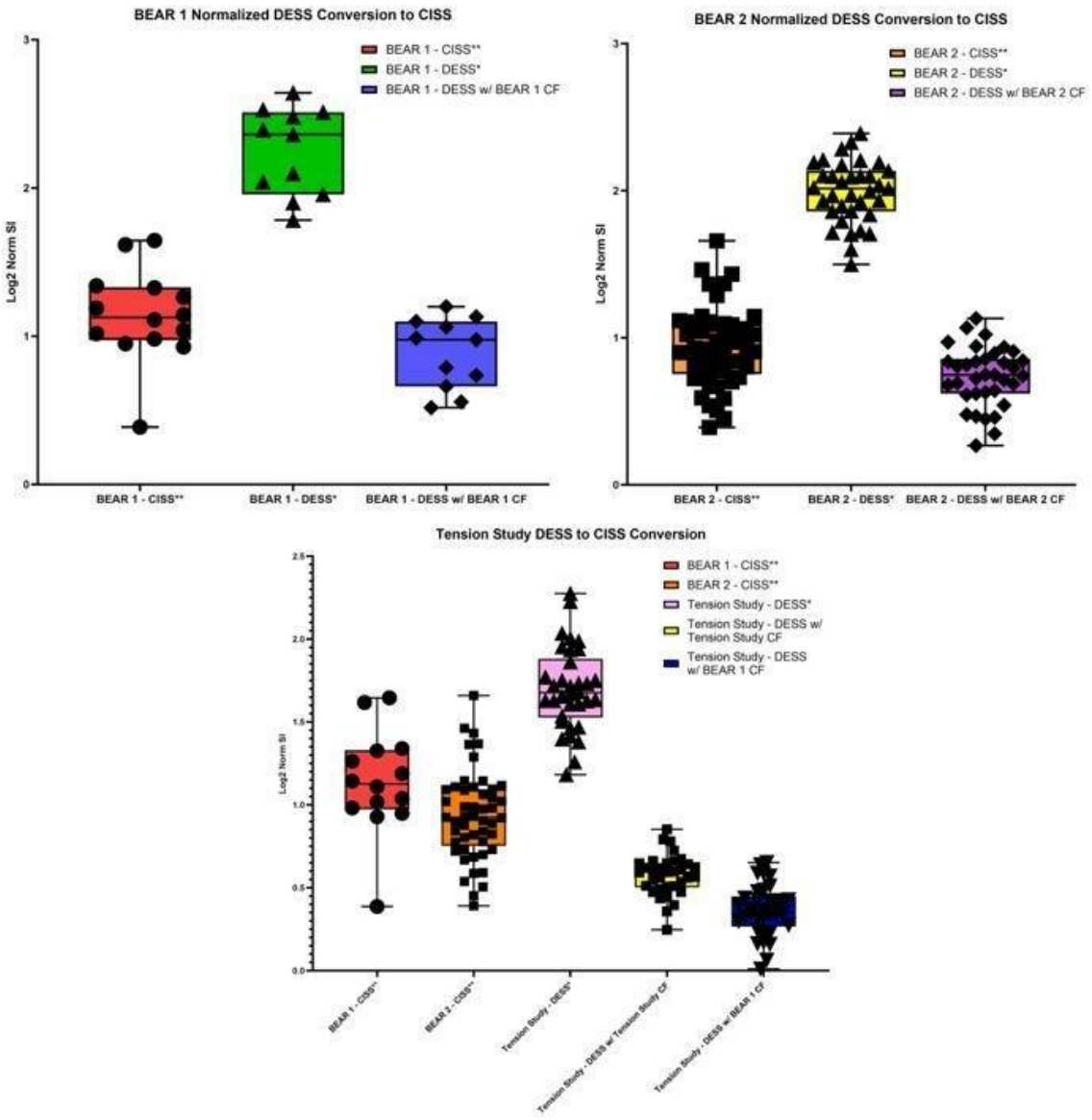

Figure B. 1 BEAR I CISS SI (red), DESS SI (green) and DESS adjusted SI (blue); BEAR II CISS SI (orange), DESS SI (yellow), and DESS adjusted SI (purple); Tension study DESS SI (pink) and DESS adjusted SI (blue)

Histogram Matching: Histogram matching by aligning the specific reference of the targeted proved to perform well with this cohort of patients. Match intensity distribution of the segmented ACL region in the DESS and CISS showed promise and allows for a global adjustment of the entire intensity range (Figure B. 3). MAE for the BEAR I patients was 0.010 (n=11) and for BEAR II was 0.131 (n=22) (Figure B. 2).

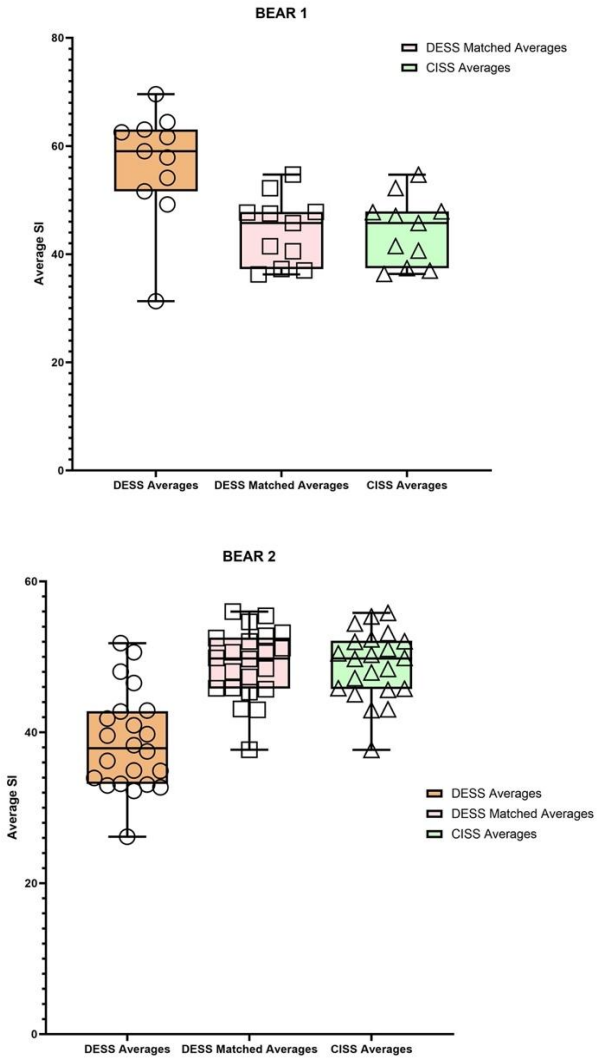

Figure B. 2. BEAR I MAE (left) and BEAR II MAE (right) distributions between the DESS average, DESS matched/adjusted average, and the CISS average

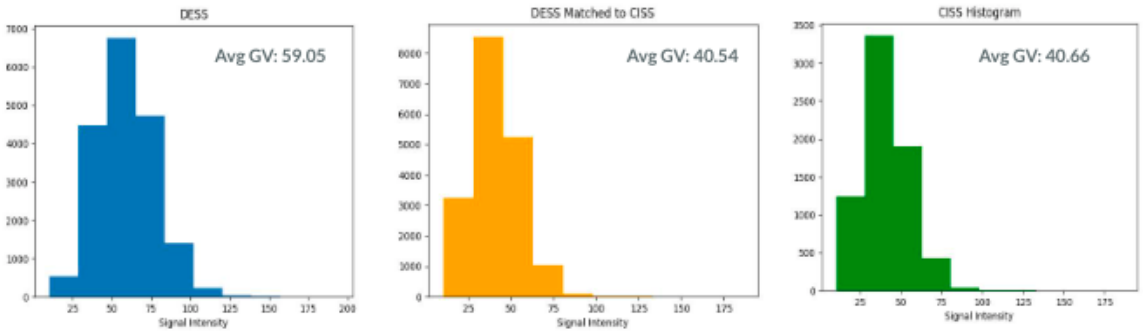

Figure B. 3. Example of DESS Histogram Matching. Original DESS pixel value distribution (blue), adjusted DESS (yellow), and CISS histogram pixel distribution (green)

Non-Grid CycleGAN: The run-time for one epoch was found to be 3 hours with the addition of upscaling to the convolutional layers. Due to this reason, only 15 epochs were able to run and were qualitatively evaluated. What we were able to visualize was that the model, even with the addition of the upsampling layers to the convolutions, was not able to produce optimal results. The grid-like artifacts in the output images were not as obvious as the original CycleGAN results in Chapter 6 for the DESS to CISS transformations (Figure 28). The payoff was largely seen in the sharpness and overall quality of the outputs (Figure B. 4).

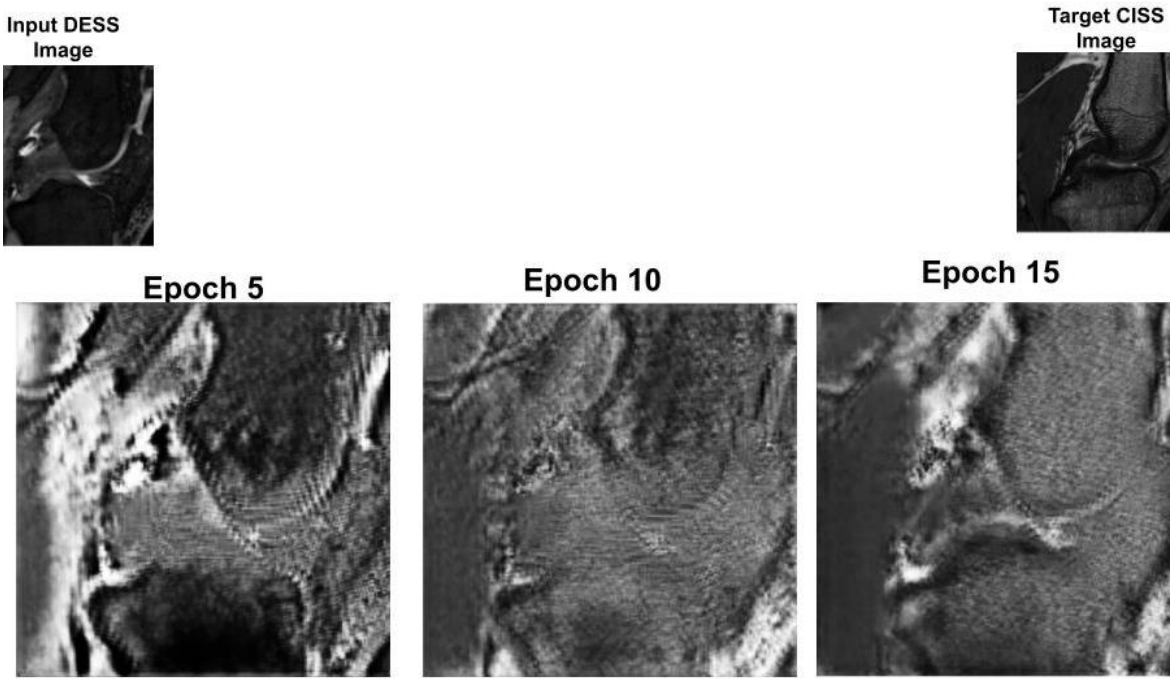

Figure B. 4 Output images after 5, 10, and 15 epochs of the updated CycleGAN model with original input images (top left) and target image (top right)

Discussion: There is still much needed to be done in the field of MRI sequence-to-sequence transformations. However, each of these studies has allowed for further insight into the advantages and disadvantages of varying methods. The Ratio of Mean Intensities is a simplistic way to mathematically transform pixel values from a source to a target

range. However, it's simplicity may often overlook the complexities of MRI acquisition parameters that result in very high MAE scores with agreement between the target and adjusted source in the BEAR I were found to not be significantly different. BEAR I does have a lower sample size, which may have allowed for this agreeance between the adjusted DESS and target CISS values. Scaling intensities with a simple linear transformation was found to be insufficient. Therefore, a higher order of transformation was needed. Histogram matching was thought to be a more sophisticated method that may have led to better results.

Histogram matching was shown to result in much better MAE scores between the adjusted DESS and target CISS pixel values. These values improved from the RMI method, which proved to be advantageous. However, Histogram matching requires the need of perfect one-to-one matching. This would require each subject to obtain an image in both DESS and CISS images in order to conduct the successful transformation of histograms. This is not always possible, and the need for perfect pair defeats the purpose of creating a normalization technique that would perform this transformation if the patient only had the DESS scans.

The last and final effort of this study was to update the CycleGAN to advance the convolutional layers with an upscaling layer to hopefully remove the grid-like artifacts found in the output images presented in Chapter 6. Although the grid-like artifacts were adjusted for with the updated method of CycleGAN, there were additional obstacles created with the adjustment of the CycleGAN architecture. The first and most prominent obstacle was the run-time for each epoch. The epoch run-time was now 3 hours for one epoch, which was due to the lack of convergence found from the comparison between the

generated images and the target images. This increased run-time from 1 hour with the original model to 3 hours significantly impacted the number of epochs we were able to run with the given GPUs of the Google Cloud system. The model also did not perform well, as there was a different variation of noise that was introduced, specifically around the region of interest, which was the ACL. Overall, given these obstacles of the updated model along with the previous methods, we concluded that the model presented in Chapter 6 performed the best for this task and acknowledged there are opportunities for growth in the field of machine learning to perform MRI sequence-to-sequence transformations.